Lubricant Flow and De-wetting at the Head-Disk Interface of a Hard Disk Drive

by

Alejandro Rodriguez Mendez

A dissertation submitted in partial satisfaction of the

requirements for the degree of

Doctor of Philosophy

in

Engineering – Mechanical Engineering

in the

Graduate Division

of the

University of California, Berkeley

Committee in charge:

Professor David B. Bogy, Chair
Professor Stephen Morris
Professor Lawrence C. Evans

Fall 2015

Lubricant Flow and De-wetting at the Head-Disk Interface of a Hard Disk Drive

Abstract

Lubricant Flow and De-wetting at the Head-Disk Interface of a Hard Disk Drive

by

Alejandro Rodriguez Mendez

Doctor of Philosophy in Engineering - Mechanical Engineering
University of California, Berkeley

Professor David B. Bogy, Chair

In this dissertation we investigate the lubricant behavior at the head-disk interface of a hard disk drive (HDD) by numerically simulating the formation of lubricant moguls on the disk and the accumulation of lubricant on the slider's air bearing surface (ABS). We use classical lubrication theory from continuum mechanics to model both the air bearing and the lubricant motion. The numerical simulations were compared to experimental tests of lubricant reflow on the disk after laser heating. A good agreement was found between experiments and numerical simulations.

We investigate the effects of the slider's flying height, skew angle and ABS design on the lubricant flow and reflow. We describe the lubricant thickness profile and volume evolution on the slider's ABS and lateral walls. It was found that a smaller flying height contributes to a faster lubricant removal from the ABS due to the induced increase in the air shear stress. When the HDD is at rest, the lubricant accumulated on the deposit end flows back into the ABS driven by the action of disjoining pressure. It is found, for a particular slider design, that increasing the slider's radial position and thus changing its skew angle has the effect of enhancing the lubricant flow process due to a decrease in the slider's flying height. The lubricant migration process is significantly dependent on the ABS design. It is found that slider designs that accumulate most lubricant on a broader area on the deposit end and have larger values of air shear stress remove lubricant from the ABS at higher volume rates than those designs where accumulation is concentrated near the center of the deposit end and have smaller values of average shear stress.

We simulate the flow and reflow processes of unstable lubricant films. We study the spreading of droplets with thickness larger than the critical de-wetting thickness. It is observed that, if surface tension is neglected from the governing equations, the disjoining pressure acts as a destabilizing force inducing an unrestrained growth of the film. The disjoining pressure breaks up the initial droplet into smaller ones which narrow down in width and increase in height. As the growth continues, the curvature of each droplet becomes sufficiently large to balance the disjoining pressure. The final state consists of a few isolated droplets connected by a uniform film. When we include the effect of air shear stress and air pressure gradient the initial droplet breaks up into smaller ones, which are then sheared downstream in the direction of the air shear stress. It was not possible to simulate the de-wetting behavior of the lubricant film on the entire slider domain, since it was found that surface tension is significant only at length scales several orders of magnitude smaller than the size of the slider.

Finally we investigate the changes in magnetic spacing due to lubricant migration on the ABS and study the formation of lubricant clots on the disk surface known as “moguls”. It is observed that the minimum magnetic spacing of a lubricant contaminated slider is significantly larger than that of a clean slider even after a relatively long time of flying the slider over the disk. This increase in spacing is detrimental for the read/write performance of the HDD. It is also observed that the air shear stress can generate lubricant moguls on the disk surface due to oscillations of the slider along the vertical, downtrack and offtrack directions.

To my parents Refugio Eugenia and Manuel

Contents **Page**

Acknowledgements

First and foremost I would like to thank my adviser Professor David B. Bogy for his unrestricted moral, academic and financial support. He is probably the best adviser a student can have. Even though Professor Bogy is in charge of a profitable laboratory, his main concern is the education of his students. I am grateful to him for letting me develop my own research interests and providing me with guidance during my studies at UC Berkeley.

My appreciation goes to Professors Stephen Morris, David Steigmann and Lawrence C. Evans for their valuable contributions to my dissertation and my qualifying exam. I learned most of the theoratical background necessary for the development of this dissertation from the lectures and office hours of Professor Morris. I am also fortunate to have attended the inspiring lectures offered by Professor Steigmann whose knowledge in elasticity is close to absolute.

I thank my collegues in the Compute Mechanics Laboratory for sharing their knowledge and ideas with me. My research work was enriched from my discussions with Sripathi V. Canchi, Rahul Rai, Jinglin Zheng, Liping Li, Joanna Bechtel Dahl, Shaomin Xiong, Yung-Kan Chen, Soroush Ghahri Sarabi, Haoyu Wu, Yuan Ma, Tholfagar Mardan and Amin Ghafari Zeydabadi. I was fortunate to have shared my 5 years of PhD with my friend Yung-kan Chen. Together we worked on course materials, homeworks and research. We both attended several international conferences including one in Turin, Italy and another in Dresden, Germany. Shaomin, Soroush, Haoyu, Yuan, Tholfagar and Amin have shaped definitely the contents of this dissertation for which I am grateful.

I also thank my parents: Manuel Rodriguez Sanchez and Refugio Eugenia Mendez Torres; my brothers: Luis Manuel and Rafael; and my sister Susana for their support and encouragement at all times.

This work was supported by the Computer Mechanics Laboratory (CML) at the University of California, Berkeley, the Consejo Nacional de Ciencia y Tecnología (CONACYT) and the University of California Institute for Mexico and the United States (UC-MEXUS).

Chapter 1

Introduction

1.1 Hard Disk Drive operation and the Head-Disk Interface (HDI)

A hard disk drive (HDD) is a data storage device used for storing and retrieving digital information using rapidly rotating disks (platters) coated with magnetic material. A HDD retains its data even when it is powered off. A typical HDD design consists of a spindle that holds flat rigid ("hard") disks with magnetic heads arranged on a moving actuator arm to read and write data to the surfaces [1]. A typical HDD design is shown in figure 1.1. The platters are made from a non-magnetic material, usually aluminum alloy, glass, or ceramic, and are coated with a shallow layer of magnetic material typically 10–30 nm in depth [2]. The magnetic recording layer is protected from impact, corrosion, and wear by a hard diamond-like carbon overcoat (2-3 nm thick) and a thin polymer lubricant layer (1-2 nm thick) [3]. The platters in contemporary HDDs are spun at speeds varying from 5,400 rpm in energy-efficient portable devices, to 15,000 rpm for high-performance servers. The faster the platter spins, the faster data can be written or read in a HDD [4].

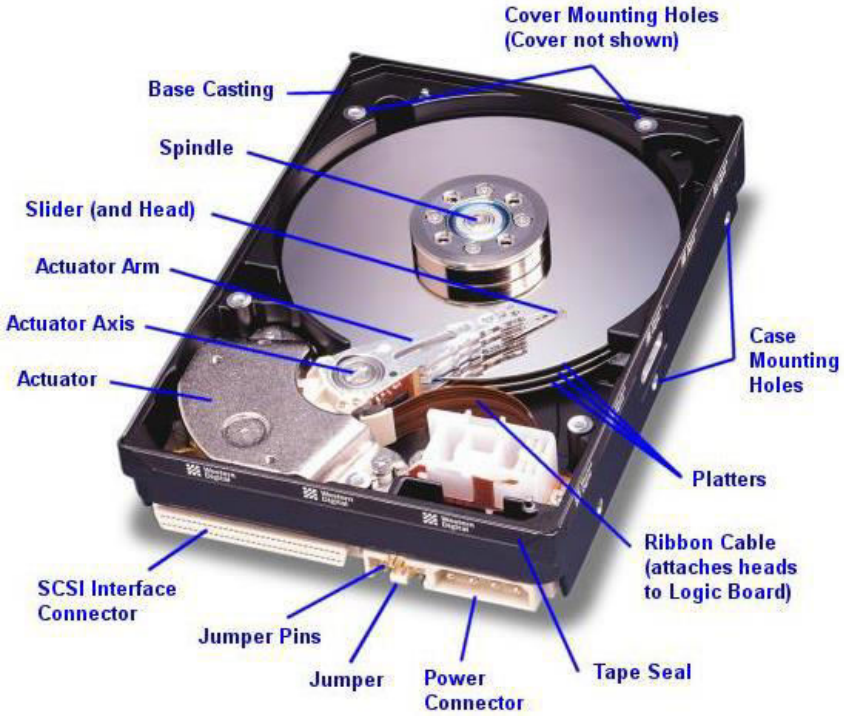

Fig. 1.1. Photograph of a Western Digital hard disk drive [2].

A read/write head (slider) floats above the spinning platter reading and writing data. A HDD records data by magnetizing a thin film of magnetic material on a disk. Sequential changes in the direction of magnetization represent binary data bits. The data is read from the disk by detecting the transitions in magnetization. User data is encoded using an encoding scheme that determines how the data is represented by the magnetic transitions [5]. The read/write heads (sliders) are the small parts of a disk drive, that move above the disk surface and transform the disk's magnetic field into electrical current (reading) or vice versa (writing). The read and write transducers are

protected from contact and corrosion by a carbon overcoat (2-3 nm thick). The heads have gone through a number of changes over the years. A sketch of the head-disk interface is shown in figure 1.2. The heads "fly" above the disk surface with clearance of around 1 nanometer [6]. The flying height has been constantly decreasing to enable higher areal density. The flying height of the head is controlled by the design of an air-bearing surface (ABS) etched onto the disk-facing surface of the slider. The role of the air bearing surface is to maintain a constant flying height as the head moves over the surface of the disk. If the head hits the disk's surface, a catastrophic head crash can result. A recent technology called thermal flying height control (TFC) improves the flying reliability at low physical clearances by bringing only the trailing edge portion of the slider containing the read and write transducers close to the disk. In TFC power is supplied to a resistive heater embedded in the slider, and the thermal expansion bulge containing the read/write transducer brings these elements to the required physical proximity to the disk. The TFC concept involves a heater element imbedded near the read/write transducer. Electric power is applied to the heater during reading and writing processes, causing a local thermal protrusion underneath the transducer, thus reducing the spacing between the transducer and the disk.

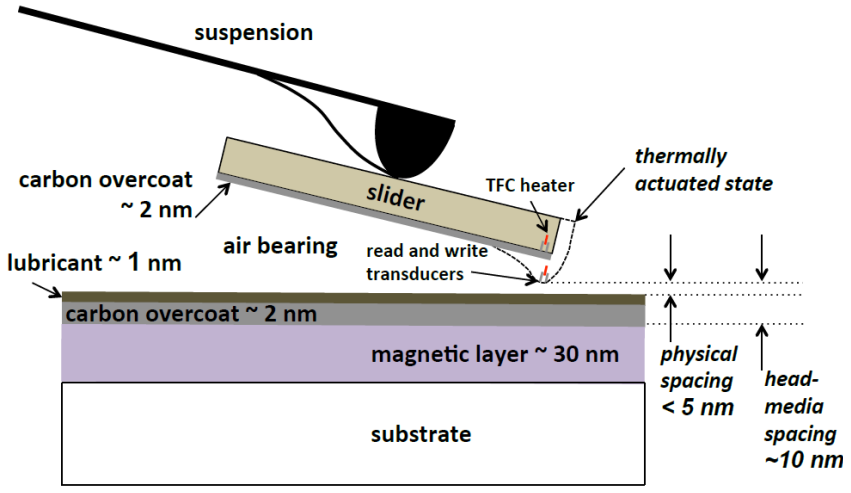

Fig. 1.2. Head-Disk Interface [7].

A typical HDD has two electric motors; a spindle motor that spins the disks and an actuator motor that positions the read/write head assembly across the spinning disks. Opposite the actuator at the end of the head support arm is the read-write head. Circuit cables connect the read-write heads to amplifier electronics mounted on the actuator. The relative velocity between the disk and slider, on the order of 10 m/s, forms a self-acting pressurized gas bearing called the air bearing that balances the applied suspension load and moments that act to push the slider toward the disk. In equilibrium, the slider is "flying" above the disk with a minimum physical clearance (also called flying height) of about 5 nm or less in modern HDDs. The read/write head assembly relies on air inside the disk enclosure to support the heads at their proper flying height while the disk rotates. HDDs require a certain range of air densities in order to operate properly. The connection to the external environment and density occurs through a small hole in the enclosure (about 0.5 mm in breadth), usually with a filter on the inside (the breather filter) [8]. If the air density is too low, as at high elevations, then there is not enough lift for the flying head, so the head gets too close to the disk, and there is a risk of head crashes and data loss. Specially manufactured sealed and pressurized disks are needed for reliable high-altitude operation, above

about 3,000 m (9,800 ft) [9]. The air inside the operating drive is constantly moving too, being swept in motion by friction with the spinning platters. This air passes through an internal recirculation filter to remove any leftover contaminants from manufacture, any particles or chemicals that may have somehow entered the enclosure, and any particles or outgassing generated internally in normal operation. High humidity present for extended periods of time can also damage the heads and platters.

1.2 Hard Disk Drive Industry

Hard Disk Drives were first introduced by IBM in 1956. HDDs became the dominant secondary storage device for general-purpose computers by the early 1960s. Continuously improved, HDDs have maintained this position into the modern era of servers and personal computers. More than 200 companies have manufactured HDDs over time. But consolidations have concentrated production into just four manufacturers today: Western Digital, Seagate, HGST and Toshiba. Worldwide disk storage revenues were US $32 billion in 2013, down 3% from 2012. The major advantage of a HDD is that it is capable of storing a large amount of data cheaply. These days, 1 Terabyte (1,024 gigabytes) of storage is not unusual for a laptop hard drive, and the density continues to grow. However, the cost per gigabyte is hard to calculate now-a-days since there are so many classes to consider, though it is safe to say that all HDDs are substantially cheaper than SSDs. As a comparison, the popular WD Black (1TB) goes for roughly $69 on most websites while the Crucial M500 (960GB) and Samsung 840 EVO (1TB) SSDs go for $369 and $439 respectively, over five times the price of the WD Black. So if you want cheap storage and lots of it, using a standard hard drive is definitely the more appealing way to go. The most common size for laptop hard drives is the 2.5” form factor while a larger 3.5” form factor is used in desktop computers. The larger size allows for more platters inside and thus more storage capacity.

The digital and computer technology advances in the last several decades have been made possible in part by the ability to store and access digital data. Much of the world's digital information has been and still is stored on hard disk drives (HDDs). While hard drives may appear to the consumer to be giving way to solid state drives (SSDs) in many popular mobile devices, the convenience of accessing your data "anytime, anywhere" on multiple devices is possible because of the storage of multiple copies of your digital data on servers, refrigerator sized arrays of hard disk drives connected on a network, maintained by a cloud service provider [10]. Digital technology has also been leveraged in practically every sector of modern society; all these activities require storage and access of digital data, tasks often provided by hard disk drives. As the worldwide demand for data storage continues to explode HDDs remain an important infrastructure player in the world's technological development.

The tremendous increase in magnetic areal density and the associated decrease of cost per gigabyte has been largely responsible for the proliferation of hard disk drive recording into new applications and markets. The superparamagnetic limit imposes a signal-to-noise ratio, thermal stability, and writability tradeoff that limits the ability to continue to scale traditional magnetic recording technology to higher storage densities. A new technology called Heat-assisted magnetic recording (HAMR) promises to extend the areal density of magnetic data storage. By temporarily heating the media during the recording process, the media coercivity can be lowered below the available applied magnetic write field, allowing higher media anisotropy and therefore smaller thermally stable grains. The heated region is then rapidly cooled in the presence of the

applied head field whose orientation encodes the recorded data. A sketch illustrating the HAMR writing process is shown in Fig. 1.3. With a tightly focused laser beam heating the media, the write process is similar to magneto-optical recording, but in a HAMR system the readout is performed with a magnetoresistive element [11].

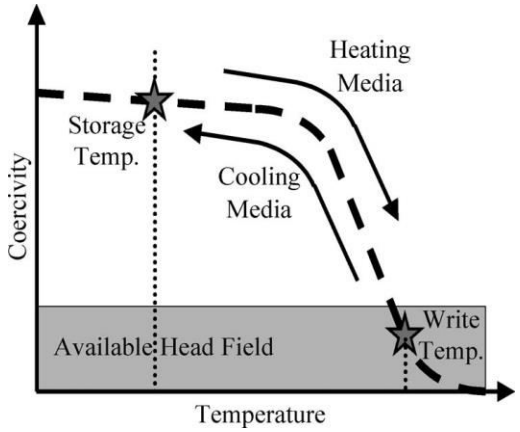

Fig 1.3. A schematic diagram of the HAMR write process [11].

HAMR requires the development of a number of novel components. These include the light delivery system, the thermomagnetic writer, a robust head disk interface, and rapid cooling media. Designing these components into a high-performance data storage system requires a large research investment. In addition to developing the HAMR technology, the head-media spacing must also be reduced from 10 nm in current HDD products to 4.5 nm for 4 TB/in2 magnetic recording. New revolutionary technologies in materials, processes, and clearance control schemes will be needed to realize the estimated 0.9 nm head overcoat, 1 nm flying height, 0.8 nm lubricant, and 1.5 nm disk overcoat requirements. Not only will the capabilities of HDI technology be stretched to reduce head-media spacing, but new challenges and requirements to HDI stability will be introduced by HAMR never seen before in traditional drives [12].

1.3 Objective and Organization of this Dissertation

The objective of this dissertation is to advance the understanding of the lubricant behavior at the head-disk interface by numerically simulating the accumulation of lubricant on the slider's air bearing surface and the formation of lubricant moguls on the disk surface. Lubrication theory is used to model both the air bearing and lubricant motion.

This dissertation is composed of eight chapters. Chapter 1 presents a brief introduction to the hard disk drive principles and construction. Chapter 2 describes the forces acting on thin fluid films giving rise to the concept of disjoining pressure. The governing partial differential equations for the air bearing and lubricant films are derived from Reynolds lubrication theory. Chapter 3 describes an experimental investigation of the lubricant reflow process after laser heating and compares the results with those obtained from numerical simulations. Chapter 4 presents numerical simulations of lubricant flow on the slider's air bearing surface focusing attention on the effects of flying height, skew angle and ABS design. The lubricant accumulation characteristics on the slider's ABS and lateral walls are described. In chapter 5 we investigate the de-wetting behavior of lubricant films used in HDDs. We simulate the flow and reflow processes of unstable lubricant films. In chapter 6 we investigate the changes in flying height due to

lubricant migration on the ABS and in chapter 7 we investigate the formation of lubricant moguls on the disk surface. Finally, a concluding summary and suggestions for future work are provided in Chapter 8.

Chapter 2

Lubrication Theory

2.1 Surface tension and the Young-Laplace equation

The cohesive forces between liquid molecules are responsible for the phenomenon known as surface tension. The molecules at the surface do not have other like molecules on all sides of them and consequently they cohere more strongly to those directly associated with them on the surface. A molecule in the bulk liquid experiences cohesive forces with other molecules in all directions, resulting in a net force of zero. A molecule at the surface of a liquid experiences only net inward cohesive forces. The net effect is an inward force at its surface that causes liquid to behave as if its surface were covered with a stretched elastic membrane. Surface tension is measured as the energy required to increase the surface area of a liquid by a unit of area. Surface tension has the dimension of force per unit length or of energy per unit area. Surface tension is responsible for the shape of liquid droplets. Although easily deformed, droplets of water tend to be pulled into a spherical shape by the imbalance in cohesive forces of the surface layer. In the absence of other forces, including gravity, drops of virtually all liquids would be approximately spherical [13].

Surface tension acts only at the free surface; consequently, it does not appear in the Navier-Stokes equations, but rather enters through the boundary conditions [14]. The surface tension, σ, at the air-liquid interface, S, acts tangentially to the liquid surface with unit tangent, $\boldsymbol{\nu}$, as shown in figure 2.1.

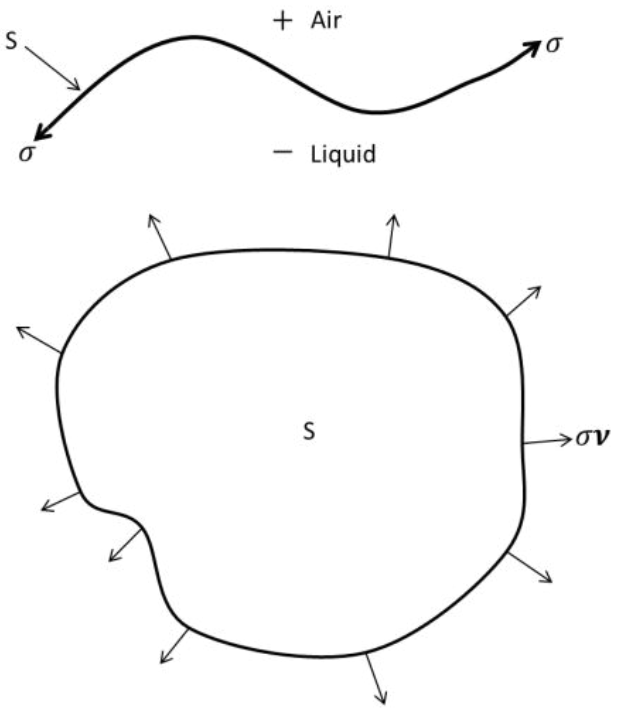

Fig.2.1. Surface tension acting on the air-liquid interface of a liquid body.

Consider the material volume, R, around the air-liquid interface shown in figure 2.2. The liquid surface enclosed by R is denoted by ω. A balance of forces on R yields,

$$\int_R \rho \ddot{\boldsymbol{x}} dv = \int_{\partial R} \boldsymbol{T}\boldsymbol{n} da + \int_R \rho \boldsymbol{b} dv + \int_{\partial \omega} \sigma \boldsymbol{\nu} ds, \tag{2.1}$$

where dv, da, ds denote volume, area and line differentials respectively.

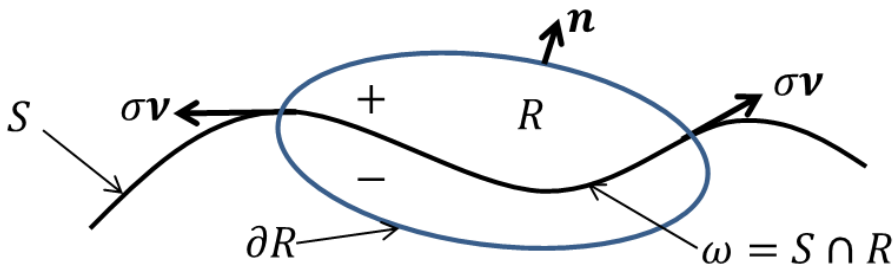

Fig. 2.2. Material volume around the air-liquid interface.

In the limit as the volume R collapses onto the surface S the volume integrals vanish and equation (2.1) yields

$$\boldsymbol{0} = \int_{\omega} [\![\boldsymbol{T}]\!]\boldsymbol{n} da + \int_{\partial \omega} \sigma \boldsymbol{\nu} ds, \tag{2.2}$$

where $[\![\boldsymbol{T}]\!] = \boldsymbol{T}^{+} - \boldsymbol{T}^{-}$ and $\boldsymbol{n}$ denotes the surface normal on ω pointing outwards, i.e. from the liquid into the air. We use Stokes' theorem in the above equation to convert the line integral on $\partial\omega$ into a surface integral on ω, and obtain,

$$\boldsymbol{0} = \int_{\omega} [\![\boldsymbol{T}]\!]\boldsymbol{n} da + \int_{\omega} [(\boldsymbol{I} - \boldsymbol{n}\otimes\boldsymbol{n})\nabla\sigma - \sigma(\nabla \cdot \boldsymbol{n})\boldsymbol{n}] da. \tag{2.3}$$

Since the surface ω is arbitrary, we can localize the above equation to obtain,

$$[\![\boldsymbol{T}]\!]\boldsymbol{n} + [(\boldsymbol{I} - \boldsymbol{n}\otimes\boldsymbol{n})\nabla\sigma - \sigma(\nabla \cdot \boldsymbol{n})\boldsymbol{n}] = \boldsymbol{0}, \qquad on\ \boldsymbol{S}. \tag{2.4}$$

The above equation can be decomposed into tangential,

$$(\boldsymbol{I} - \boldsymbol{n}\otimes\boldsymbol{n})[\![\boldsymbol{T}]\!]\boldsymbol{n} + (\boldsymbol{I} - \boldsymbol{n}\otimes\boldsymbol{n})\nabla\sigma = \boldsymbol{0}, \tag{2.5}$$

and normal terms,

$$(\boldsymbol{n}\otimes\boldsymbol{n})[\![\boldsymbol{T}]\!]\boldsymbol{n} - \sigma(\nabla \cdot \boldsymbol{n})\boldsymbol{n} = \boldsymbol{0}. \tag{2.6}$$

In the framework of lubrication theory, the normal stress at the interface, $T_{nn} \approx T_{zz}$, is approximated by the fluid pressure, i.e. $T_{zz} = -p$. Hence, equation (2.6) can be written in the form,

$$0 = [\![T_{zz}]\!] - \sigma(\nabla \cdot \boldsymbol{n}) = -p^{+} + p^{-} - \sigma(\nabla \cdot \boldsymbol{n}). \tag{2.7}$$

Equation (2.7) is known as the Young-Laplace equation. This equation can be interpreted as the balance of normal forces on a given surface element of the liquid, as shown in figure 2.3.

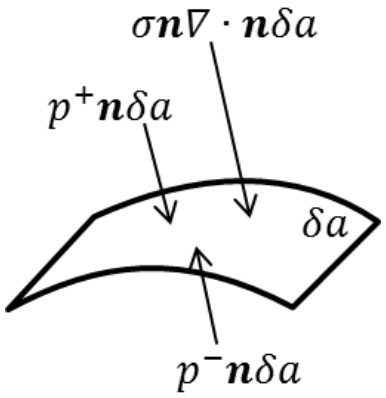

Fig. 2.3. Balance of normal forces on an area element at the air-liquid interface.

For a liquid film on the $x - y$ plane with a free surface determined by the equation $z = h(x, y)$, the unit normal, $\boldsymbol{n}$, is given by

$$\boldsymbol{n} = -\left(1 + {h_x}^2 + {h_y}^2\right)^{-1/2}\left(h_x \boldsymbol{e_1} + h_y \boldsymbol{e_2} - \boldsymbol{e_3}\right). \tag{2.8}$$

Hence,

$$\nabla \cdot \boldsymbol{n} = -\left(1 + {h_x}^2 + {h_y}^2\right)^{-3/2}\left[\left(1 + {h_y}^2\right)h_{xx} - 2h_x h_y h_{xy} + \left(1 + {h_x}^2\right)h_{yy}\right]. \tag{2.9}$$

In the framework of lubrication theory it is assumed that the surface slopes h_x, h_y are small compared to unity. Hence, we can neglect the squares of these terms in equation (2.9) to obtain,

$$\nabla \cdot \boldsymbol{n} = -h_{xx} - h_{yy}. \tag{2.10}$$

So, the Young-Laplace equation becomes,

$$p^{-} = p^{+} - \sigma\left(h_{xx} + h_{yy}\right). \tag{2.11}$$

2.2 Disjoining pressure and the augmented Young-Laplace equation

It is observed experimentally that in nanometer-thin lubricant films, the molecules in the solid substrate interact with those of the coating fluid giving rise to an additional pressure within the liquid film (additional to that induced by surface tension and ambient pressure). This pressure is known as "disjoining pressure". Disjoining pressure is generated by several molecular

interactions, e.g. van de Waals forces, electrostatic forces between charged surfaces, structural effects of the liquid, etc. Disjoining pressure characterizes the state of a thin layer. The pressure depends on the thickness of the film, the composition and properties of the interacting phases (bodies), and the temperature. In the lubrication approximation, when the slope of the free surface of the film is small compared to unity, we can assume that the outcome of all interactions between the film and the exterior environment is a pressure, $\Pi(h)$, which depends only on the local film thickness h. The disjoining pressure $\Pi(h)$ can be either positive (solid repels the air-liquid interface) or negative (solid attracts the air-liquid interface), depending on the properties of the solid substrate and coating films [15].

We can interpret the disjoining pressure to be an external pressure in addition to that of the air pressure, p^+, acting on the air-liquid interface as shown in figure 2.4.

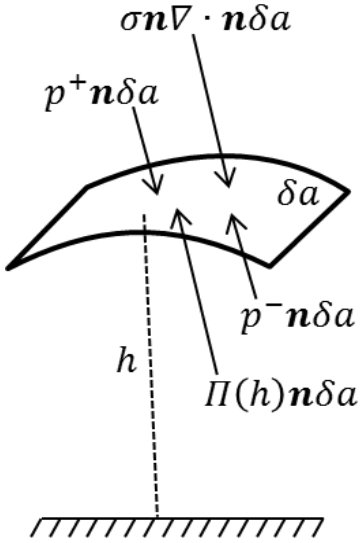

Fig. 2.4 Balance of normal forces on an area element at the air-liquid interface.

A balance of balance of normal forces on a surface element of the liquid yields,

$$p^- = p^+ + \sigma(\nabla \cdot \boldsymbol{n}) - \Pi(h). \tag{2.12}$$

Equation (2.12) is known as the augmented Young-Laplace equation. When the interaction between the liquid film and the solid substrate is dominated by van der Waals forces, the disjoining pressure can be approximated by the expression

$$\Pi(h) = \frac{A}{h^3}, \tag{2.13}$$

where A is known as the Hamaker constant [16]. Other expressions for disjoining pressure commonly employed in the literature are shown in table 2.1 and plotted in figure 2.5.

Table 2.1. Some expressions for disjoining pressure encountered in the literature

Disjoining pressure	$\Pi(h)$
Model 1 [16]	$\frac{a_1}{h^3}$
Model 2 [17]	$\frac{a_2}{h^n}+\frac{a_3}{h^m}, \quad 0<n<m$
Model 3 [18]	$\frac{a_4}{h^3}+a_5 e^{-a_6 h}+a_7\cos(a_8 h+a_9)\,e^{-a_{10}h}$

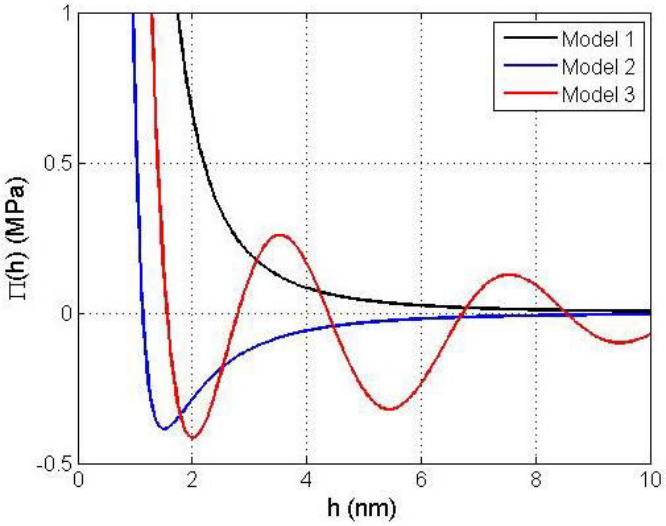

Fig. 2.5. Disjoining pressure as a function of liquid film thickness for the three models given in table 2.1 with: $m=3, n=4, a_1=5.3(10^{-21}), a_2=-a_1, a_3=6(10^{-30}), a_4=a_1, a_5=1.6(10^6), a_6=5(10^8), a_7=-10^6, a_8=1.57(10^9), a_9=3.77, a_{10}=2.5(10^8)$.

2.3 Lubrication Theory

As observed in chapter 1, in current hard disk drives the minimum physical spacing between the disk and slider is less than 5 nm and the lubricant thickness is around 1 nm. These characteristic lengths scales are much smaller than the lateral dimensions of the slider (typically 0.7-1 mm) and the disk radius (typically 10-30 mm). When modeling these components of the head-disk interface, one can take advantage of the disparity in length scales between coordinate directions to simplify the analysis. For both, the air bearing and the lubricant coating the disk, the governing equations are specialized forms of the well-known Reynolds lubrication equation. The lubricant is considered to be an incompressible Newtonian fluid, while the air is considered an ideal gas as well as a compressible Newtonian fluid. The governing equations are derived via the traditional lubrication approximation procedure first described by Reynolds [19].

In fluid dynamics, lubrication theory describes the flow of fluids (liquids or gases) in a geometry in which one dimension is significantly smaller than the others. Mathematically, lubrication theory can be seen as exploiting the disparity between two length scales. The first is the characteristic film thickness, h, and the second is a characteristic substrate length scale L. The key requirement for lubrication theory is that the ratio h/L is small [20].

Problems of flow in thin films appear not only in HDDs but they also play an important role in a number of applications, such as the spreading of a film, or the lubrication of a hydraulic journal bearing. These all involve flow in long thin fluid layers, so the velocity component tangent to the

layer is large compared with that perpendicular to the layer: the flow is "quasi-parallel". The dynamics of the spreading of a liquid film, in the first instance, and the forces between solid surfaces moving relative to each other, in the second, can be calculated by making the simplifying assumption that the flows occur principally in the direction of the plane of the film. Specifically, it is the effect of varying pressure along the film that accounts for the force between the two components of the bearing [21].

Consider first a horizontal plate sliding on an incompressible lubricating film past a secondary surface as seen in figure 2.6. If the distance h separating the two plates is small compared to the dimension of the plate, L, we can assume fully developed flow applies throughout most of the film when the flow has reached steady state.

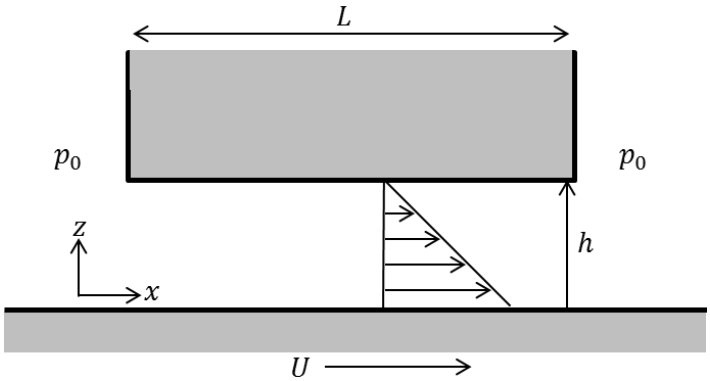

Fig. 2.6. Horizontal plate on an incompressible film coating a moving plate.

If we assume a velocity field of the form $\boldsymbol{v} = v(z)\boldsymbol{e}_x$ we find that the Navier-Stokes equations reduce to,

$$\nabla p = \mu v_{,zz}\boldsymbol{e}_x. \tag{2.14}$$

This equation and the boundary conditions for p imply $p = p_0$ for all x, z, and a velocity profile of the form

$$v(z) = U\left(1 - \frac{z}{h}\right). \tag{2.15}$$

Since the pressure is the same inside the film as outside the slider, the sliding motion of two parallel surfaces produces no lateral z-component of force. To obtain the volume flux through the gap we integrate the velocity with respect to z to obtain,

$$q = \int_0^h v(z)dz = \frac{1}{2}Uh. \tag{2.16}$$

Now suppose the slider is inclined ever so slightly relative to the stationary plate as in figure 2.7. We might guess that if the slope ε is small enough, the velocity profile will not be affected.

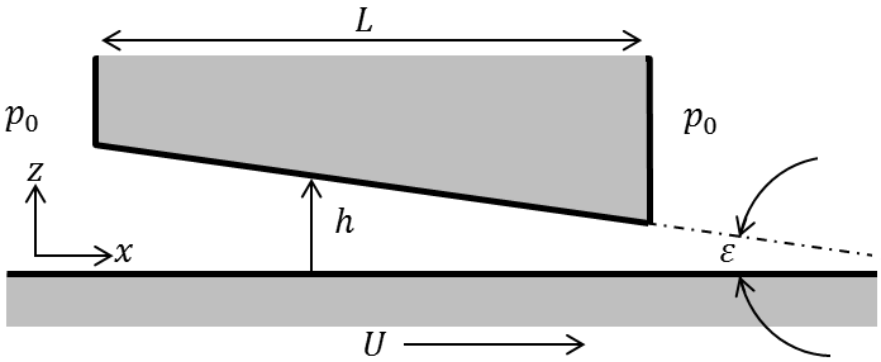

Fig. 2.7. Inclined plate on an incomplressible film coating a moving horizontal plate.

But, owing to the inclination, h is no longer independent of x, so our guess $\boldsymbol{v} = v(z)\boldsymbol{e}_x$ leads to $q = 0.5Uh(x) = f(x)$, which violates continuity (mass conservation). However, continuity is preserved by a nonzero pressure gradient, dp/dx, which causes pressure driven flow. Thus, even the primary component of the velocity profile is affected by this slight inclination. More significantly, this inclination produces a pressure in the film different from the fluid outside the slider which tends to push the two surfaces apart or together.

2.4 Lubrication approximation of the Navier-Stokes equation of fluid mechanics

It is convenient to write down here the equations governing a compressible Newtonian fluid. The constitutive equation for stress is given by,

$$\boldsymbol{T} = -p(\rho)\boldsymbol{I} + \lambda(tr\boldsymbol{D})\boldsymbol{I} + 2\mu\boldsymbol{D}, \tag{2.17}$$

where $\boldsymbol{D} = 1/2(\mathbf{L} + \mathbf{L}^T)$ and $\mathbf{L} = \nabla\boldsymbol{v}$. We use the above expression for stress in the Cauchy momentum equation,

$$\nabla \cdot \boldsymbol{T} + \rho\boldsymbol{b} = \rho(\boldsymbol{v}_t + \mathbf{L}\boldsymbol{v}), \tag{2.18}$$

to obtain the Navier-Stokes equation,

$$-\nabla p + (\mu + \lambda)\nabla(\nabla \cdot \boldsymbol{v}) + \mu\,\Delta\boldsymbol{v} + \rho\boldsymbol{b} = \rho(\boldsymbol{v}_t + \mathbf{L}\boldsymbol{v}). \tag{2.19}$$

Conservation of mass yields the continuity equation,

$$0 = \dot{\rho} + \rho\nabla \cdot \boldsymbol{v} = \rho_{,t} + \nabla \cdot (\rho\boldsymbol{v}), \tag{2.20}$$

which along with (2.19) and properly defined boundary conditions define the motion of the fluid [22].

We want to non-dimensionalize the above governing equations to obtain approximate scales for all variables. Consider the case of a fluid with negligible body forces. In this case equation (2.19) becomes,

$$-\nabla p + (\mu + \lambda)\nabla(\nabla \cdot \boldsymbol{v}) + \mu\,\Delta\boldsymbol{v} = \rho(\boldsymbol{v}_{,t} + \mathbf{L}\boldsymbol{v}). \tag{2.21}$$

We want to study an air bearing slider of dimension L with minimum spacing h_0 flying over a disk moving with velocity U. The disk surface lies in the (x, y) plane as shown in figure 2.8.

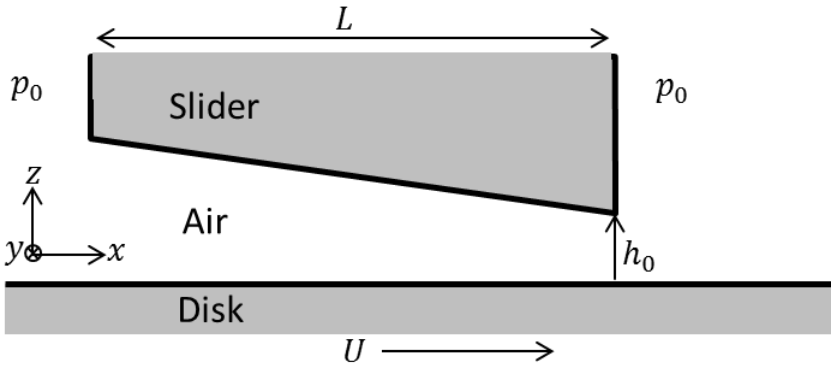

Fig. 2.8. Slider air bearing flying over a moving disk.

In the momentum and continuity equations we replace the terms $t, v_x, v_y, v_z, x, y, p$ by $(L/U)t, Uv_x,\ Uv_y, Vv_z, Lx, Ly, h_0 z, p_s p$ where the latter variables are non-dimensional and V is to be chosen. From the continuity equation we obtain,

$$0 = \frac{U}{L}\rho_{,t} + \frac{U}{L}(\rho v_x)_{,x} + \frac{U}{L}(\rho v_y)_{,y} + \frac{V}{h_0}(\rho v_z)_{,z}. \tag{2.22}$$

Rearranging the above equation we obtain,

$$0 = \rho_{,t} + (\rho v_x)_{,x} + (\rho v_y)_{,y} + \frac{V}{\varepsilon U}(\rho v_z)_{,z}, \tag{2.23}$$

where $\varepsilon = h_0/L$. Then, an evident choice for V is $V = \varepsilon U$. As part of the lubrication approximation, we assume the pressure gradient balances the viscous forces, so we choose $p_s = \mu UL/h_0^2$ to balance the term $\mu v_{x,zz}$ in the momentum equation (2.21). Making the same replacements of dimensional variables by non-dimensional ones in the momentum equations and letting, $Re = \rho U h_0/\mu$, we obtain, after rearranging,

$$-p_{,x} + \frac{(\mu+\lambda)}{\mu}\varepsilon^2(v_{x,xx} + v_{y,yx} + v_{z,zx}) + \varepsilon^2(v_{x,xx} + v_{x,yy}) + v_{x,zz} = Re\varepsilon(v_{x,t} + v_{x,x}v_x + v_{x,y}v_y + v_{x,z}v_z), \tag{2.24a}$$

$$-p_{,y} + \frac{(\mu+\lambda)}{\mu}\varepsilon^2(v_{x,xy} + v_{y,yy} + v_{z,zy}) + \varepsilon^2(v_{y,xx} + v_{y,yy}) + v_{y,zz} = Re\varepsilon(v_{y,t} + v_{y,x}v_x + v_{y,y}v_y + v_{y,z}v_z), \tag{2.24b}$$

$$-p_{,z} + \frac{(\mu+\lambda)}{\mu}\varepsilon^2(v_{x,xz} + v_{y,yz} + v_{z,zz}) + \varepsilon^4(v_{z,xx} + v_{z,yy}) + \varepsilon^2 v_{z,zz} = Re\varepsilon^3(v_{z,t} + v_{z,x}v_x + v_{z,y}v_y + v_{z,z}v_z). \tag{2.24c}$$

Typical dimensions for the air bearing are: $h_0 = 10^{-8}\,m, L = 10^{-3}\ m, \mu = 1.80610^{-5}\ Pa \cdot s, U = 10\,m/s, \rho{\sim}1\,Kg/m^3$, so $\varepsilon = 10^{-5}$, $Re = 5.5(10^{-4})$. Also, typical dimensions for a PFPE lubricant used in HDDs are: $h_0 = 1e-9\,m, L = 1e-3\,m, \mu = 1\,Pa \cdot s, U = 10\,m/s, \rho{\sim}2000\,Kg/m^3$, so $\varepsilon = 10^{-6}, Re = 20(10^{-6})$ [23]. Therefore, for the air bearing model of a hard disk drive it is reasonable to neglect terms of order larger than ε^2 or εRe in the momentum equation (2.24). Then we obtain,

$$-p_{,x} + v_{x,zz} = 0, \tag{2.25a}$$

$$-p_{,y} + v_{y,zz} = 0, \tag{2.25b}$$

$$-p_{,z} = 0. \tag{2.25c}$$

The dimensional scales for shear and normal stresses are determined from equation (2.17), i.e.

$$T_{xz} = \mu\left(v_{x,z} + v_{z,x}\right), \tag{2.26a}$$

$$T_{xz} = \mu\left(v_{x,z} + v_{z,x}\right), \tag{2.26b}$$

$$T_{zz} = -p + \lambda\left(v_{x,x} + v_{y,y} + v_{z,z}\right) + 2\mu v_{z,z}. \tag{2.26c}$$

To non-dimensionalize these equations, we replace T_{xz}, T_{yz}, T_{zz} by the non-dimensional variables $(\mu U/h_0)T_{xz}$, $(\mu U/h_0)T_{yz}$, $p_s T_{zz}$ chosen to balance $\mu v_{x,z}$, $\mu v_{x,z}$, p respectively. Thus we obtain,

$$T_{xz} = v_{x,z} + \varepsilon^2 v_{z,x}, \tag{2.27a}$$

$$T_{yz} = v_{y,z} + \varepsilon^2 v_{z,y}, \tag{2.27b}$$

$$T_{zz} = -p + \frac{\lambda}{\mu}\varepsilon^2\left(v_{x,x} + v_{y,y} + v_{z,z}\right) + 2\varepsilon^2 v_{z,z}. \tag{2.27c}$$

We neglect the small terms of order ε^2 to obtain the approximated non-dimensional stress,

$$T_{xz} = v_{x,z}, \tag{2.28a}$$

$$T_{yz} = v_{y,z}, \tag{2.28a}$$

$$T_{zz} = -p. \tag{2.28c}$$

Equations (2.25) and (2.28) constitute the lubrication approximation framework for the slider-disk system [24].

2.5 Reynolds lubrication equation for compressible fluids

Now we consider the boundary value problem of the air bearing slider shown in figure 2.8. The equations governing this problem are given by (2.25) and (2.28). It is convenient to write equations (2.25) in dimensional variables, i.e.

$$-p_{,x} + \mu v_{x,zz} = 0, \tag{2.29a}$$

$$-p_{,y} + \mu v_{y,zz} = 0, \tag{2.29b}$$

$$-p_{,z} = 0, \tag{2.29c}$$

with boundary conditions,

$$on\ z = 0, \qquad v_x = U_x + l v_{x,z}, \qquad v_y = U_y + l v_{y,z}, \qquad v_z = 0, \tag{2.30a}$$

$$on\ z = h(x,y), \qquad v_x = -l v_{x,z}, \qquad v_y = -l v_{y,z}, \qquad v_z = 0, \tag{2.30b}$$

$$at\ x = 0, L, \qquad y = 0, W, \qquad p = p_0, \tag{2.30c}$$

where p_0 is the ambient pressure, l is Maxwell's slip length [25] and W is the slider's width. In kinetic theory the slip length is a function of pressure and can be written as,

$$l = a\lambda(p) = \frac{D}{p}, \tag{2.31}$$

where λ is the air mean free path which is inversely proportional to the air pressure p with constant of proportionality D, and a is an accommodation factor [26].

When the head-disk spacing is comparable to the air mean free path, the continuum hypothesis is a questionable assumption. The mean free path of air molecules is about λ = 65 nm at ambient pressure and temperature. The minimum slider-disk spacing, h, for a typical ABS design is of the order of 10 nm. The ratio Kn = λ/h, known as Knudsen number, plays an important role in lubrication theory. As observed in [7, 117], the continuum approach is sufficiently accurate for dense gases in the range Kn < 0.01, while the kinetic theory applies for rarefied gases in the range Kn > 10. However, empirical evidence suggests that the applicability of the continuum equations can be extended to the regime 0.1 < Kn < 10 by using first-order and higher order velocity slip conditions [118-120]. A more accurate description of molecular slip for rarefied gases can be obtained from the linearized Boltzmann equation [121-122]. The governing equation thus obtained is known as the molecular gas lubrication (MGL) equation. The solution of the MGL equation is implemented in the CMLAir air bearing solver and was used in this thesis for chapters 4 and 5, while in chapters 6 and 7 we used a first order slip model. The results obtained using a first order slip model are within 4 % of those obtained with the MGL equation.

The velocity gradient is obtained by integrating equations (2.29a), (2.29b) once with respect to z,

$$v_{x,z} = \frac{1}{\mu} p_{,x} z + b_1, \tag{2.32a}$$

$$v_{y,z} = \frac{1}{\mu} p_{,y} z + c_1. \tag{2.32b}$$

Integrating again with respect to z we obtain the velocity profile,

$$v_x = \frac{1}{2\mu} p_{,x} z^2 + b_1 z + b_2, \tag{2.33a}$$

$$v_y = \frac{1}{2\mu} p_{,y} z^2 + c_1 z + c_2. \tag{2.33b}$$

Using boundary conditions (2.30a), (2.30b) we obtain,

$$v_x = \frac{1}{2\mu} p_{,x} \big(z^2 - h(z+l)\big) - \frac{U_x (z+l)}{(h+2l)} + U_x, \tag{2.34a}$$

$$v_y = \frac{1}{2\mu} p_{,y} \big(z^2 - h(z+l)\big) - \frac{U_y (z+l)}{(h+2l)} + U_y. \tag{2.34b}$$

Then, we can compute the mass flux, $\boldsymbol{q}$, through a given cross section by integrating equation (2.34) with respect to z,

$$q_x = \int_0^h \rho v_x dz = -\frac{\rho}{12\mu} p_{,x} (h^3 + 6lh^2) + \frac{\rho U_x h}{2}, \tag{2.35a}$$

$$q_y = \int_0^h \rho v_y dz = -\frac{\rho}{12\mu} p_{,y} (h^3 + 6lh^2) + \frac{\rho U_y h}{2}. \tag{2.35b}$$

We have considered the ideal gas law, $p = \rho RT$ in equation (2.35) with R and T constants, so by equation (2.29c) ρ is independent of thickness z. Substituting for ρ and l we obtain,

$$RTq_x = -\frac{p}{12\mu} p_{,x} \left(h^3 + 6\frac{D}{p} h^2\right) + \frac{p U_x h}{2}, \tag{2.36a}$$

$$RTq_y = -\frac{p}{12\mu} p_{,y} \left(h^3 + 6\frac{D}{p} h^2\right) + \frac{p U_y h}{2}. \tag{2.36b}$$

Consider the control volume shown in figure 2.9.

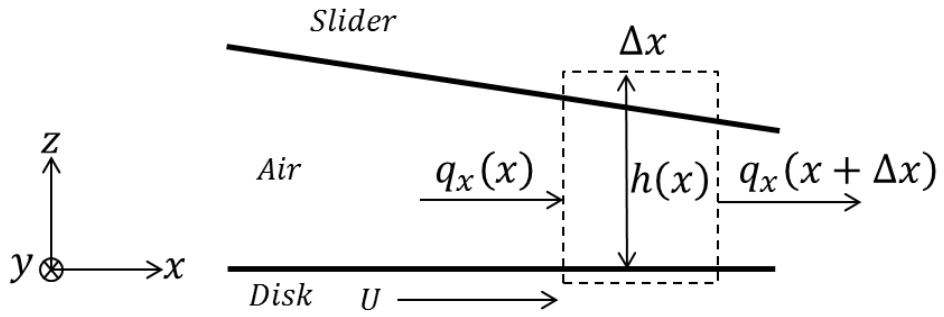

Fig. 2.9. Control volume around the slider-disk system.

A mass balance on this control volume yields the equation,

$$(\rho h)_{,t} + \nabla \cdot \boldsymbol{q} = 0, \tag{2.37}$$

where, $\boldsymbol{q} = (q_x, q_y)$ and $\nabla \cdot$, is the two dimensional divergence operator. Substituting for $\boldsymbol{q}$ and ρ we obtain,

$$(ph)_{,t} - \nabla \cdot \left[\frac{h^2}{12\mu}(6D + ph)\nabla p\right] + \frac{1}{2}\mathbf{U}_d \cdot \nabla(ph) = 0, \tag{2.38}$$

where $\mathbf{U}_d = (U_x, U_y)$ and $\nabla p = (p_{,x}, p_{,y})$. Equation (2.38) is the Reynolds lubrication equation for compressible fluids. We can also compute the stress as given by the dimensional version of equations (2.28).Thus we obtain,

$$T_{xz} = \mu v_{x,z} = \frac{1}{2}p_{,x}(2z - h) - \frac{\mu U_x}{(h + 2l)}, \tag{2.39a}$$

$$T_{yz} = \mu v_{y,z} = \frac{1}{2}p_{,y}(2z - h) - \frac{\mu U_y}{(h + 2l)}, \tag{2.39b}$$

$$T_{zz} = -p. \tag{2.39c}$$

In most cases considered in this dissertation, the y-component of the disk velocity is equal to zero, i.e. $U_y = 0$, so $\mathbf{U}_d = (U, 0)$.

2.6 Reynolds lubrication equation for incompressible fluids

In this section we consider the problem of an incompressible fluid coating the surface of a moving disk as shown in figure 2.10. The traction exerted by the air on the free surface of the liquid is $\boldsymbol{\sigma n}$, were $\boldsymbol{\sigma}$ is the air stress tensor and $\boldsymbol{n}$ is the unit normal to the free surface of the liquid.

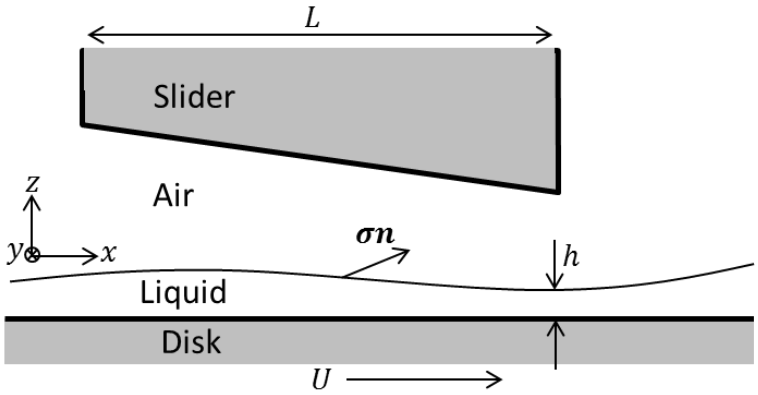

Fig. 2.10. Slider air bearing flying over a moving disk coated with a liquid film.

The momentum equations are the same as those for the compressible case, i.e. equations (2.29). The boundary conditions in this case are,

$$on\ z = 0, \qquad v_x = U_x, \qquad v_y = U_x, \qquad v_z = 0, \tag{2.40a}$$

$$on\ z = h(x,y), \qquad \boldsymbol{Tn} = \boldsymbol{\sigma n}, \tag{2.40b}$$

where $\boldsymbol{T}$ and $\boldsymbol{\sigma}$ are the stress tensors for the liquid and air respectively. In the lubrication approximation $\boldsymbol{n} \approx \boldsymbol{e}_z$, so the boundary condition (2.40b) can be approximated by $T_{xz} = \sigma_{xz}, T_{yz} = \sigma_{yz}, T_{zz} = \sigma_{zz}$. Thus, we can use equations (2.28) to replace the shear stress in the liquid by the liquid velocity gradients. Hence, we write the boundary conditions (2.40) in the form,

$$on\ z = 0, \qquad v_x = U_x, \qquad v_y = U_x, \qquad v_z = 0, \tag{2.41a}$$

$$on\ z = h(x,y), \qquad \mu v_{x,z} = \sigma_{xz}, \qquad \mu v_{y,z} = \sigma_{yz}, \qquad p = \sigma_{zz}, \tag{2.41b}$$

where $\sigma_{xz}, \sigma_{yz}, \sigma_{zz}$ are obtained from equation (2.39) at $z = 0$. The velocity gradient is obtained by integrating equations (2.29) once with respect to z and using boundary condition (2.41b). In this manner we obtain,

$$v_{x,z} = \frac{1}{\mu} p_{,x}(z-h) + \frac{1}{\mu}\sigma_{xz}, \tag{2.42a}$$

$$v_{y,z} = \frac{1}{\mu} p_{,y}(z-h) + \frac{1}{\mu}\sigma_{yz}. \tag{2.42b}$$

Integrating again with respect to z and using boundary condition (2.41a) we obtain the velocity profile,

$$v_x = \frac{1}{\mu} p_{,x}\left(\frac{1}{2}z^2 - hz\right) + \frac{1}{\mu}\sigma_{xz} z + U_x, \tag{2.43a}$$

$$v_y = \frac{1}{\mu} p_{,y} \left(\frac{1}{2} z^2 - hz \right) + \frac{1}{\mu} \sigma_{yz} z + U_y. \tag{2.44b}$$

Then, we can compute the volume flux, $\boldsymbol{q}$, through a given cross section by integrating equation (2.44) with respect to z,

$$q_x = \int_0^h v_x dz = -\frac{1}{3\mu} p_{,x} h^3 + \frac{1}{2\mu} \sigma_{xz} h^2 + U_x h, \tag{2.45a}$$

$$q_y = \int_0^h v_y dz = -\frac{1}{3\mu} p_{,y} h^3 + \frac{1}{2\mu} \sigma_{yz} h^2 + U_y h, \tag{2.45b}$$

Consider the control volume shown in figure 2.11.

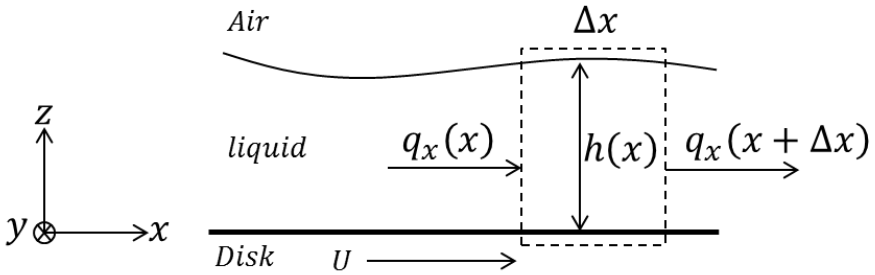

Fig. 2.11. Control volume on the coating film.

A mass balance on this control volume yields the equation,

$$h_t + \nabla \cdot \boldsymbol{q} = 0, \tag{2.46}$$

where, $\boldsymbol{q} = (q_x, q_y)$ and $\nabla \cdot$ is the two dimensional divergence operator. Substituting for $\boldsymbol{q}$ we obtain,

$$h_t + \nabla \cdot \left\{ \frac{h^2}{2\mu} \boldsymbol{\tau} - \frac{h^3}{3\mu} \nabla p \right\} + \mathbf{U}_d \cdot \nabla h = 0, \tag{2.47}$$

where $\boldsymbol{\tau} = (\sigma_{xz}, \sigma_{yz})$, and $\mathbf{U}_d = (U_x, U_y)$. Equation (2.47) is the Reynolds lubrication equation for incompressible fluids. The fluid pressure p is determined by a balance of normal forces at the air-liquid interface as shown in figure 2.4. Then, using the augmented Young-Laplace equation (2.12) [27], $p = p_a - \sigma \Delta h - \Pi(h) = \sigma_{zz}$, for the liquid pressure p in equation (2.12) we obtain,

$$h_t + \nabla \cdot \left\{ \frac{h^2}{2\mu} \boldsymbol{\tau} - \frac{h^3}{3\mu} \nabla [p_a - \sigma \Delta h - \Pi(h)] \right\} + \mathbf{U}_d \cdot \nabla h = 0, \tag{2.48}$$

where p_a is the air pressure as given by equation (2.38) and Δ is the two dimensional Laplace operator.

Chapter 3

Experimental observation and numerical calculation of lubricant reflow after laser heating

In heat assisted magnetic recording (HAMR) technology for hard disk drives, the media is heated to about 500 °C during the writing process in order to reduce its magnetic coercivity and thus allow data writing with the regular magnetic head transducers. The traditional lubricants such as Z-dol and Z-tetraol may not be able to perform in such harsh heating conditions due to evaporation, decomposition and thermal depletion. However, some of the lubricant depletion can be recovered due to reflow after a period of time, which can help to reduce the chance of head disk interface failure. In this chapter, the lubricant reflow process is simulated numerically by solving the governing equations obtained in chapter 2. The numerical results are compared with experiments carried out by Shaomin Xiong and Haoyu Wu from the Computer Mechanics Laboratory. A HAMR test stage was used in the experiments to induce a thermal depletion on a Z-tetraol type lubricant film. Various lubricant depletion profiles were generated using different laser heating conditions. The lubricant reflow process after thermal depletion was monitored by use of an optical surface analyzer (OSA). Reasonably good agreement between simulations and experiments was observed.

3.1 Introduction

In current hard disk drives (HDDs), nanometer-thick lubricant layers are applied to the surface of the media to provide protection against corrosion and reduce friction and wear during accidental slider disk contacts [28]. The lubricant films are synthesized from Perfluoropolyether (PFPE) molecules, e.g., Z-tetraol, which are stable enough to protect the disk at room temperature for at least five years. On the other hand, high magnetic anisotropy materials need to be used to break the limit of superparamagnetism in order to increase storage areal density beyond 1 Tb/in^2. The magnetic state of this kind of media is so stable at room temperature that current magnetic transducers are not able to switch its orientation. Therefore, heat assisted magnetic recording (HAMR) technology [29-30] has been proposed to solve this problem. In HAMR, the magnetic layer is heated up to its Curie temperature with a laser, reducing the magnetic coercivity of the media and allowing data writing using regular magnetic transducers.

Since the lubricant layer is on top of the disk surface, it will be locally heated to a temperature similar to that of the magnetic layer. Such high temperatures can damage traditional lubricants and reduce their lifetime due to evaporation, decomposition and thermal depletion [31-32]. However, it is possible to recover some of the lubricant depletion due to reflow after some period of time. The reflow process helps to cure the lubricant depletion and reduce the chance of head disk interface (HDI) failure. It is therefore important to understand the mechanisms and characteristics of the lubricant reflow for HAMR systems.

3.2 Experimental procedure

A free space laser stage was built in the Computer Mechanics Laboratory by Shaomin Xiong and Haoyu Wu to provide HAMR-like heating conditions on the disk and thus study the lubricant depletion and reflow processes. The test stage contains three main parts: an illumination module that generates a laser beam with different power levels and focus the laser spot onto the disk with

a size of a few microns, a spindle stage that spins the disk at a controlled speed, and a servo motor that controls the radial movement of the laser spot. A schematic drawing of the test system is shown in figure 3.1.

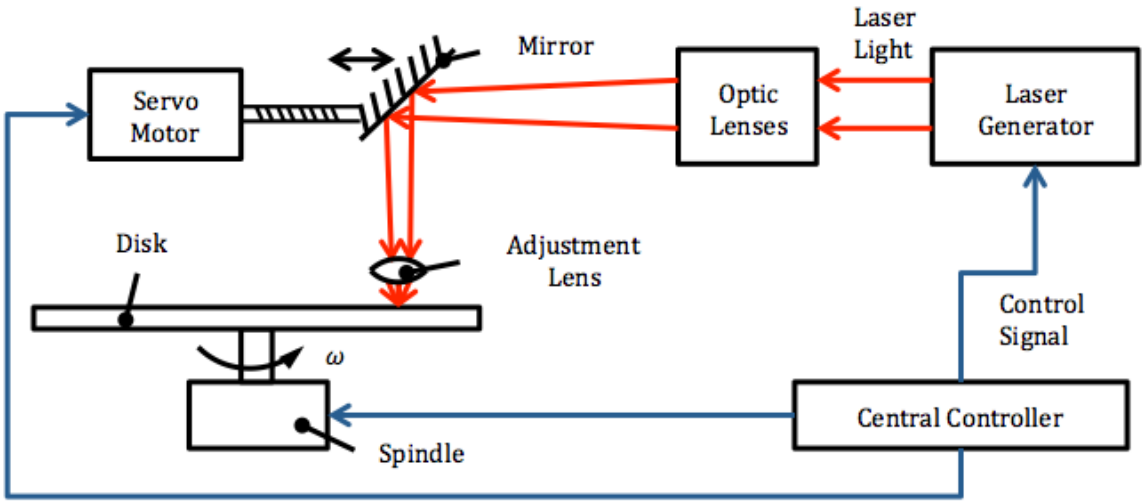

Fig. 3.1. Test stage for HAMR-like heating conditions.

As shown in figure 3.1, a *Central Controller* governs the *Spindle*, the *Laser Generator*, and the *Servo Motor*. A *Laser Generator* shines a laser light over the spinning disk and the *Servo Motor* controls the objective lens such that different tracks on the disk can be exposed to the laser. The laser spot generated from the illumination module heats up the disk to provide HAMR-like conditions. Commercial Perpendicular Magnetic Recording (PMR) disks are used in all experiments. The disks are 3.5 inches in diameter with aluminum substrates. The lubricant type is Ztetraol with A20H additives, and film thickness of 9.5 Å. The disk is exposed to the laser at a constant power P_L, while spinning at a constant angular velocity ω. We shine the laser on different tracks of the disk for time periods corresponding to 1000, 500, 100, 50, 10, 5, 1 disk revolutions respectively. We denote the number of disk revolutions during laser heating by n_L.

Soon after the disk is exposed to the laser, the disk is measured by an optical surface analyzer (OSA Candela). The Q-Phase channel of the OSA Candela is used to measure changes in lubricant thickness [33]. Scans by the OSA are taken periodically at room temperature with time intervals of 95 s up to a total time of 22 min. A final scan is also taken after 24 h to observe the steady state of the lubricant.

3.3 Lubricant reflow process

Following the experimental procedure described in section 3.2, the lubricant profile at different times after laser heating were obtained using the OSA scanner. Some of these images are shown in figure 3.2.

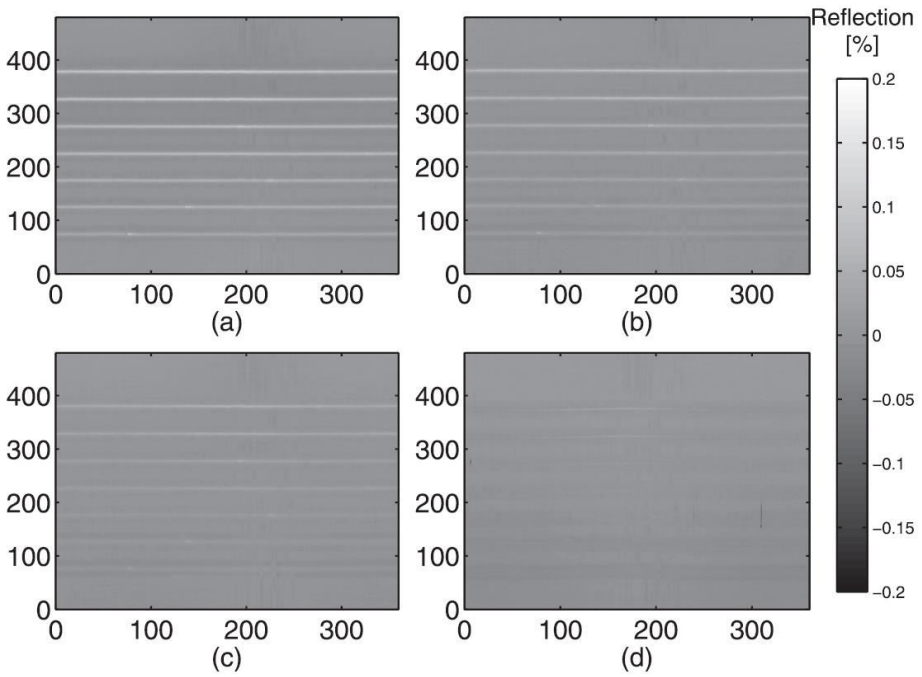

Fig. 3.2. OSA scanning images which show the relative reflectivity on a disk after laser heating at time: (a) 0 min, (b) 3 min, (c) 9 min, and (d) 24 h. The x-axis is the angular position on the disk in degrees. The y-axis is the relative radial position on the disk in μm. In the seven tracks shown in each image we used, from top to bottom, $n_L =$ 1000, 500, 100, 50, 10, 5, 1, revolutions respectively.

As seen in figure 3.2a, the parallel horizontal lines represent the tracks exposed to laser heating for different n_L. The increase of reflectivity in the Q-Phase indicates a decrease in lubricant thickness (depletion). As shown in figure 3.2a the top tracks have a larger change of reflectivity, i.e. a larger n_L which results from significantly more lubricant depletion. Figures 3(b) and 3(c) show the OSA Q-phase images at time 3 min and 9 min respectively. The reflectivity change of the tracks is smaller when compared to that of figure 3(a), indicating that the lubricant has flowed back into the depleted regions. Figure 3(d) shows the state of the lubricant after 24 h. No apparent reflection was observed when $n_L \leq 100$, which means that the lubricant has recovered back to its initial state. However, when $n_L > 100$, it is still possible to observe changes in reflectivity which indicates that the lubricant depletion was not fully recovered after 24 h of reflow. This final state condition may be due to degradation of the carbon overcoat or magnetic layers [31]. To eliminate possible non-lubricant effects, only those results with $n_L \leq 100$ are discussed below.

Figure 3.3 shows the maximum lubricant depletion depth as a function of time for one set of experiments. The lubricant depletion and reflow profiles were obtained from the OSA Q-phase images, some of which are shown in figure 3.2. The experimental parameters used in figure 3.3 are $\omega = 600\ RPM$ and $P_L = 165\ mW$. The number of disk revolutions during laser heating used is $n_L =$ 100, 50, and 5, respectively. The depletion curve for $n_L = 1$ is too small for a reliable analysis; therefore that result is not presented [34].

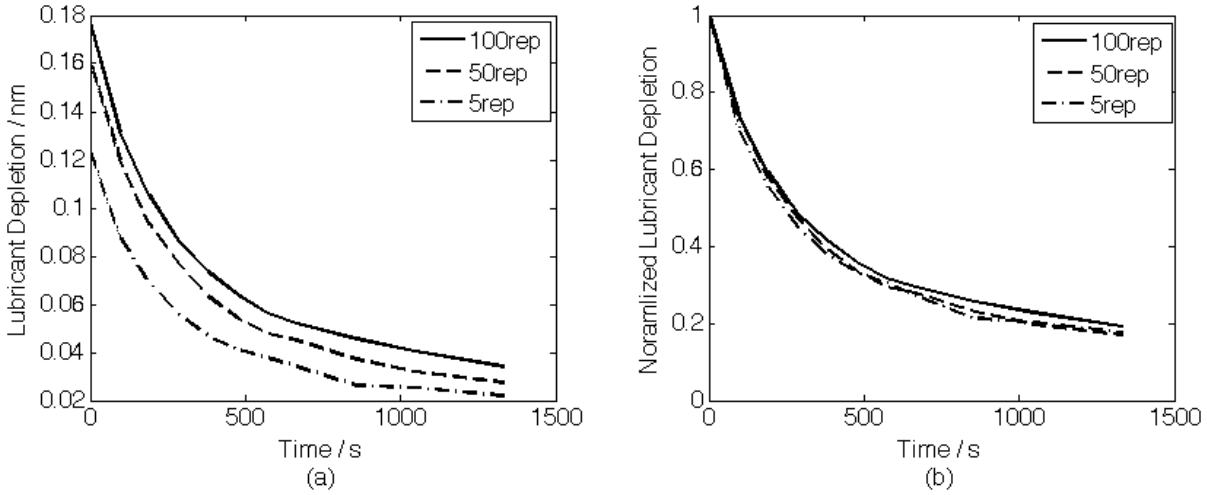

Fig. 3.3. Lubricant relaxation after laser depletion. (a) The three different lines show different laser illumination repetitions. Less repetitions result in shallower initial lubricant depletion. The reflow trends are similar for the three different conditions. (b) Lubricant depletion normalized with respect to initial value. The depletion is set to 1 at t=0. Similar trends are shown.

As shown in figure 3.3a, the lubricant depletion is more severe when the disk is heated for larger n_L. Figure 3.3b shows the lubricant depletion curves normalized by their initial value. From this figure it is observed how the lubricant depletion decreases with time, which indicates that lubricant from other regions of the disk flows back into the depleted area. The reflow rate is initially fast but decreases with time. Almost 80% of the lubricant recovers within 20 min of relaxation at room temperature.

3.4 Comparison between simulation and experiments

In this section we perform simulations of lubricant reflow to compare the results with the experimental ones reported in previous section. The lubricant reflow is described using continuum theory with a modified (effective) viscosity [35]. Within the continuum approach, the dimensions of the thin film on the disk surface make it possible to use lubrication theory in one dimension. We adapt equation (2.48) for the one dimensional case and fixed disk. Thus we obtain the governing equation

$$\frac{\partial h}{\partial t} + \frac{1}{3\mu}\frac{\partial}{\partial x}\left[h^3 \frac{d\Pi(h)}{dh}\frac{\partial h}{\partial x}\right] = 0, \tag{3.1}$$

where $h = h(x,t)$ is the film thickness, μ is the effective lubricant viscosity, $\Pi(h)$ is the disjoining pressure arising from van der Waals interactions between the lubricant and the solid substrate [36]. This disjoining pressure is modeled as $\Pi(h) = Ah^{-3}$, where A is the Hamaker constant. The initial condition is given by the lubricant depletion profile obtained in the experiments at time $t = 0\ s$. As boundary conditions, we consider zero flow at the right and left boundaries. This condition is equivalent to setting $dh/dx = 0$ on the boundaries. It can be observed that equation (3.1) depends only on the ratio of the Hamaker constant to lubricant viscosity. This ratio is adjusted to give the best match for the experimental results. The simulation results of lubricant reflow for $n_L = 100$ are shown in figure 3.4.

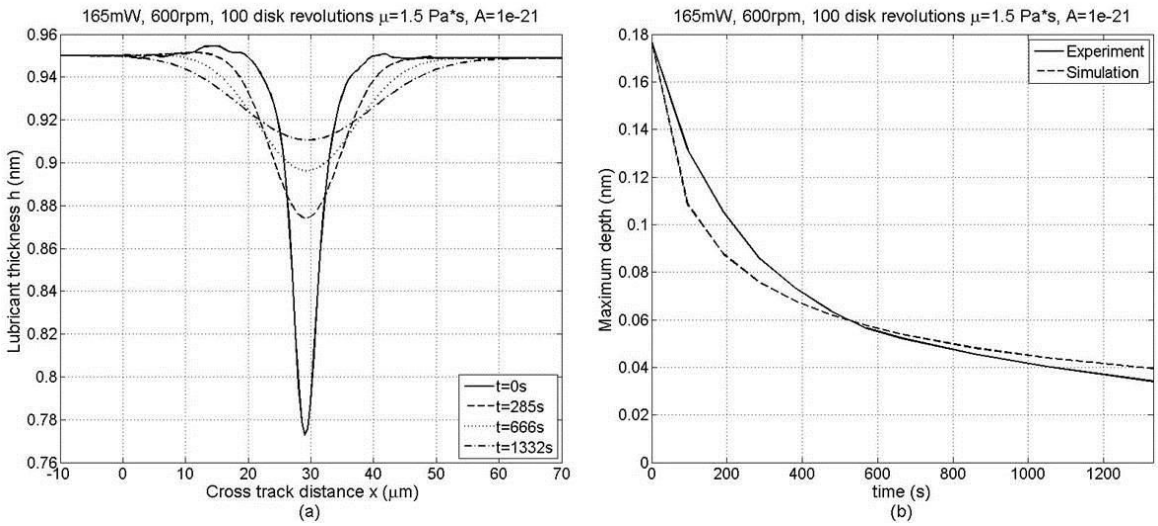

Fig. 3.4. (a) Film thickness profiles at selected times obtained from simulations. (b) Depth of the maximum depletion point in the film as obtained from experiments and simulations. The experiment parameters are $\omega = 600\ RPM$, $P_L = 165\ mW$ and $n_L = 100$. The simulation parameters are $\mu = 1.5\ Pa \cdot s$ and $A = 1 \times 10^{-21}$ J.

It can be seen from figure 3.4b that the simulation results fit fairly well the experimental data. However, there exist regions with some discrepancy. In the first 400 s of reflow, the simulation results show a faster recovery rate than the experiments. After this time, the reflow in the simulation slows down relative to the experiments. This discrepancy may be explained by noting that the lubricant viscosity of thin films can be thickness dependent as discussed in [37]. This phenomenon was not included in the present simulation model. Also the model chosen for the disjoining pressure may not exactly describe the behavior of the particular lubricant used in the experiments.

3.5 Conclusions

In this chapter, the thermal depletion behavior of Z-tetraol due to a free laser beam heating condition as well as the recovery behavior after heating was studied. The initial lubricant depletion was different for different laser heating conditions, i.e., a longer heating duration causes more lubricant depletion. However, a similar trend was found regardless of initial lubricant depletion. Almost 80% of lubricant reflows back within 20 min at room temperature. Simulation results show a reasonably good agreement with experiments.

Real HAMR laser conditions use a near field transducer (NFT) as a heating method to achieve heated spots of tens of nanometers rather than a few microns. So the NFT heating has a spot size a few orders of magnitude smaller and its duration is a few orders of magnitude shorter than our free laser beam heating. Further study needs to be made with NFT heating and HAMR media.

Chapter 4

Numerical simulations of two dimensional lubricant flow on the Air Bearing Surface

In order to achieve high recording densities, the air bearing clearance in a hard disk drive (HDD) has been decreased down to around 2 nm [6]. At this ultra-low spacing lubricant from the disk often transfers to the slider's air bearing surface (ABS) forming a molecularly thin film that imposes a significant disturbance on its flying stability [38-51]. Problems such as head instabilities, disk lubricant depletion and increase in head-disk spacing occur when lubricant is present on the ABS [52-61]. Moreover, it is expected that the lubricant transfer from disk to slider will increase with the use of Heat Assisted Magnetic Recording technology, a possible next generation of HDD [62-66]. To avoid this condition, modern sliders should be able to remove the lubricant from the ABS as fast as possible. Hence, it is necessary to have a thorough understanding of lubricant flow behavior and its driving forces.

The lubricant flow and migration dynamics on the ABS has been the subject of several recent investigations [41, 51, 53, 54, 67, 68, 69]. In [51, 67] the pitch moment and air bearing force were calculated numerically when lubricant droplets are located on the slider's air bearing surface. In [68] the lubricant thickness distribution on the ABS was simulated for diverse slider attitudes and designs. In [41] the lubricant migration on the ABS was computed numerically taking into account the evaporation of lubricant from the slider surface. In [53] there was reasonably good agreement between experiments and modeling of lubricant dynamics on the ABS for a slider at rest and during flying. In [54] the contribution of lubricant on the ABS to magnetic spacing was calculated experimentally and compared with numerical simulations.

In this chapter, we focus attention on the effects of flying height, skew angle and ABS design on the accumulation characteristics of lubricant on the slider's ABS and lateral walls. Our approach is solely numerical based on two-dimensional lubrication theory. The lubricant accumulation outside the ABS is studied by folding down the four lateral walls of the slider, locating them on the same plane with the ABS, then using the two dimensional model mentioned above. Air shear stress, air bearing pressure and disjoining pressure are considered as driving forces in the simulations. The lubricant profile and its volume evolution are calculated for two states of the HDD: operating (flow or outflow) and at rest (reflow). In the first state, lubricant is driven by air shear stress towards the trailing edge of the slider where it accumulates on the so-called deposit end as shown in figure 4.1a. In the second state, lubricant from the deposit end flows back into the ABS driven by the action of disjoining pressure and surface tension as shown in figure 4.1b.

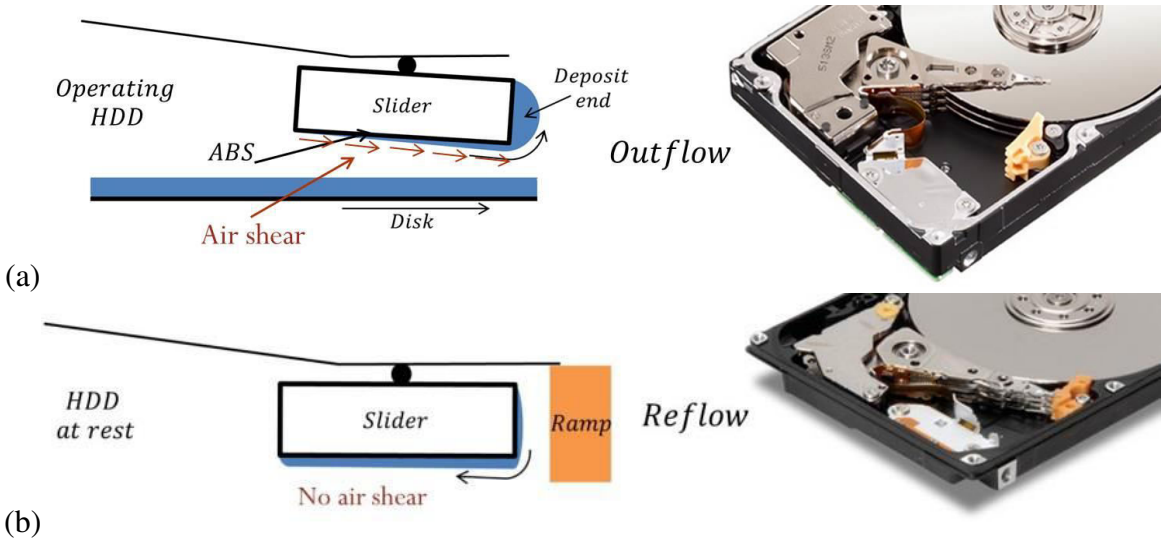

Fig. 4.1. Schematic representation of lubricant migration on the slider surface during (a) flow and (b) reflow.

The governing partial differential equation is solved by means of a finite difference numerical scheme. Four different ABS designs are considered in the numerical simulations to compare the lubricant accumulation characteristics between them. The ABS designs with shorter lubricant removal times are indicated.

4.1 Simulation of lubricant flow and reflow on a slider with fixed attitude

In current HDDs, the thickness of the lubricant film on the disk surface is of the order of 1 nm [18] and of similar order of magnitude on the slider surface when lubricant transfer has occurred [50]. Even though this film consists of only a few molecules across its thickness, the lubricant flow can be well described using continuum theory with a modified (effective) viscosity [70, 35]. This approach yields adequate results when compared with experiments [54]. The value of the effective viscosity can be several orders of magnitude larger or smaller than that of the bulk liquid [71]. Its actual value is strongly dependent on the slider's surface chemistry, roughness and air shear stress intensity. Within the continuum approach, the conditions of operation in a HDD make it possible to use lubrication theory and thus obtain governing equations for the flow on the slider's surface. Hence, we can use equation (2.48) to describe the flow of lubricant on the slider surface. This equation is reproduced here for convenience,

$$h_t + \nabla \cdot \left\{ \frac{h^2}{2\mu} \boldsymbol{\tau} - \frac{h^3}{3\mu} \nabla [p - \sigma \Delta h - \Pi(h)] \right\} = 0, \tag{4.1}$$

where the term $\mathbf{U}_d \cdot \nabla h$ was omitted since the slider is fixed in space, i.e. $\mathbf{U}_d = 0$ in this case. Here, h, μ, p, σ, Π are the lubricant thickness, lubricant viscosity, air pressure, surface tension and disjoining pressure, respectively. The term $\boldsymbol{\tau} = (T_{xz}, T_{yz})$ is the air shear stress. In Eq. (4.1) we have assumed a no-slip boundary condition at the slider-lubricant interface. It is expected that as the film thickness $h \to 0$, slippage at the interface will have a larger contribution to the overall flow; therefore, the assumption of a no-slip condition breaks down. For the thinnest films, slippage can be accounted for by introducing a Navier slip boundary condition in the model [21,72]. Here, the velocity at the solid-liquid interface is proportional to the velocity gradient

into the liquid. The constant of proportionality is the so-called slip length which is not readily available to us from current literature. Consequently, we simplify the analysis by considering only a zero slip condition in the lubrication model.

We want to non-dimensionalize equation (4.1) to obtain relative scales for all the terms involved in it. For this purpose we replace $h, t, x, y, \boldsymbol{\tau}, p, \Pi$ by the non-dimensional variables $h_0 h, t_s t, Lx, Ly, \tau_s \boldsymbol{\tau}, p_s p, \Pi_s \Pi$ where we take $\Pi_s = \Pi(h_0)$ and t_s is to be determined. As done in chapter 2 section 2.4, we take $p_s = \eta UL/u_0^2, \tau_s = \eta U/u_0$ where η, U, u_0 are the air viscosity, disk velocity and referential air bearing spacing. Hence, after clearing dimensions we obtain,

$$h_t + \nabla \cdot \left\{ h^2 \boldsymbol{\tau} - h^3 \nabla \left[C_p p - C_\sigma \Delta h - C_\pi \Pi(h) \right] \right\} = 0, \tag{4.2}$$

where we have chosen $t_s = 2\mu L/(\tau_s h_0)$ and $C_p = 2h_0 p_s/(3L\tau_s)$, $C_\sigma = 2\sigma h_0^2/(3L^3\tau_s)$, $C_\pi = 2h_0\Pi_s/(3L\tau_s)$. Typical dimensions for a PFPE lubricant on a slider flying on air are: $h_0 = 10^{-9}\ m, L = 10^{-3}\ m, \mu = 1\, Pa \cdot s, U = 10\, m/s$, $\sigma = 0.02\, N/m$, $\eta = 1.80610^{-5}\ Pa \cdot s, u_0 = 10^{-8}\, m, \Pi_s = 5.310^6\, Pa$. Hence, obtain the coefficients $C_p = 0.066, C_\sigma = 7.3(10^{-16})$, $C_\pi = 1.9(10^{-4})$. Therefore, we conclude that the surface tension effect is negligibly small compared to the other terms in (4.2). This outcome is also found elsewhere in the literature [73]. For this reason, the Laplace pressure was not implemented in the simulations carried out in this chapter. Thus, in this section we solve the governing equation,

$$h_t + \nabla \cdot \left\{ h^2 \boldsymbol{\tau} - h^3 \nabla \left[C_p p - C_\pi \Pi(h) \right] \right\} = 0. \tag{4.3}$$

For the film characteristics encountered in HDDs, the disjoining pressure is expected to be dominated by van der Waals interactions and expressed by [18]:

$$\Pi(h) = \frac{A}{h^3}, \tag{4.4}$$

where A is known as the Hamaker constant which describes the strength of the van der Waals interactions. This equation is plotted in figure 4.2.

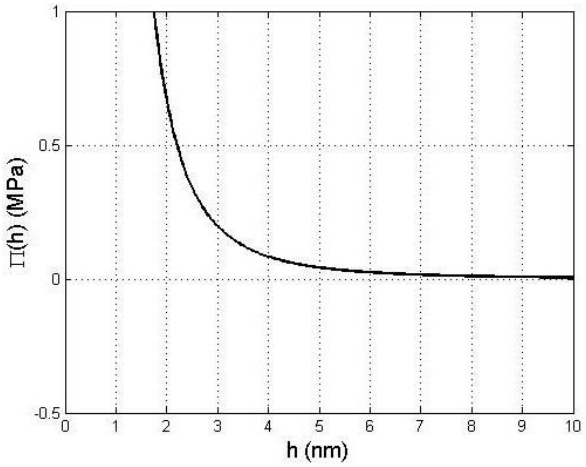

Fig. 4.2. Disjoining pressure $\Pi(h)$ as a function of lubricant thickness h.

There exist an extensive variety of lubricants used in HDDs that differentiate themselves in structural composition, functional end groups and molecular weight. In our study, the values of the material properties were not chosen to match a specific lubricant. However, the chosen values lie within the range of those lubricant properties commonly found in the available literature. Thus, the calculations performed in this chapter were carried out using the material properties: $\mu = 0.144\ Pa \cdot s$ [35], $A = 5(10^{-20})\ J$ [74] . The air bearing pressure and air shear stress fields were calculated using the CMLAir air bearing software [75] which is used to solve equation (2.38). We assumed that the lubricant on the ABS induces a negligible change in air bearing pressure and air shear stress. Therefore, this calculation on CMLAir was carried out only once for each simulation using a slider with no lubricant. In other words, the air shear and air bearing pressure fields are considered to be time independent.

In order to study the lubricant flow and accumulation outside the ABS using the two dimensional model (4.3), we fold down the four lateral walls of the slider (walls parallel to the z direction) locating them on the same plane with the ABS as seen in figure 4.3. By following this approach, the lubricant accumulation on the deposit end as well as on the three other lateral walls can be analyzed.

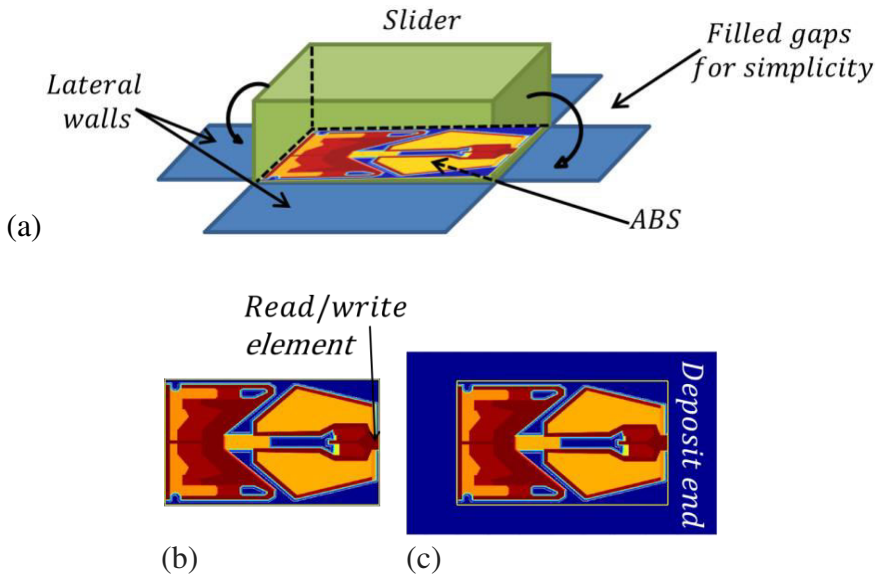

Fig. 4.3. Slider model: (a) lateral walls unfolded, (b) ABS design and (c) ABS with unfolded lateral walls.

Zero volume flow rate is imposed as the boundary condition on the four outer edges. Outside the actual ABS, the air shear stress is set to zero and the air bearing pressure is set to that of the ambient pressure. With these conditions, the lubricant evolution equation (4.3) is solved for h using a second order accurate Crank-Nicolson finite difference scheme [76]. The resulting nonlinear system of equations is solved by a modified Newton's method [77].

We simulate the lubricant migration on the surface of a slider with fixed attitude and compare the results with those obtained when its flying height and skew angle are modified. Two states of a HDD are considered: operation (flow) and rest (reflow). Four different slider designs are employed in the simulations. For the initial condition, we consider a 1 nm lubricant layer lying

uniformly on the slider surface, as seen in figure 4.4 for t = 0 s. Under these conditions, the volume on the ABS is calculated as a function of time.

4.2 Fixed Attitude

The slider's attitude is fixed at a minimum fly height (FH) = 10 nm, skew angle = 0°, pitch angle = 120 μrad, roll angle = 0 μrad. The slider's radial position and disk rotational speed are 18 mm and 5400 rpm, respectively. The simulation results are presented in figure 4.4. The plots show the lubricant film thickness on the slider surface for selected times. Areas of accumulation are clearly observable inside and outside the ABS. In particular, a relatively large lubricant build up is visible near the center of the deposit end, outside the actual ABS. The film thickness on the read/write element is thinner than that on the rest of the slider; however it could be covered by lubricant due to a reflow process once the HDD is at rest as discussed below. Before discussing the reflow process, it is insightful to analyze the individual contribution to the total flow of the second term in equation (4.3), namely the Couette flow due to air shear stress. Then, we calculate the contribution of the third and fourth terms in (4.3) i.e. the Poiseuille flow due to pressure gradients within the lubricant. All terms involve the thickness parameter, h, hence their values change as the lubricant profile evolves with time. To compare them we compute the ratio of the average magnitude of the Couette term, C, to the average magnitude of the Poiseuille term, P, i.e. C/P. The averages are taken only over the ABS since the air shear stress (hence the Couette term) is assumed zero outside the ABS. The ratios at times t = 0 s, 10 s, 100 s, 900 s are C/P= 33.26, 1.10, 0.98, 1.04 respectively. Thus, we observe that initially, when a flat film covers the slider surface, the shear stress dominates largely the flow process. When the flat film deforms, the contribution of pressure gradients to the flow process become more relevant. For times larger than zero in the above calculations, both terms are approximately of the same order of magnitude. Since the Poiseuille term in (4.3) consists of disjoining pressure and air bearing pressure, the latter regarded here as fixed in time, this implies that the disjoining pressure plays a role in the flow process of the same order of importance as the air shear stress.

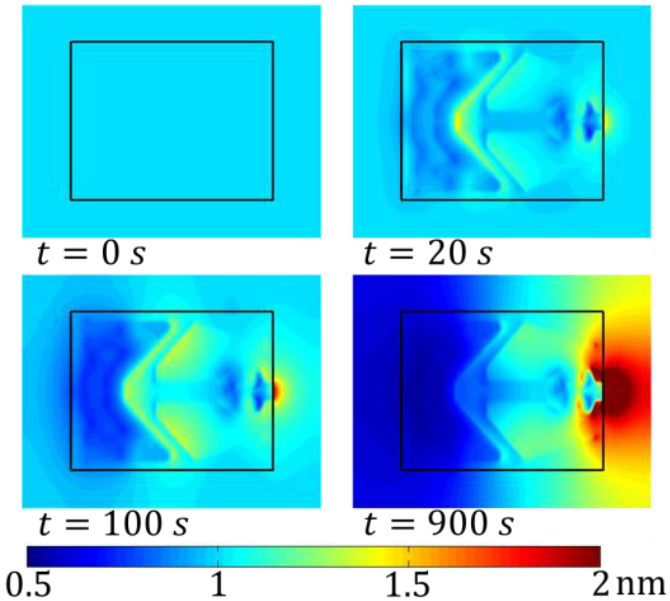

Fig. 4.4. Lube thickness at different times for an operating HDD.

We now simulate the lubricant reflow when the HDD is at rest after 900 s of operation. In this condition, the air bearing pressure and air shear stress are suppressed from the governing equation (4.3). Here, the lubricant is driven only by the action of disjoining pressure. The simulation results are presented in figure 4.5. The plots show the lubricant film thickness on the slider surface for selected times during reflow. It is observed from figure 4.5 that the lubricant accumulated on the deposit end diffuses evenly in all directions due to the action of disjoining pressure. This process drives lubricant from the deposit end back into the ABS, contaminating the read/write element. The lubricant continues to diffuse until the film thickness reaches a steady state at approximately t = 3000 s. The lubricant profile at the final state is almost a uniform film of 1 nm thickness equal to the initial condition shown in figure 4.4 for t = 0 s.

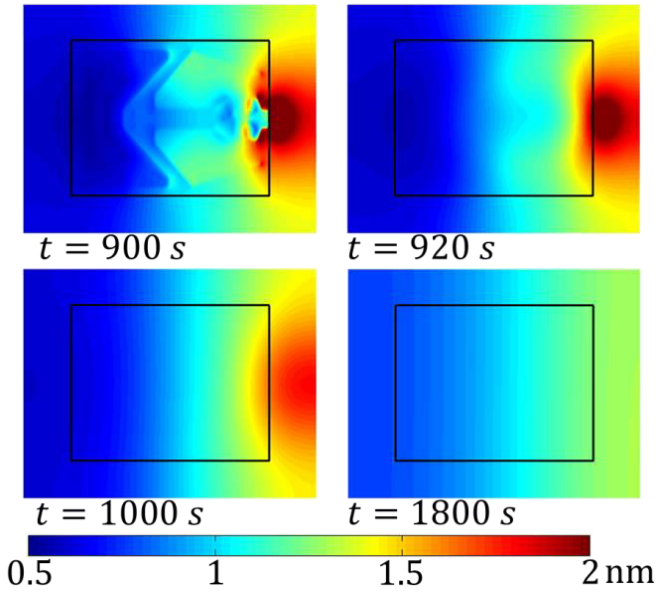

Fig. 4.5. Lubricant thickness profile for a HDD at rest.

4.3 Effect of Flying Height

The effect of flying height on lubricant flow is now considered. Here, we simulate the film evolution on the slider's surface under the same flying conditions given in the previous section but with minimum flying heights of 10 nm, 50 nm, 100 nm and 150 nm. These values were chosen so as to minimize changes in air bearing pressure and air shear stress due to the migration of lubricant on the ABS since, as discussed in section 4.1, the air bearing stress and pressure are assumed fixed in time for each simulation. Calculations are performed for the cases of flow and reflow mentioned above. The results are shown in figure 4.6 where lubricant volume on the ABS is plotted as a function of time. The volume was calculated and normalized only over the actual ABS, i.e. the amount of lubricant on the lateral walls was not included. Therefore, the normalized volume can increase to more than unity due to lubricant from the lateral walls entering into the ABS.

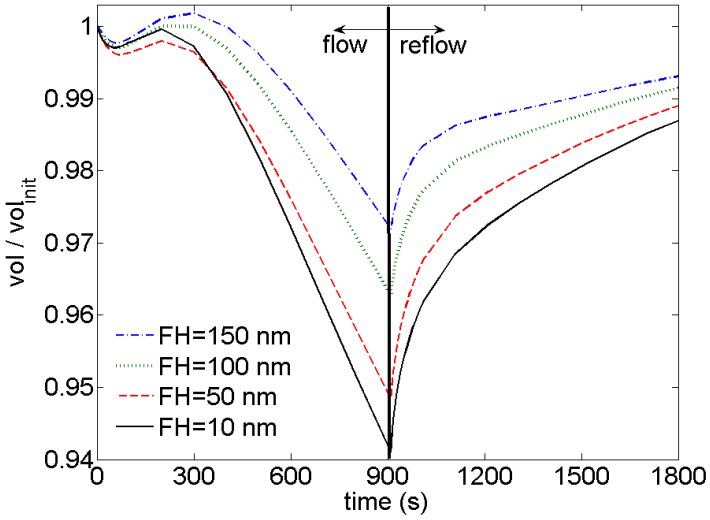

Fig. 4.6. Lubricant volume on the ABS for selected flying heights.

We observe in figure 4.6 that the volume decreases with time during HDD operations (flow). In this case, lubricant is removed from the ABS mainly by the action of the air shear stress. On the other hand, when the drive is at rest (reflow) the volume increases with time due to lubricant from the deposit end flowing back into the ABS driven by disjoining pressure. It is also observed in figure 4.6 that a smaller flying height results in a faster lubricant removal during HDD operations. In particular at t = 900 s, more lubricant is moved out of the ABS as the flying height is reduced. Computing the average air shear stress over the ABS we obtain 127.9 Pa, 111.8 Pa, 98.1 Pa, 88.6 Pa for the minimum flying heights of 10 nm, 50 nm, 100 nm, 150 nm respectively. We note that decreasing the slider's flying height induces an increase in air shear stress that speeds up the lubricant flow process.

4.4 Effect of Skew Angle

To study the effect of skew angle on the lubricant flow we select the following values of skew angle: 15°, 7°, 0°, -7°, -15° as shown in figure 4.7a. In this case, the slider's flying attitude is not fixed, i.e. its flying height, skew, pitch and roll angles are dependent on the radial position of the slider on the disk. The relation among radial position, skew angle and minimum flying height are given in table 1 for the particular HDD configuration considered in our study.

Table 1. Relation among slider's radial position, skew angle, minimum flying height and average air shear stress.

Radius (mm)	Skew (deg)	min FH (nm)	Air Shear (Pa)
25.254	15	6.849	186.30
21.161	7	7.647	155.00
18	0	9.094	131.23
15.311	-7	10.666	112.31
12.83	-15	11.511	95.91

The simulation results are presented in figure 4.7b,c. The plots show the lubricant film thickness on the slider's surface for skew angles of 15°, and -15° at time t = 300 s. It is clear from this figure that one of the effects of skew angle is to mobilize more lubricant towards the sides (top and bottom) of the slider. Moreover, for this particular slider design, the flow process is intensified as the skew angle increases.

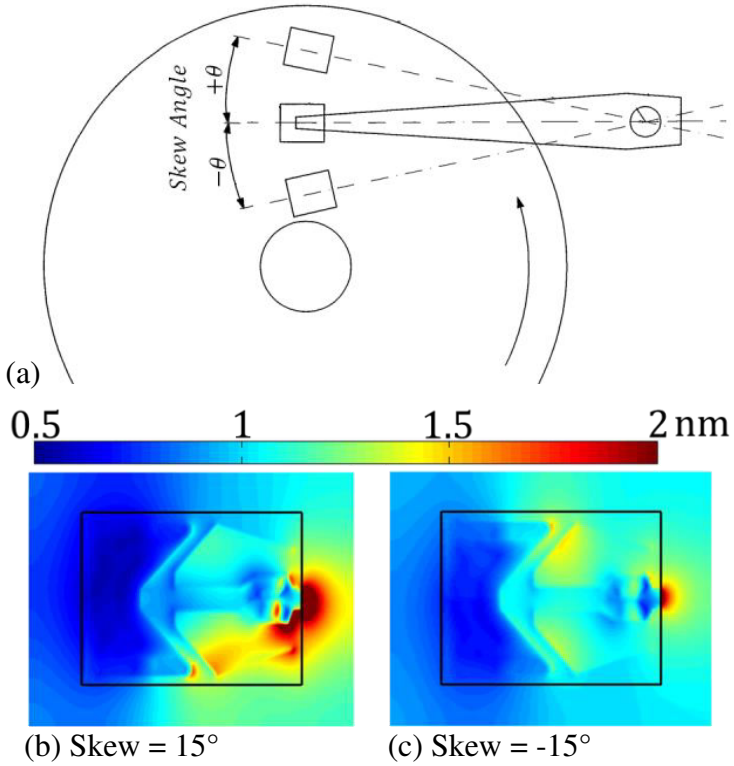

Fig. 4.7. (a) Skew angle definition. Lubricant profiles at t=300 s for skew angles of (b) 15° and (c) -15°.

This is observed clearly in figure 4.8 where the volume of lubricant on the ABS is plotted as a function of time for the selected values of skew angles. The plot shows that, during HDD operations, a faster lubricant removal corresponds to a larger (more positive) value of skew angle, i.e. more lubricant is removed from the ABS as the skew angle increases from negative to positive values.

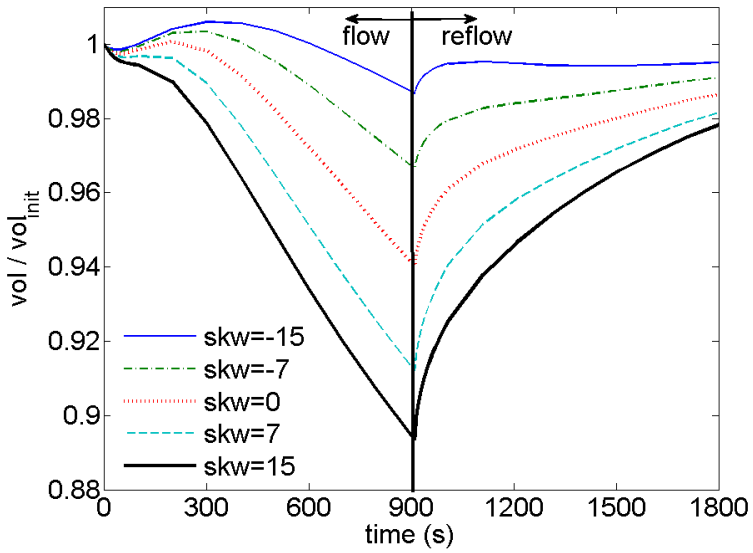

Fig. 4.8. Lubricant volume on the ABS for chosen skew angles.

To explain this behavior, we observe in table 1 that more positive values of skew angle correspond to smaller flying heights (for this particular slider design, figure 3). From table 1, we observe that a reduction in flying height induces an increase in average air shear stress that enhances the flow as discussed in section 4.2.

4.5 Effect of Slider Design

We analyze the effect of slider design on the lubricant migration process. To this end we choose the four ABS designs presented in the first row of figure 4.9. The flying attitude of the four sliders is fixed with the same values given in section 4.2. The plots show the lubricant film thickness on the slider surface at times t = 100 s and t = 900 s. It is observed that the lubricant distribution is slider dependent. In particular, at time t = 900 s, sliders 1 and 4 accumulate a relatively large amount of lubricant near the center of the deposit end, next to the trailing end center pad.

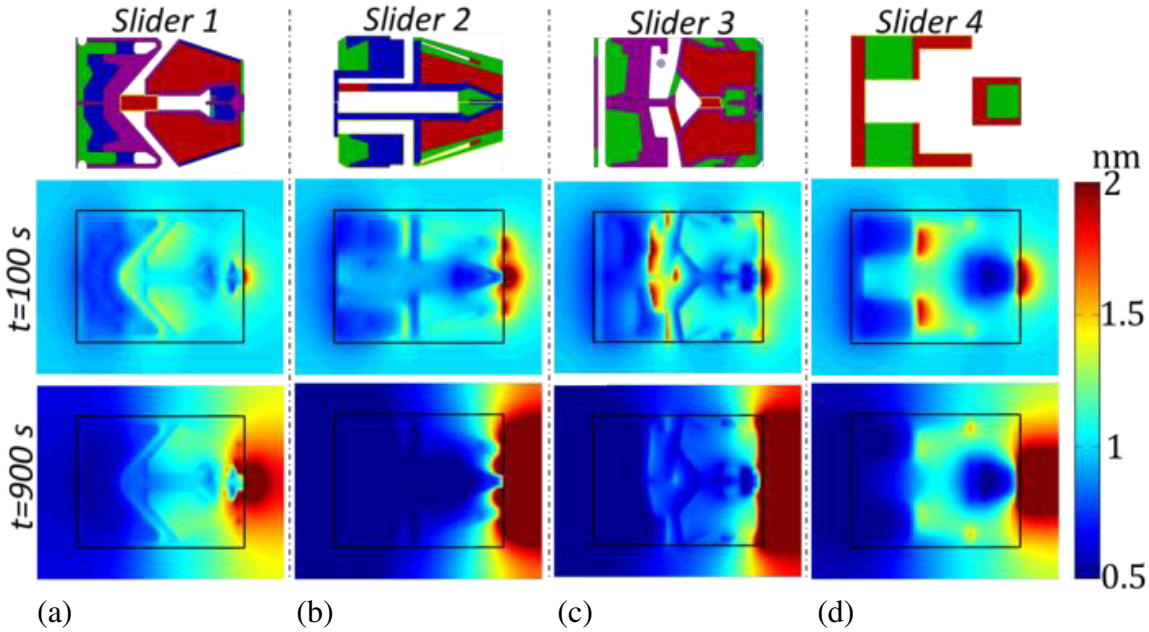

Fig. 4.9. Lubricant thickness profile at times t = 100 s and t = 900 s for chosen ABS designs corresponding to: (a) slider 1, (b) slider 2, (c) slider 3, (d) slider 4.

On the other hand, sliders 2 and 3 spread this lubricant across the width (y direction) of the deposit end, i.e. they have a larger area of distribution. The way in which lubricant is accumulated on the deposit end may have implications on how fast the lubricant is removed from the ABS as discussed below.

In figure 4.10 the lubricant volume on the ABS is plotted as a function of time for the four slider designs. As observed, the curves corresponding to sliders 1 and 4 (and sliders 2 and 3) show similar trajectories, i.e. they are close to each other. Moreover, during HDD operations (flow), sliders 2 and 3 remove more lubricant from the ABS in a shorter period of time than sliders 1 and 4. The average air shear stress over the ABS is 127.9 Pa, 184.3 Pa, 202.4 Pa, and 135.4 Pa for sliders 1, 2, 3 and 4 respectively. We notice that the average air shear stress is larger on sliders 2

and 3 than on sliders 1 and 4. This observation is in agreement with the behavior of the volume plots shown in figure 4.10, namely that sliders 2 and 3 have a faster clean up time.

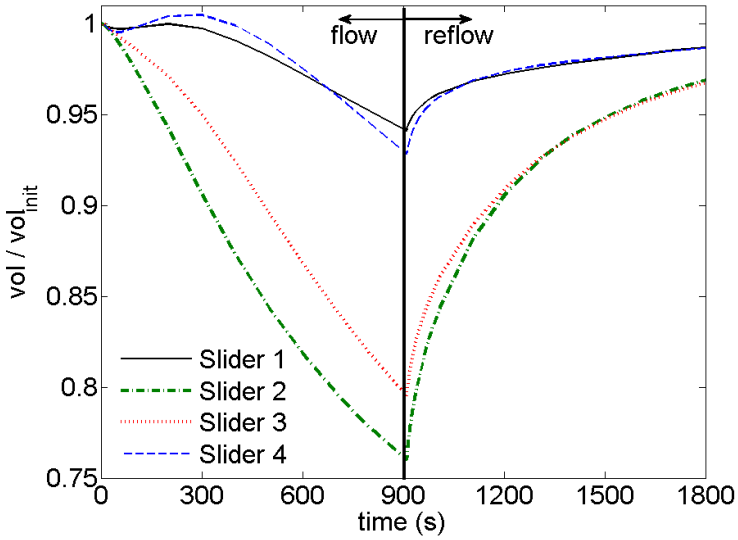

Fig. 4.10. Lubricant volume on the ABS for chosen slider designs.

Since air shearing plays an important role in determining the lubricant flow characteristics, we can gain further insight into the migration process by analyzing the air shear stress profile on the ABS. In figure 4.11, the vector field and intensity of the air shear stress are plotted for sliders 1 and 3. Besides the fact mentioned above, namely that slider 3 has a larger average shear stress than slider 1, we indicate a few important differences between their shear profiles. In figure 4.11a, we note that the magnitude of the air shear stress along the trailing end edge of slider 1 is close to zero except on the center pad where it is the largest. From this characteristic, we expect the largest accumulation of lubricant on the deposit end near the center pad, in agreement with the profile shown in figure 4.9a. Also along this edge we note two regions, above and below the center pad, where air shear is directed towards the interior of the ABS, i.e. approximately along the $-x$ direction. On the other hand, in figure 4.11b we observe that the air shear stress on the trailing edge of slider 3 is all directed away from the ABS towards the deposit end. Moreover, the shear stress magnitude is relatively large, around 300 Pa, all along the trailing edge and it is the largest on the center pad. Here, we expect a large accumulation to exist all along the trailing end on the deposit end, in agreement with figure 4.9c.

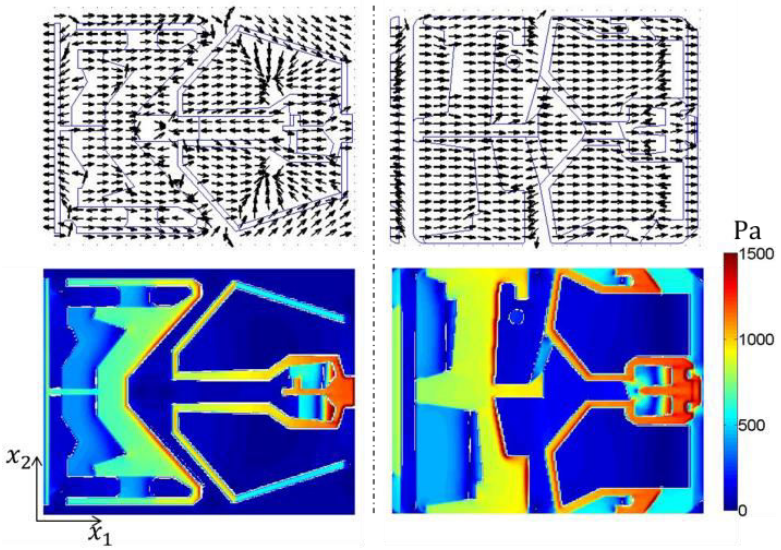

(a) Slider 1 (b) Slider 3

Fig. 4.11. Vector field and magnitude of air shear stress for (a) slider 1 and (b) slider 3.

For the reasons presented above, it is plausible to relate the time for lubricant removal, on a particular slider design, to the magnitude and distribution of the air shear stress on the ABS. These shear stress characteristics determine the extent of area on the deposit end where most lubricant is accumulated. Therefore, we can use the lubricant accumulation profile on the deposit end as an indicator of a slider's speed in removing lubricant from the ABS. As it is observed in figure 4.9a,d accumulation on sliders 1 and 4 occurs largely in a small area near the center of the deposit end and the average magnitude of shear stress is smaller than sliders 2 and 3; therefore lubricant is removed from the ABS at a relatively slow rate which is clearly depicted in figure 4.10. On the other hand, figure 4.9b,c shows that accumulation on sliders 2 and 3 occurs all along the trailing edge on the deposit end and the average shear stress is larger than sliders 1 and 4; consequently lubricant is removed from the ABS at a higher rate as demonstrated in figure 4.10.

4.6 Conclusions

It is shown that the lubricant accumulation characteristics on the slider surface are strongly dependent on the slider's flying height, skew angle and ABS design. The lubricant thickness profile and volume evolution on a slider's ABS are calculated including the effects of air shear stress, air bearing pressure and disjoining pressure as driving forces. Changes in flying height, skew angle and slider design are taken into account in the numerical simulations. It is concluded that a smaller flying height contributes to a faster lubricant removal from the ABS due to an induced increase in air shear stress. It is observed that when the HDD is at rest, lubricant accumulated on the deposit end flows back into the ABS driven by the action of disjoining pressure. It is found, for a particular slider design, that increasing the slider's skew angle has the effect of enhancing the lubricant flow process due to a decrease in the slider's flying height. The lubricant migration process is significantly dependent on the ABS design. It is found that slider designs that accumulate the most lubricant on a broader area on the deposit end and have larger values of air shear stress remove lubricant from the ABS at higher volume rates than those designs where accumulation is concentrated near the center of the deposit end and have smaller values of average shear stress.

Chapter 5

De-wetting on the slider's air bearing surface

5.1 Introduction

In this chapter we investigate the de-wetting behavior of perfluoropolyether (PFPE) lubricant films used in HDDs. As observed in chapter 1, in order to achieve higher recording densities the slider's read/write head should be brought closer to the disk. Currently, the minimum air-bearing clearance in HDDs has been decreased down to around 2 nm. At this ultra-low spacing lubricant from the disk often transfers to the slider's air bearing surface (ABS) forming a molecularly thin film that imposes a significant degradation on its performance. To achieve the future required sub-nanometer clearances, perturbations in the lubricant film need to be kept to less than a few angstroms in thickness [78]. Consequently, it is critical to make accurate predictions of the lubricant response at the head-disk interface in order to engineer reliable HDDs. The accuracy of these predictions relies on a proper understanding and implementation of the lubricant's disjoining pressure. The lubricants used in current HDDs have reactive functional end groups that bond the lubricant to the disk overcoat [79-80] as shown in figure 5.1.

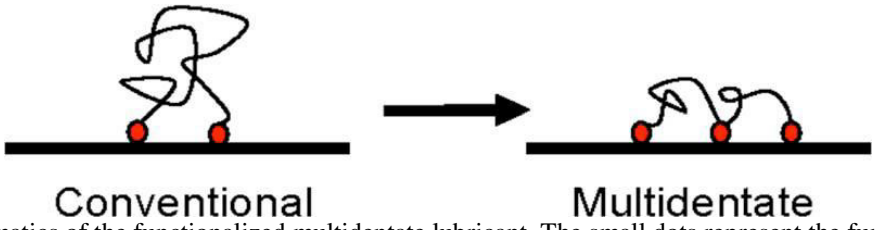

Fig. 5.1. Schematics of the functionalized multidentate lubricant. The small dots represent the functional groups providing adhesive interactions [79].

When these lubricant films reach a critical thickness they become unstable and form either multilayers or droplet structures as shown in figure 5.2 [81-84].

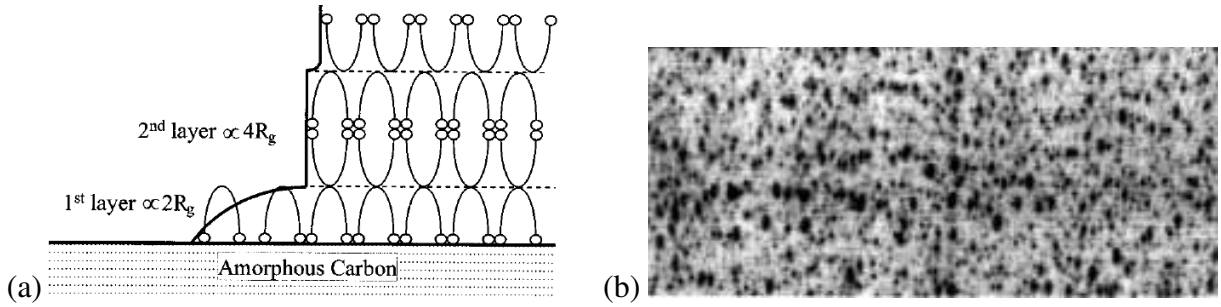

Fig. 5.2. An unstable lubricant film forms either (a) multilayer structures [81], or (b) droplet structures [83].

The above unstable phenomenon on liquid films is known as de-wetting. De-wetting is a process that can occur at a solid-liquid or liquid-liquid interface. Generally, de-wetting describes the rupture of a thin liquid film on the substrate and the formation of droplets [85-89].

The dynamics of nano-scale thin films is determined mainly by their disjoining pressure. Most studies in HDDs consider a disjoining pressure that is due only to van der Waals forces, i.e. $\Pi(h) = Ah^{-3}$. This model provides only a crude estimate for the lubricant behavior. It cannot

predict the motion of liquid films where de-wetting or multilayer formation occurs. Disjoining pressure is generated by diverse forces such as: van der Waals, electrostatic and structural forces; the last one arises from molecules within the film having a structure different from that of the bulk lubricant [90].

5.2 Spreading of a lubricant film with negligible surface tension

We first consider the case of a slider at rest with a uniform lubricant layer on its surface. Since the slider is at rest the air shear stress $\boldsymbol{\tau}$ and air pressure gradient ∇p vanish. As observed in chapter 4, the lubricant flow on a slider with dimension $L = 1\,mm$ is dominated by the disjoining pressure so that the effect of surface tension can be neglected. Therefore, under these conditions the equation of motion (2.12) becomes,

$$h_t + \frac{1}{3\mu}\nabla \cdot \{h^3 \Pi'(h) \nabla h\} = 0. \tag{5.1}$$

We non-dimensionalize this equation by replacing the dimensional variables h, t, x, y, Π by the non-dimensional ones $h_0 h, t_s t, Lx, Ly, \Pi_s \Pi$ where we take $\Pi_s = \Pi(h_0)$ and $t_s = 3\mu L^2/(\Pi_s h_0^2)$ so that the first term in (5.1) balances the disjoining pressure term. Then, the non-dimensional equation is,

$$h_t + \nabla \cdot \{h^3 \Pi'(h) \nabla h\} = 0. \tag{5.2}$$

We first consider the disjoining pressure given by model 2 from table 2.1, i.e.

$$\Pi(h) = a_1 h^{-n} + a_2 h^{-m}, \tag{5.3}$$

with $a_1 = -5.3(10^{-21})\ Nm, a_2 = 6(10^{-30})\ Nm^2,\ n = 3, m = 4$ [91]. This equation is plotted in figure 5.3. The disjoining pressure given by equation (5.3) roughly approximates the behavior of a ZDOL lubricant commonly used in HDDs [92].

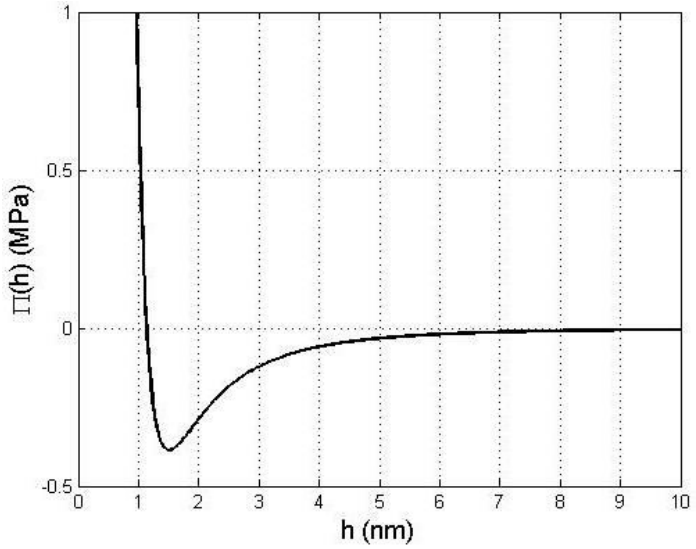

Fig. 5.3. Disjoining pressure as function of film thickness given by model 2 from table 2.1.

We solve equation (5.2) using a finite difference numerical scheme where we use central differences for the spatial derivatives and one sided differences for the time derivative. As boundary conditions we set the restriction $\partial h/\partial n = 0$ on the four walls; this condition is equivalent to imposing a zero volume flux through any of the boundaries. As for the initial condition, we consider a 1.5 nm lubricant layer lying uniformly on the slider surface. And we consider a portion of the slider surface of dimensions $L \times L$. We insert a 1 nm droplet on top of the lubricant to play the role of a disturbance in the film. We use the values $\mu = 1\ Pa \cdot s,\ L = 10^{-3}\ m, h_0 = 10^{-9}\ m, \Pi_s = |\Pi(h_0)|$, hence the resulting time scale for this flow process is approximately $t_s = 3\mu L^2/(\Pi_s h_0^2) = 4.3(10^6)\ s$. The simulation results are shown in figure 5.4.

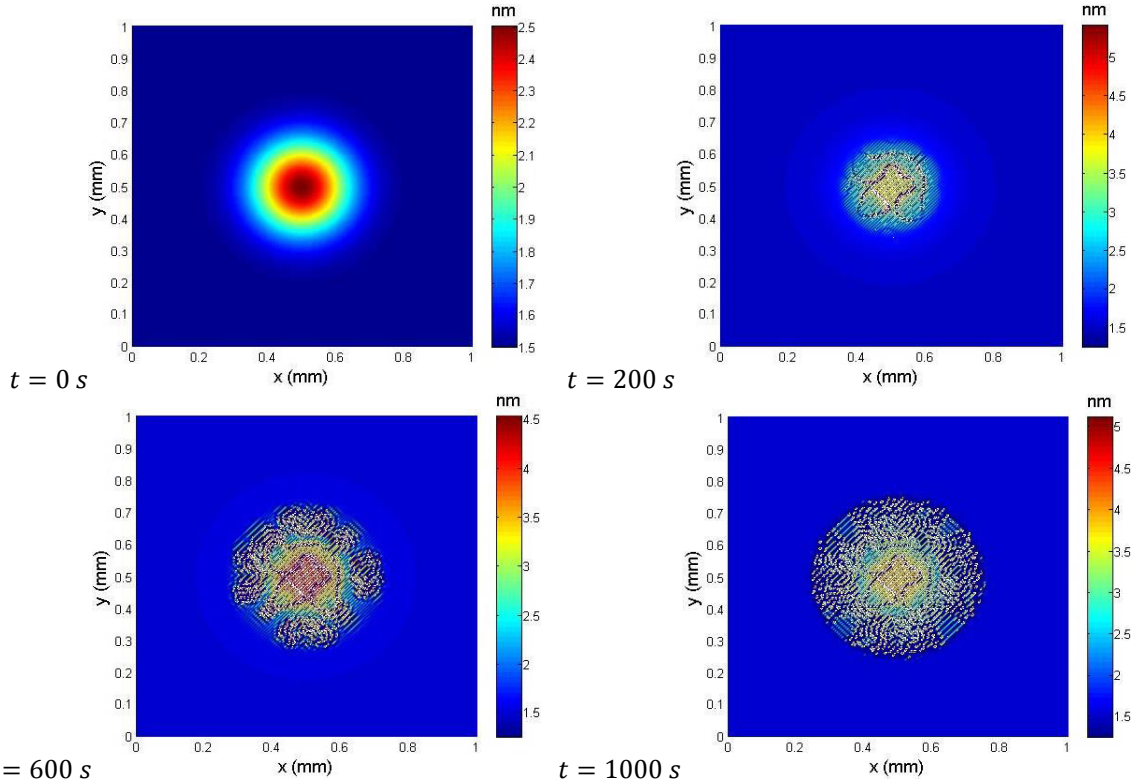

Fig. 5.4. Lubricant thickness profiles of a droplet at times 0 s, 200 s, 600 s, and 1000 s. Surface tension is neglected. Mesh grid size = 5 μm. Disjoining pressure given by model 2 from table 2.1.

Figure 5.4 shows the evolution of the lubricant droplet with time. It is observed that the initial droplet breaks up into smaller droplets which grow to a thickness over 5 nm. The width of each droplet narrows down to the size of the computational grid at which point the solution is no longer valid. To gain insight into the results obtained in figure 5.4 we linearize equation (5.2), around $h = h_0$, to obtain,

$$h_t + k\Delta h = 0, \tag{5.4}$$

where $k = h_0^3\Pi'(h_0)/(3\mu)$. Equation (5.4) is the ubiquitous heat equation which is known to be stable for $k \leq 0$, i.e. when $\Pi'(h_0) \leq 0$ and unstable when $k > 0$, i.e. when $\Pi'(h_0) > 0$ [93]. For the particular choice of disjoining pressure given by (5.3) we find that below (above) $h_0 =$

$1.51(10^{-9})$ m equation (5.4) is stable (unstable). For the initial condition shown in figure 5.4, we observe that the top of the lubricant droplet is in an unstable condition. Hence, from equation (5.4), we expect the height of the droplet to grow continuously until $\Pi'(h) \to 0$ or $\nabla h \to 0$.

We also observe that the width of most droplets shown in figure 5.4 at 1000 s corresponds to the size of the grid used in the numerical simulation, i.e. 5 μm. Motivated by this, we refine the mesh to half the size of the grid size used previously i.e. 2.5 μm. The results are shown in figure 5.5.

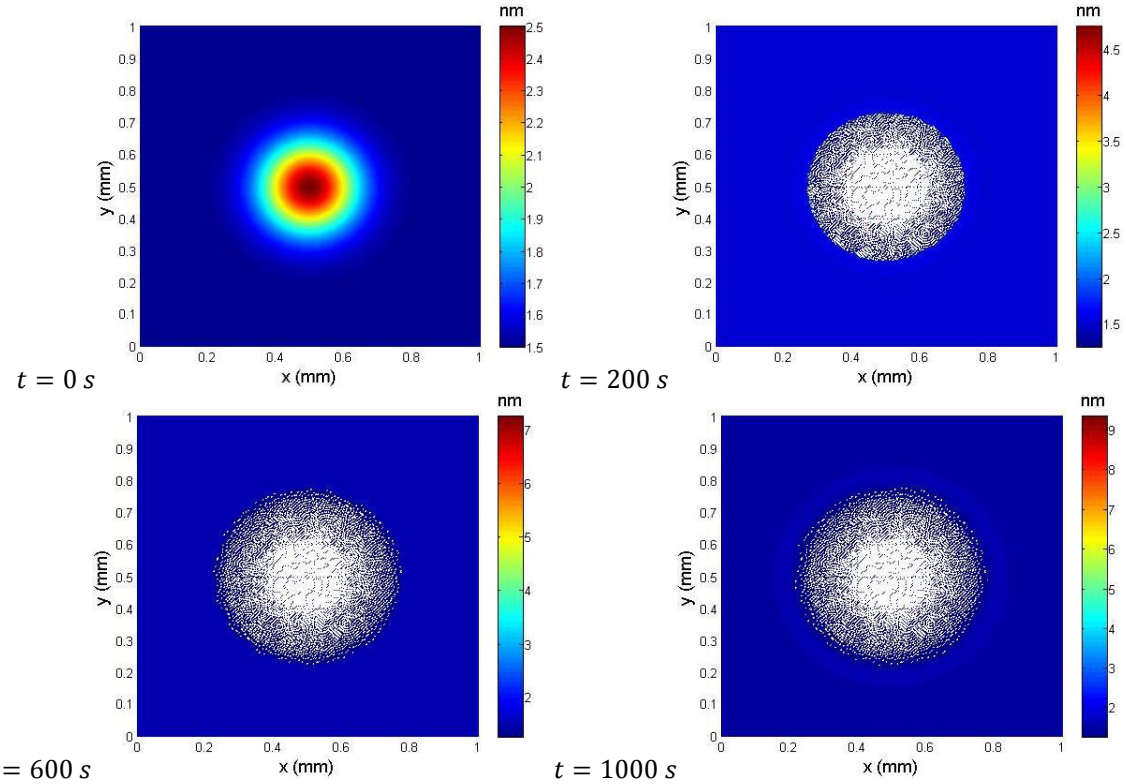

Fig. 5.5. Lubricant thickness profiles of a droplet at times 0 s, 200 s, 600 s, and 1000 s. Surface tension is neglected. Mesh grid size = 2.5 μm. Disjoining pressure given by model 2 from table 2.1.

Again, we observe that the horizontal size (width) of most droplets shown in figure 5.5 at 1000 s corresponds to the size of the grid, refined in this case. We attribute this behavior to the finite difference numerical scheme itself. Consider a point (x, y) in figure 5.5(1000 s) that corresponds to the peak value of an isolated droplet. Hence, approximating the gradient of the thickness, ∇h, by a central difference, we obtain $\partial h(x,y)/\partial x \approx (1/2\Delta x)[h(x+\Delta x, y) - h(x-\Delta x, y)] = 0$, and similarly $\partial h(x,y)/\partial y \approx 0$, since $h(x+\Delta x, y) = h(x-\Delta x, y) = h(x, y+\Delta y) = h(x, y-\Delta y)$ in this case. Therefore, the results shown in figures 5.4 and 5.5 cannot be considered as reliable since it is an artificial consequence of the finite difference scheme. To avoid such a problem we need to include in equation (5.2) the restoring force of surface tension to balance the disjoining pressure when $\Pi'(h) > 0$.

5.3 Spreading of a lubricant film with non-negligible surface tension

Now, we assume that the conditions of the lubricant film and the dimensions of the computational domain are such that surface tension is of significant magnitude so that it balances the disjoining pressure. Hence, the equation of motion (2.12) becomes,

$$h_t + \frac{1}{3\mu}\nabla \cdot \{h^3 \nabla[\sigma \Delta h + \Pi(h)]\} = 0. \tag{5.5}$$

We non-dimensionalize this equation by replacing h, t, x, y, Π by the non-dimensional variables $h_0 h, t_s t, Lx, Ly, \Pi_s \Pi$ where we take $t_s = 3\mu L^4/(\sigma h_0^3)$ and $\Pi_s = \sigma h_0 / L^2$ so that the surface tension term balances the disjoining pressure term. Then, the non-dimensional equation becomes,

$$h_t + \nabla \cdot \{h^3 \nabla[\Delta h + \Pi(h)]\} = 0. \tag{5.6}$$

We solve this equation using the finite difference numerical scheme described above. As boundary conditions we impose the restriction $\partial h/\partial n = 0$ and $\partial^3 h/\partial n^3 = 0$ on the four walls; this condition is equivalent to imposing a zero volume flux through any of the boundaries. We choose the model of disjoining pressure given by equation (5.3). As before, the initial condition is a 1.5 nm lubricant layer lying uniformly on the slider surface with a 1 nm droplet on top of the lubricant to play the role of a disturbance in the film. We use the values $\sigma = 0.02\ N/m$ [94], $\mu = 1\ Pa \cdot s$ [74, 95], $L = 10^{-6}\ m, h_0 = 10^{-9}\ m,$ so the resulting time scale for this flow process is approximately $t_s = 3\mu L^4/(\sigma h_0^3) = 1.5(10^5)\ s$. The simulation results are shown in figure 5.6.

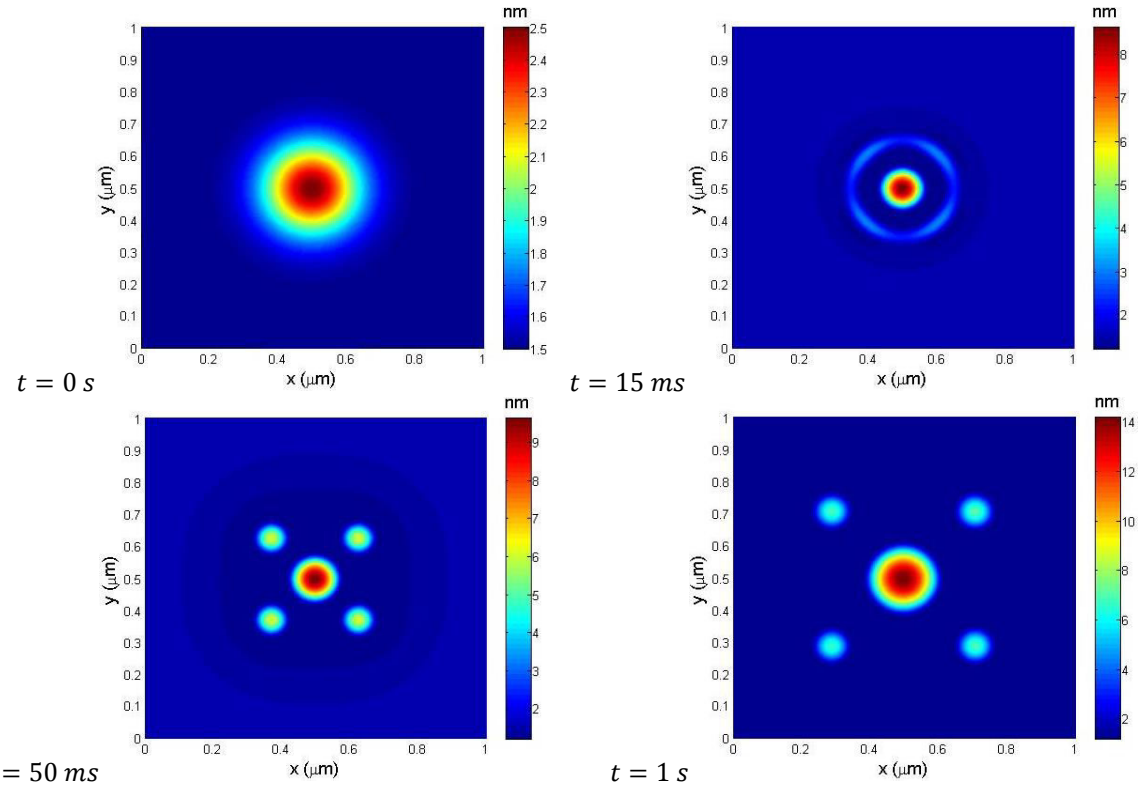

Fig. 5.6. Lubricant thickness profiles of a droplet at times 0 s, 15 ms, 50 ms, and 1 s. Surface tension is included. Disjoining pressure given by model 2 from table 2.1.

From figure 5.6(0 s), we observe that the droplet initially has a thickness larger than $1.51\ nm$ so $\Pi'(h) > 0$. This implies that the state of the droplet is unstable so it starts to increase in thickness as shown in figure 5.6(15 ms). Due to the characteristics of $\Pi(h)$, the droplets continue to grow in height and decrease in width until its curvature is large enough for the surface tension term (Laplace pressure) to balance the disjoining pressure. The initial droplet creates a ring of lubricant around it that eventually breaks up into smaller droplets as seen in figure 5.6(50 ms). The resulting new state is stable since it is energetically more favorable than the initial state [96].

We can also consider, as initial condition, a uniform lubricant layer on the surface of the slider with a thickness of 2.5 nm. In this case the film is already unstable since $\Pi'(h) > 0$ when $h > 1.51\ nm$. We perturb the uniform film by creating a hole, 1 nm depth, in the middle of the domain. The results are shown in figure 5.7.

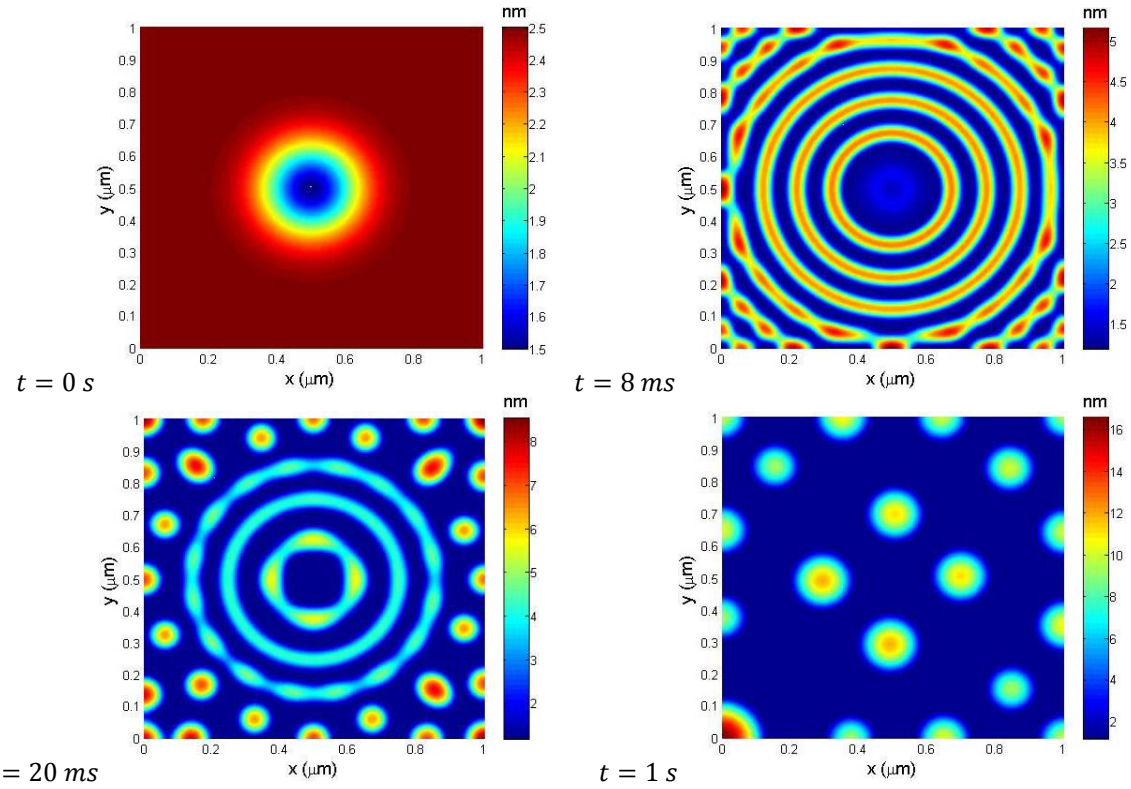

Fig. 5.7. Lubricant thickness profiles of a hole in a uniform film at times 0 s, 8 ms, 20 ms, and 1 s. Disjoining pressure given by model 2 from table 2.1.

From figure 5.7(0 s), we observe that the film, away from the center hole, has a thickness of $2.5\ nm$, i.e. larger than $1.51\ nm$ so $\Pi'(h) > 0$. This implies that the state of the film is unstable. The center hole increases in width as time progresses. This process generates concentric rings around the initial hole which eventually break up into smaller droplets as seen in figure 5.7(50 ms). This action is known as de-wetting [85]. The final state is that of a few isolated lubricant droplets connected by a uniform film with a thickness of $1.18\ nm$, approximately the thickness when $\Pi(h) = 0$ and $\Pi'(h) < 0$ which is $h = 1.13\ nm$ as seen in figure 5.3.

Consider now a multi-dentate type of lubricant such as ZTMD which is commonly encountered in HDDs [58]. An expression for the disjoining pressure of this type of lubricants is proposed in [18] and is given by,

$$\Pi(h) = a_1 h^{-3} + a_2 e^{-a_3 h} + a_4 \cos(a_5 h + a_6)\, e^{-a_7 h}, \tag{5.7}$$

with $a_1 = 5.3(10^{-21})\ Nm$, $a_2 = -1.6(10^6)\ N/m^2$, $a_3 = 5(10^8)$, $a_4 = -10^6\ N/m^2$, $a_5 = 1.57(10^9)$, $a_6 = 3.77$, $a_7 = 2.5(10^8)$. This equation is plotted in figure 5.8.

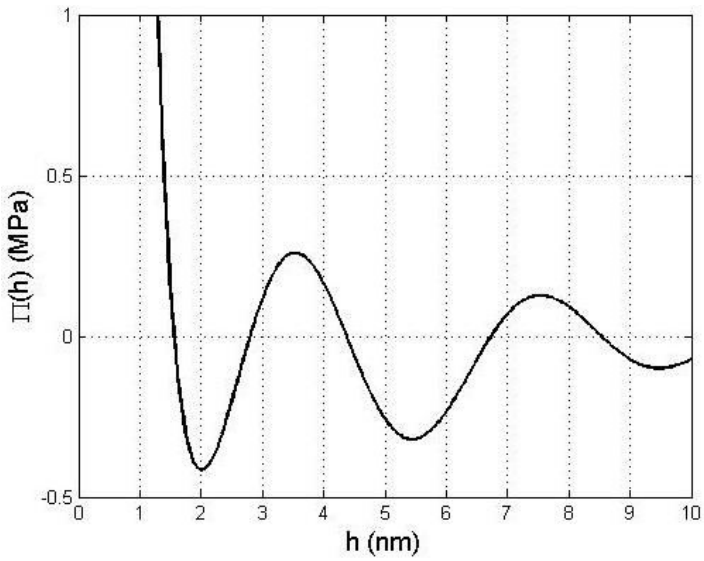

Fig. 5.8. Disjoining pressure as function of film thickness given by model 3 from table 2.1.

We first consider the spreading of a lubricant step lying over the surface of the slider with lateral dimensions $L = 1\ mm$. The step is 20.66 nm in its high part and 1.5 nm in its low part as shown in figure 5.9a. We solve equation (5.6) using the numerical scheme previously described. The simulation results are shown in figure 5.9b. Due to the relatively large lateral dimensions of the slider, relative to the lubricant thickness, surface tension effects are negligible in this case when compared to disjoining pressure effects. As observed in figure 5.9b, after 1000 s the initial lubricant step deforms into a terraced or multilayer structure. The obtained multilayer structure contains 6 visible layers (5 steps). The first layer has a thickness of 1.5 nm, whereas the height of the next layers is: 4.33 nm, 8.53 nm, 12.64 nm, 16.65 nm and 20.47 nm respectively. These heights correspond closely to those points in figure 5.8 where $\Pi'(h) < 0$ and $\Pi(h) = 0$ i.e. the points of stability: 1.55 nm, 4.37 nm, 8.52 nm, 12.59 nm, 16.63 nm and 20.66 nm respectively.

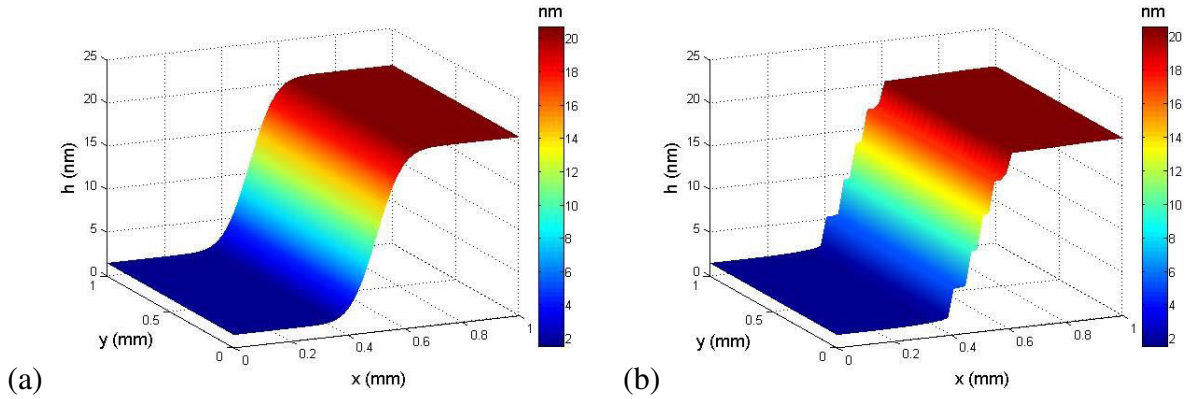

Fig. 5.9. Lubricant thickness for the spreading of a step on the film at time (a) 0 s and (b) 1000 s. Disjoining pressure given by model 3 from table 2.1.

These terraced structures on PFPE lubricants are also observed in experiments which confirm the validity of our results. In [84] the authors investigate the spreading profiles of a Zdol film with a thickness of 15 nm. Their experimental results are shown in figure 5.10.

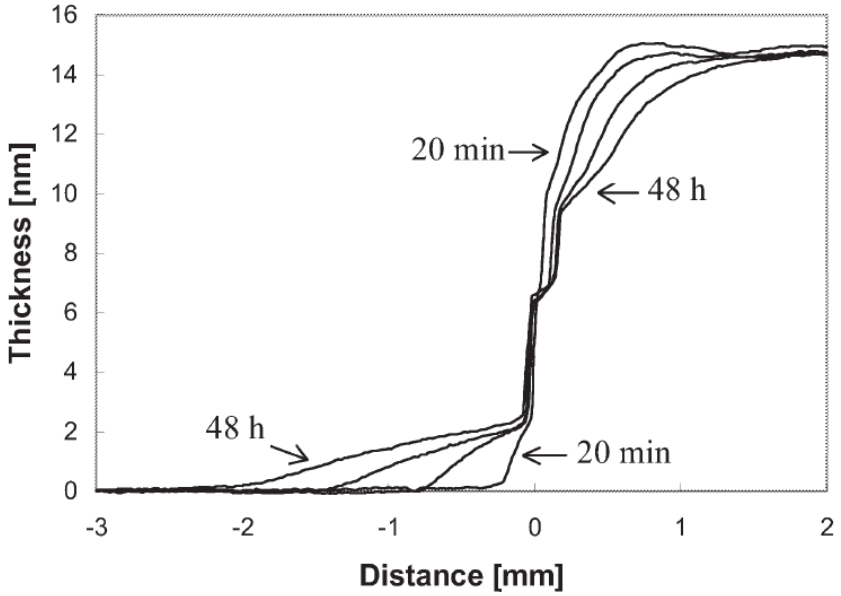

Fig. 5.10. Thickness profiles of Zdol on amorphous carbon, with initial thickness of 15 nm at 20 min, 7 h, 24 h and 48 h [84].

As shown, a complex layered structure develops with time. The development of such a layered structure has been interpreted as a manifestation of a specific surface conformation. As noted in [84], the diffusive first layer develops from the diffusion of Zdol molecules within the first monolayer, with end-groups orienting preferentially towards the carbon surface. The interactions between these molecules and the carbon surface are stronger than intermolecular interactions. Hence, molecules spread like a two-dimensional gas. The second layer is much less mobile and exhibits a sharp step, which has a thickness nearly twice of the first layer. The proposed conformation of this layer was Zdol dimers, having their end-groups connected to each other via hydrogen bonding. These molecules are more strongly influenced by the intermolecular (cohesion) than surface (adhesion) interactions [97].

Now consider a uniform lubricant layer lying on a portion of the surface of the slider with a thickness of 2.5 nm. As before, we perturb the uniform film by creating a hole, 1 nm in depth, in the center of the computational domain. The results are shown in figure 5.11.

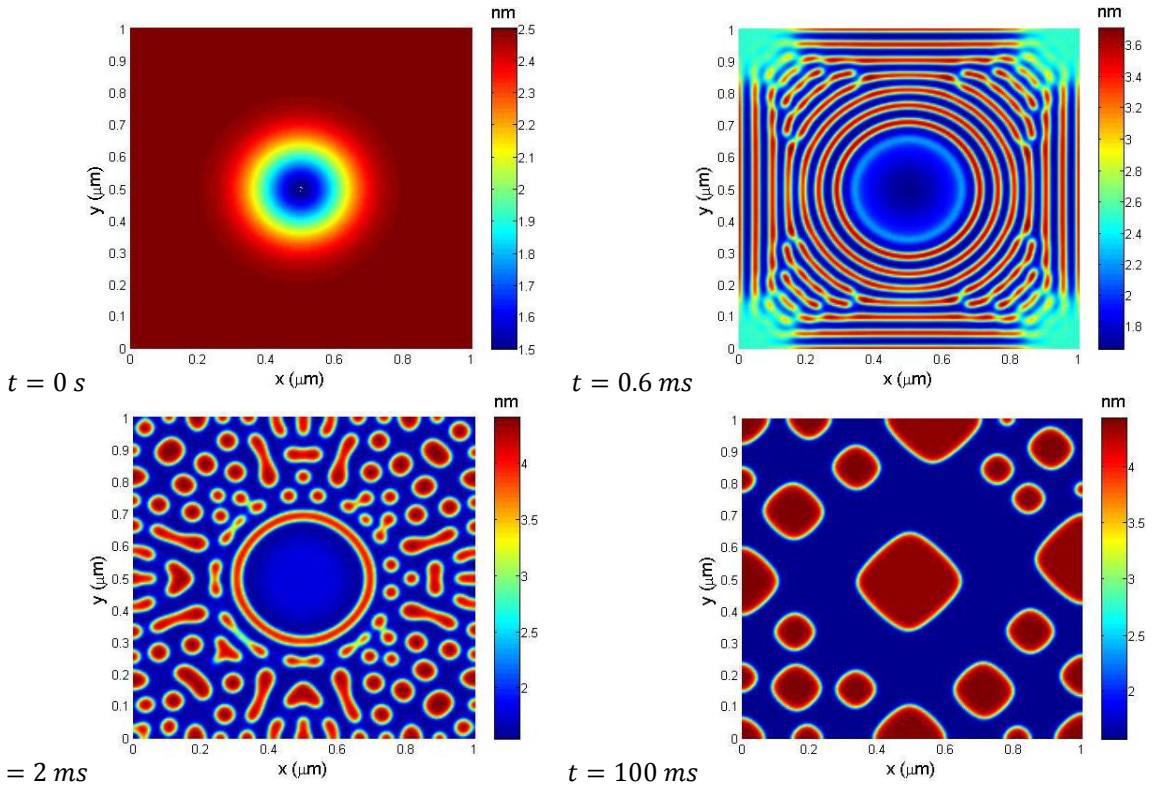

Fig. 5.11. Lubricant thickness profiles of a hole in a uniform film at times 0 s, 0.6 ms, 2 ms, and 100 ms. Disjoining pressure given by model 3 from table 2.1.

From figure 5.11(0 s), we observe that the film, away from the center hole, has a thickness of $2.5\ nm$, i.e. larger than $2\ nm$, so $\Pi'(h) > 0$. This implies that the state of the film is unstable. Similar to the results obtained using the previous disjoining pressure given by (5.3), with this new disjoining pressure given by (5.7) the center hole increases in width as time progresses generating concentric rings around the initial hole. The rings reach the boundary first at the center of the walls and eventually break up into smaller droplets which coalesce into larger ones as seen in figures 5.11(100 ms). At the final state only of a few isolated lubricant droplets remain. These droplets are connected by a uniform film with a thickness of $1.58\ nm$, which is approximately the smallest thickness at which $\Pi(h) = 0$ and $\Pi'(h) < 0$.

We now investigate the effect of substrate roughness on the de-wetting behavior of the lubricant. For this purpose we consider a substrate roughness with a maximum peak value of 0.1 nm. The roughness was generated randomly using a Gaussian noise distribution as shown in figure 5.12.

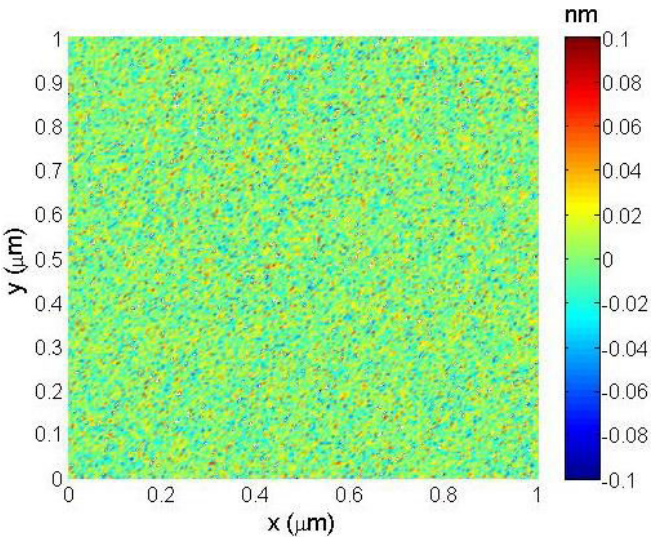

Fig. 5.12. Substrate roughness generated by Gaussian noise with maximum peak value of 0.1 nm.

On top of the substrate roughness we consider a lubricant film with a uniform thickness of 2.5 nm relative to the mean plane of the substrate roughness. We use the disjoining pressure given by (5.7). The results are shown in figure 5.13.

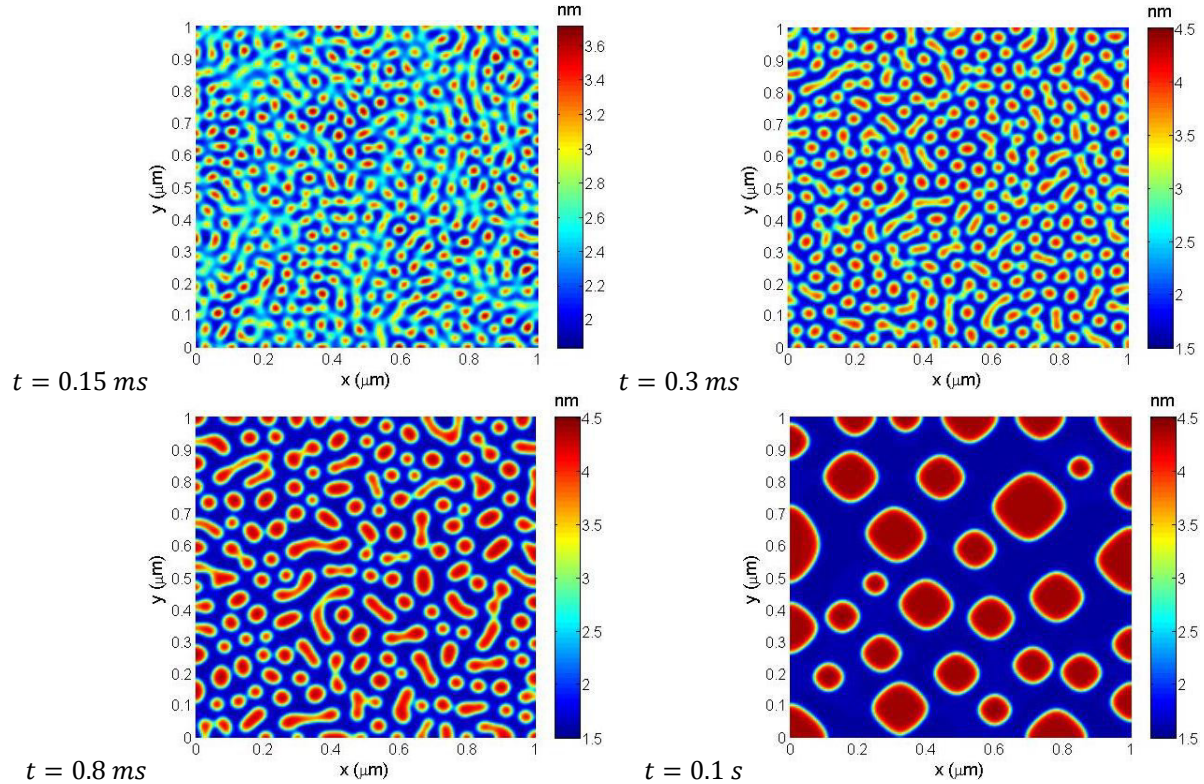

Fig. 5.13. Lubricant thickness profiles of a uniform film coating a substrate with roughness at times 0.15 ms, 0.3 ms, 0.8 ms, and 0.1 s. Disjoining pressure given by equation (5.7).

As observed in figure 5.13, the substrate roughness induces the uniform film to break up into droplets distributed throughout the computational domain. As time progresses, the smaller

droplets merge among each other to form larger ones. After a time of $t = 0.1\ s$ the state of the film consist of just a few isolated droplets with thickness of around 4.4 nm connected by a uniform 1.5 nm film. As observed above, the connecting film and droplet thickness correspond to the thickness h at which $\Pi(h) = 0$ and $\Pi'(h) < 0$.

5.4 Lubricant flow on a slider flying over a spinning disk

We now consider the case of a slider, no longer at rest, but flying over the spinning disk surface. In this case, we must consider the effects of air shear stress and air pressure. We consider a slider with length $L \approx 1\ mm$ so the equation of motion is given by (4.3). The dimensional version of that equation is reproduced here for convenience,

$$h_t + \nabla \cdot \left\{ \frac{h^2}{2\mu} \boldsymbol{\tau} - \frac{h^3}{3\mu} \nabla [p - \Pi(h)] \right\} = 0, \tag{5.8}$$

where the surface tension term is not included since it is negligible small compared to the other terms and can be left out of the governing equation as described in chapter 4 section 4.1. We non-dimensionalize equation (5.8) by replacing $h, t, x, y, \boldsymbol{\tau}, p, \Pi$ by the non-dimensional variables $h_0 h, t_s t, Lx, Ly, \tau_s \boldsymbol{\tau}, p_s p, \Pi_s \Pi$, where $\Pi_s = \Pi(h_0)$. We choose $\tau_s = 2h_0 \Pi_s/(3L)$, $p_s = \Pi_s, t_s = 3\mu L^2/(\Pi_s h_0^2)$. Thus, we obtain the non-dimensional equation,

$$h_t + \nabla \cdot \{h^2 \boldsymbol{\tau} - h^3 \nabla [p - \Pi(h)]\} = 0. \tag{5.9}$$

We consider the slider with the air bearing surface shown in figure 5.14. The length and width of this slider are 1.33 mm and 0.83 mm respectively.

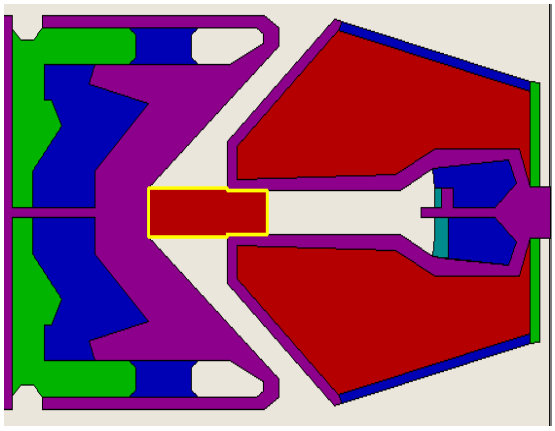

Fig. 5.14. Air bearing surface design chosen for the simulation of section 5.4. The length and width of this slider are $L = 1.33\ mm$ and $W = 0.83\ mm$ respectively.

We calculate the air shear stress and air bearing pressure using the CMLAir air bearing solver [75]. We solve equation (5.9) using the finite difference numerical scheme described before. We consider the disjoining pressure given by (5.7) and compare the results with those obtained by using the purely van der Waals disjoining pressure (4.4). The results are shown in figure 5.15 where the red color represents a thickness larger or equal to 2 nm.

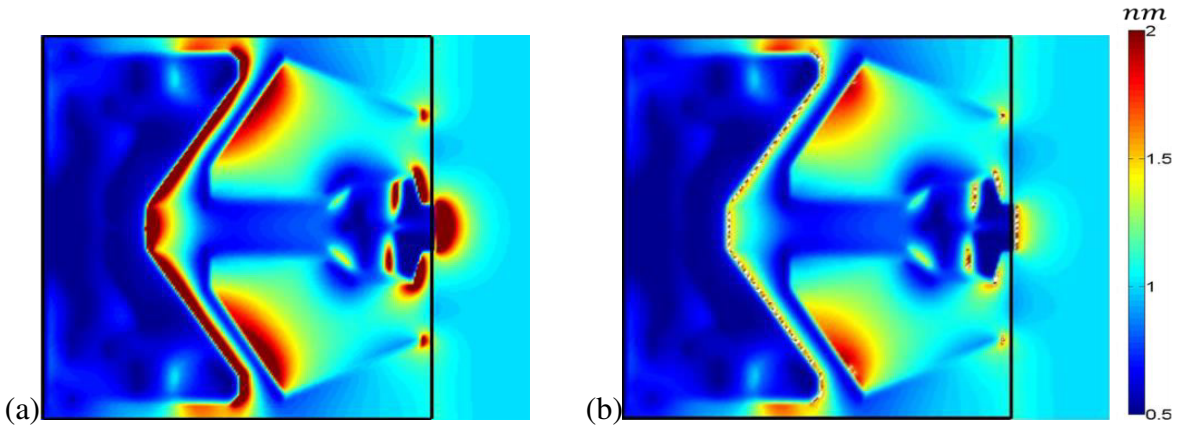

Fig. 5.15. Thickness profile at t = 100 s for a film with disjoining pressure given by equation (a) (4.4) and (b) (5.7)

It is observed, that the results obtained using a purely van der Waals disjoining pressure (figure 5.15a) are considerably different from those obtained with the disjoining pressure (5.7) (figure 5.15b). In figure 5.15b, we observe that, as the air shear stress forces the lubricant to migrate and accumulate on the surface of the slider, the film becomes unstable at those regions where its thickness is such that $\Pi'(h) > 0$. There, the film breaks up into droplets. As time progresses, the droplets increase in height and decrease in width. Eventually, the widths of the droplets narrow to the size of the computational grid ($5\ \mu m$) in a similar fashion to previous results shown in figure 5.4. Since there is no surface tension term to balance the disjoining pressure and air shear stress, the droplets continue to grow unboundedly. However, we expect that as the droplets decrease in width, the magnitude of their curvature will be sufficiently large for surface tension (Laplace pressure) to become important. This can only happen at a length scale of the order of $1\ \mu m$. Therefore, at such length scales, we need to consider the surface tension effect in our calculations.

We now consider only a portion of the slider surface of dimension $L = 1\ \mu m$. Then from equation (4.2) $C_p = 0.066, C_\sigma = 7.3(10^{-7})\,, C_\pi = 0.19$. In this case the surface tension term can be important when the curvature of the film is sufficiently large. However, the air shear stress and air pressure gradient vary on a scale of the order of $1\ \mu m$, hence they can be considered constant on such length scales, i.e. $\boldsymbol{\tau}$ and ∇p are constant in this case. The governing equation is given by (2.48), reproduced here for convenience,

$$h_t + \nabla \cdot \left\{ \frac{h^2}{2\mu} \boldsymbol{\tau} - \frac{h^3}{3\mu} \nabla [p - \sigma \Delta h - \Pi(h)] \right\} = 0. \tag{5.10}$$

We can obtain a non-dimensional equation free of constant coefficients by replacing $h, t, x, y, \boldsymbol{\tau}, p, \Pi$ by the non-dimensional variables $h_0 h, t_s t, Lx, Ly, \tau_s \boldsymbol{\tau}, p_s p, \Pi_s \Pi$. In this case we choose $\tau_s = 2\sigma h_0^2/(3L^3)\,, t_s = 3\mu L^4/(\sigma h_0^3)\,, p_s = \sigma h_0/L^2\,, \Pi_s = \sigma h_0/L^2$ to obtain the non-dimensional equation,

$$h_t + \nabla \cdot \{h^2 \boldsymbol{\tau} - h^3 \nabla [p - \Delta h - \Pi(h)]\} = 0. \tag{5.11}$$

Since, in this case $\boldsymbol{\tau}$ and ∇p are considered constants, equation (5.11) can be written as,

$$h_t + \nabla \cdot \{h^3 \nabla[\Delta h + \Pi(h)]\} + \boldsymbol{d} \cdot \nabla h = 0, \tag{5.12}$$

where $\boldsymbol{d}(h) = (2h\boldsymbol{\tau} - 3h^2 \boldsymbol{\nabla} p)$. We use the same slider as before, i.e. the one with ABS design shown in figure 5.14. The air shear stress and air bearing pressure are calculated with the CMLAir air bearing solver [75]. We consider the average values of $\boldsymbol{\tau}$ and ∇p over the region of the slider known as the central trailing edge pad. We obtain the non-dimensional values $\boldsymbol{\tau} = (2.1(10^5), 0)$ and $\nabla p = (286, 0)$. We solve equation (5.12) using a finite difference numerical scheme, where we use central differences for the surface tension and disjoining pressure terms, one sided differences for the time derivative. We also use one sided differences (upwind) for the last term in (5.12) since $\boldsymbol{d}$ acts effectively as a convective velocity.

We first consider, as initial condition, the lubricant droplet sitting on a uniform film shown in figure 5.6(0 s). The results are shown in figures 5.16a and 5.16b where we use the disjoining pressures given by (5.3) and (5.7) respectively.

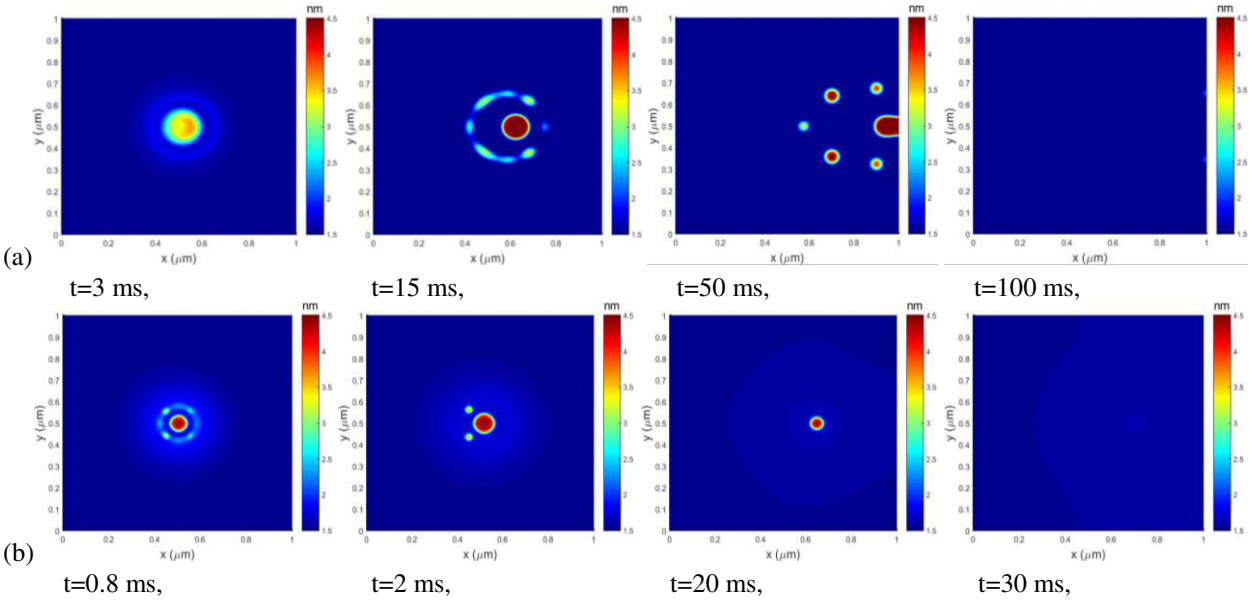

Fig. 5.16. Thickness profile of a lubricant droplet with disjoining pressure given by equation (a) (5.3) and (b) (5.7).

Now consider, as initial condition, a uniform lubricant film with a hole in the center as shown in figure 5.7(0 s). Here, we use only the disjoining pressures given by (5.7) and consider two values of air shear stress, $\boldsymbol{\tau} = (2.1(10^5), 0)$ and $\boldsymbol{\tau} = (2.1(10^6), 0)$, with $\nabla p = (286, 0)$ in both cases. The results are shown in figure 5.17.

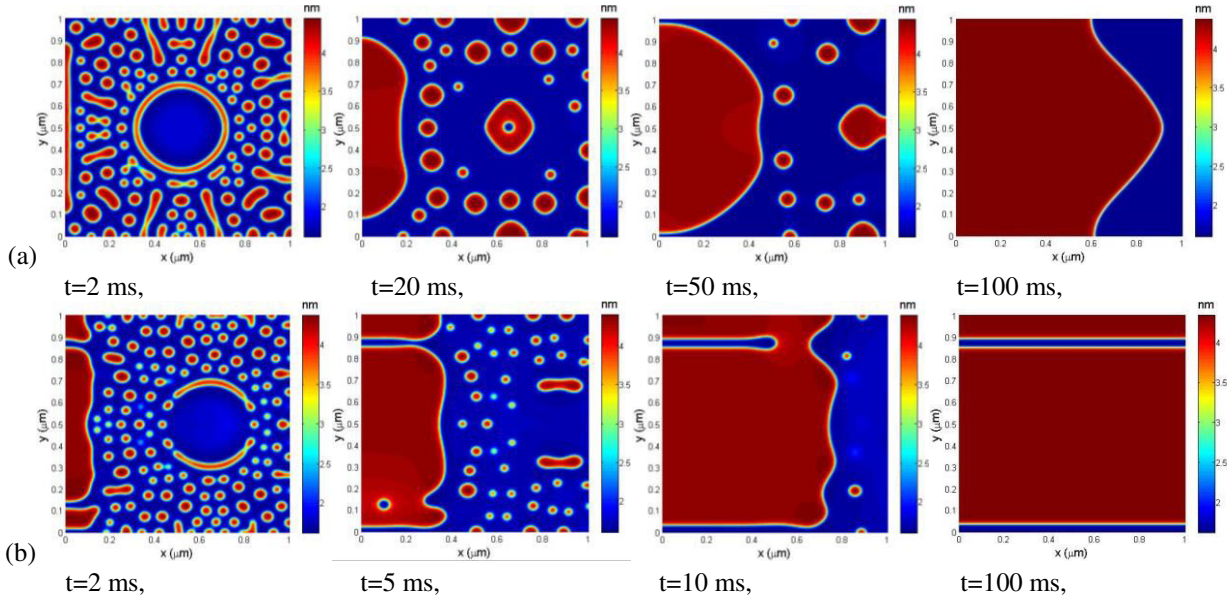

Fig. 5.17. Thickness profile of a hole in a lubricant film with disjoining pressure given by equation (5.7). The air shear stress is (a) $\boldsymbol{\tau} = (2.1(10^5),0)$ and (b) $\boldsymbol{\tau} = (2.1(10^6),0)$.

As we observe in figure 5.17, the maximum thickness of the lubricant film does not exceed the value of 4.35 nm which is approximately a thickness at which $\Pi(h) = 0$ and $\Pi'(h) < 0$. Therefore, the droplets shown before in figure 5.15b, which grow unboundedly, exceed this critical thickness and should not be considered realistic.

5.5 Conclusions

The de-wetting behavior of PFPE lubricant films on the slider's air bearing surface was investigated. We observed that, if the surface tension is neglected from the governing equations, the disjoining pressure acts as the only driving force during the spreading of a lubricant droplet. When the thickness of the droplet is larger than the critical de-wetting thickness, the disjoining pressure acts as a destabilizing force inducing the unrestrained growth of the film. The disjoining pressure induces the initial droplet to break up into smaller ones which narrow down in width and increase in height. We expect that as this process continues the curvature of each droplet will be of such significant magnitude that the surface tension cannot be neglected any more.

When we concentrate our attention to a portion of the slider with size $1\ \mu m \times 1\ \mu m$, the value of the surface tension is of significant magnitude so that it balances the effect of disjoining pressure. In this case, an initial lubricant droplet with thickness larger than the critical de-wetting thickness, breaks up into smaller droplets which then merge into large ones. The final state is that of a few stable droplets sitting on top of a uniform film.

When we include the effect of air shear stress and air pressure gradient into the governing equations the result is that of an initial droplet breaking up into smaller ones which are then sheared downstream in the direction of the air shear stress. In this case, when the computational domain is $1\ \mu m \times 1\ \mu m$, the air shear stress and air pressure gradient can be considered constants. It was not possible to simulate the de-wetting of the lubricant film on the whole slider domain, since it was found that surface tension is significant only at length scales much smaller than the size of the slider.

Chapter 6

Slider dynamics with lubricant on the air bearing surface

The total slider-disk distance in a hard disk drive needs to scale with the size of the recorded bit. In current HDDs the minimum clearance has been decreased to around 2 nm [6]. This clearance is so small that lubricant from the disk often transfers to the slider surface where it can potentially increase the magnetic spacing [98-101]. During HDD operations, the slider flies over the disk generating air shear stress that drives the lubricant on the ABS towards the trailing edge of the slider where it accumulates on the so-called deposit end as shown in figure 6.1a. When the HDD is at rest, some of the lubricant from the deposit end flows towards the ABS as shown in figure 6.1b. This migration is known as the "waterfall effect" [54]. When the slider is repositioned back on the disk, the lubricant on the ABS can result in an initial flying height larger than that of a clean slider, hence degrading the magnetic recording signal. Therefore, it is important to quantify the thickness and flow dynamics of these molecularly thin films on the slider surface considering, at the same time, possible changes in slider-disk spacing.

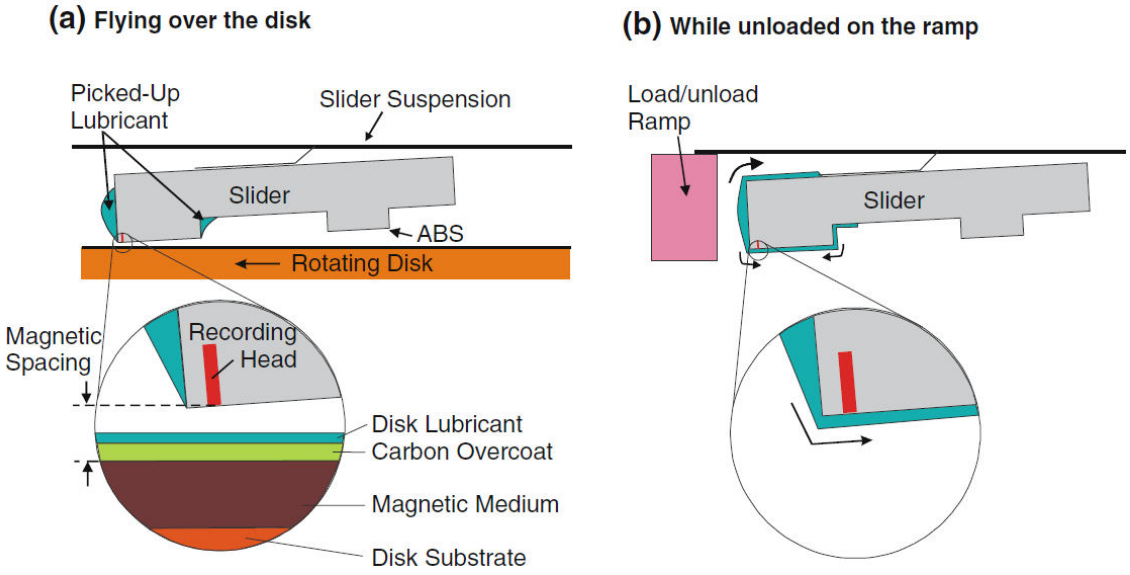

Fig. 6.1. (a) Slider flying over a spinning disk. (b) Illustration of the ''waterfall effect.'' [55].

The contribution to magnetic spacing of the molecularly thin film of lubricant that can form on the slider's air bearing surface (ABS) were often neglected when spacings were much greater than 10 nm, it but has become the focus of numerous recent investigations [99, 100, 101, 54, 55], as now even a sub-nanometer increase in magnetic spacing can degrade the recording performance of the hard drive. In current HDDs, the lubricant thickness on the disk amounts to about 10% of the total HMS [82]. In [55] the authors performed experimental tests to calculate the change in magnetic spacing due to lubricant migration on the slider and the results were compared with numerical simulations. However, for the numerical simulations they assumed the air shear stress to be fixed in time. In this chapter, we study the migration of lubricant on the slider surface considering time dependent air shear stress and air pressure gradient. We calculate the increase in spacing due to the migration of lubricant on the ABS.

6.1 The slider dynamics model

As the lubricant migrates on the ABS, the head-media spacing is expected to change. Lubricant accumulated on the air bearing surface may potentially modify the slider's attitude resulting in a change of air shear stress, the main driving force of the lubricant flow. Therefore, to improve the accuracy of our predictions we need to account for changes in flying attitude as the lubricant migrates on the slider surface. This situation is depicted schematically in figure 6.2.

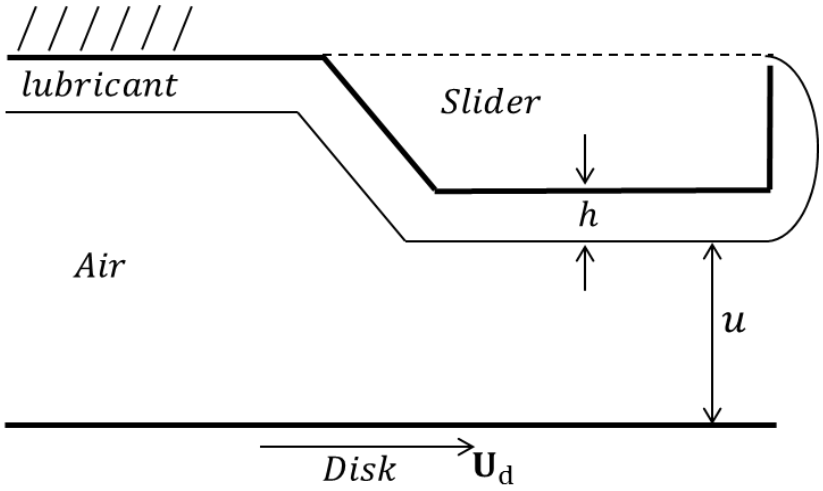

Fig. 6.2. Head-disk interface with a lubricant film on the slider surface.

To improve our predictions, the equations of motion for lubricant, air pressure and slider dynamics must be solved simultaneously. The equations governing the lubricant thickness on the slider and air pressure are given by (5.8) and (2.38) respectively. They are reproduced here for convenience,

$$h_t + \nabla \cdot \left\{ \frac{h^2}{2\mu}\boldsymbol{\tau} - \frac{h^3}{3\mu}\nabla[p - \Pi(h)] \right\} = 0, \tag{6.1}$$

$$(pu)_t - \nabla \cdot \left[\frac{u^2}{12\eta}(6D + pu)\nabla p \right] + \frac{1}{2}\mathbf{U}_d \cdot \nabla(pu) = 0, \tag{6.2}$$

where $h, \mu, \Pi(h), \eta, u, p, \mathbf{U}_d = (U_x, U_y)$ are the lubricant thickness, lubricant viscosity, disjoining pressure, air viscosity, slider-disk spacing, air pressure and disk linear velocity, respectively. Here $D = p_0\lambda(p_0)$, where λ is the mean free path of air evaluated at the ambient pressure p_0. The symbols ∇, Δ represent the two dimensional gradient and Laplace operators respectively. We notice that in equation (6.1) we have not included surface tension effects since, as shown in chapter 5, they are negligible small on the length scales of the slider length i.e. $L = 1\ mm$ and $h = 1\ nm$. The air shear stress $\boldsymbol{\tau} = (T_{xz}, T_{yz})$ in (6.1) is given by equations (2.39) calculated at the slider's ABS, i.e. at $z = h$ and $\boldsymbol{n} = -\boldsymbol{e}_z$. Hence,

$$\boldsymbol{\tau} = -\frac{u}{2}\nabla p + \frac{\eta p}{(2D + pu)}\mathbf{U}_d, \tag{6.3}$$

The slider is attached to a flexible suspension known as the Head Gimbal Assembly (HGA) as seen in figure 6.3. The suspension induces a vertical load and torsional moments (pitch and roll moments) on the slider that balance the forces exerted by the air on the slider i.e. the normal pressure and shear stress on the slider's ABS.

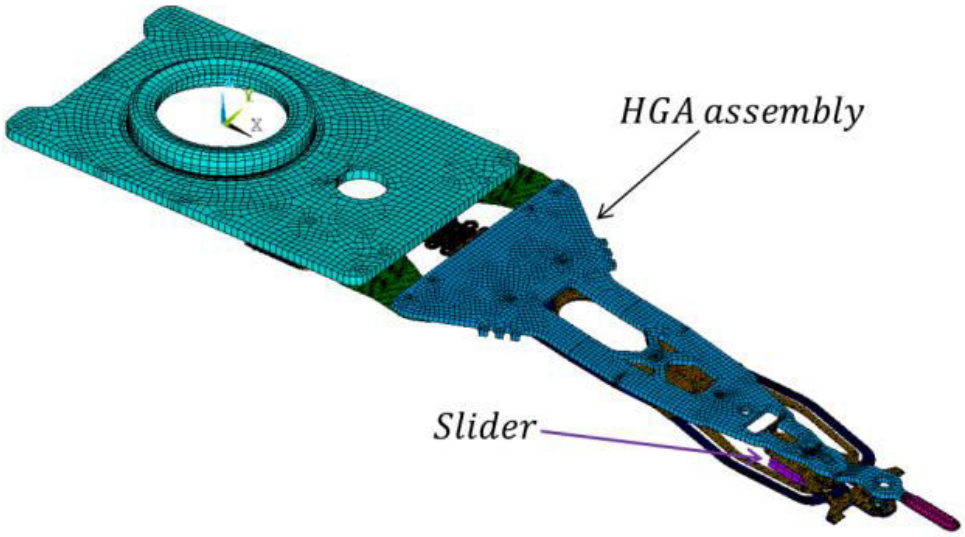

Fig. 6.3. Finite element mesh of the Head Gimbal Assembly.

The dynamics of the slider and HGA can be modeled using a finite element analysis. An accurate modeling of the HGA can require a large number of degrees of freedom (DOF), e.g. 204,000 DOF in the typical case shown in figure 6.3. Since our main interest is the air bearing and lubricant dynamics, considering such large number of DOF becomes computationally demanding. Therefore, in our approach we approximate the slider-HGA system by a rigid body consisting only of 3-DOF, i.e. translation in the vertical z direction and rotations about the x and y axes. In this reduced model we account for the stiffness and damping of each of the 3 DOF. The model is shown in figure 6.4.

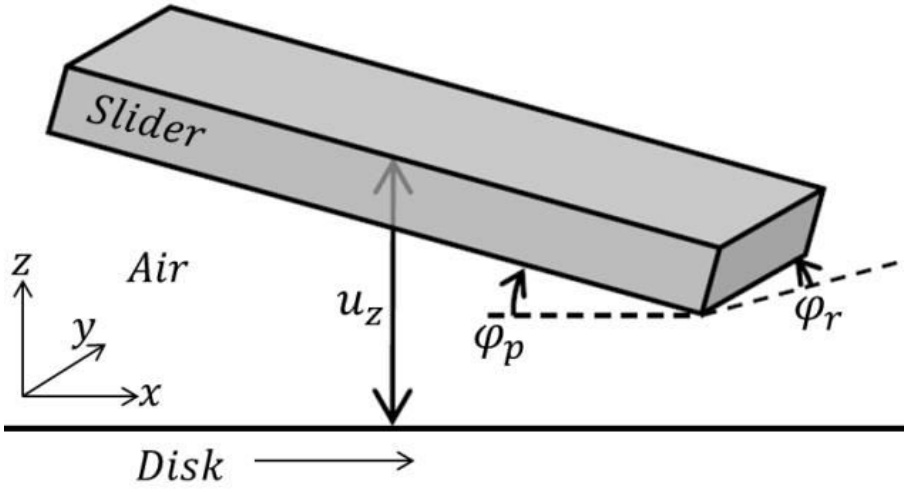

Fig. 6.4. Model of the slider body with three degrees of freedom.

We consider the motion along the z axis and rotations about the x and y axes to be independent (decoupled) of each other. The equation governing the dynamics of the system shown in figure 6.4 is obtained from a balance of applied and inertial forces on the slider body. Thus we obtain,

$$M\ddot{\boldsymbol{u}} + C\dot{\boldsymbol{u}} + K\boldsymbol{u} = \boldsymbol{F}(\boldsymbol{u}), \tag{6.4}$$

with,

$$\boldsymbol{u} = \begin{bmatrix} u_z \\ \varphi_p \\ \varphi_r \end{bmatrix}, M = \begin{bmatrix} m_z & 0 & 0 \\ 0 & m_p & 0 \\ 0 & 0 & m_r \end{bmatrix}, C = \begin{bmatrix} c_z & 0 & 0 \\ 0 & c_p & 0 \\ 0 & 0 & c_r \end{bmatrix}, K = \begin{bmatrix} k_z & 0 & 0 \\ 0 & k_p & 0 \\ 0 & 0 & k_r \end{bmatrix}, \boldsymbol{F} = \begin{bmatrix} F_z \\ T_p \\ T_r \end{bmatrix}, \tag{6.5}$$

where $u_z, \varphi_p, \varphi_r, m_z, m_p, m_r, c_z, c_p, c_r, k_z, k_p, k_r, F_z, T_p, T_r$ are the slider-disk spacing measured at the ABS center, pitch angle, roll angle, slider mass, pitch moment of inertia, roll moment of inertia, vertical damping coefficient, pitch damping coefficient, roll damping coefficient, vertical stiffness, pitch stiffness, roll stiffness, vertical force, pitch torque and roll torque respectively. Here, $\boldsymbol{F}(\boldsymbol{u})$ is the external applied force which depends on the slider's attitude $\boldsymbol{u}$. The applied force $\boldsymbol{F}(\boldsymbol{u})$ is calculated by integrating the air pressure and air shear stress over the slider's ABS in the form,

$$F_z = \int_{-W/2}^{W/2}\int_{-L/2}^{L/2}(p - p_0)dxdy - g_z, \tag{6.6a}$$

$$T_p = \int_{-W/2}^{W/2}\int_{-L/2}^{L/2}[bT_{xz} + x(p - p_0)]dxdy - g_p, \tag{6.6b}$$

$$T_r = \int_{-W/2}^{W/2}\int_{-L/2}^{L/2}\big[bT_{yz} + y(p - p_0)\big]dxdy - g_r, \tag{6.6c}$$

where $W, L, b,$ are the slider's y-width, x-length, z-thickness respectively. Also, p_0 is the ambient pressure, and g_z, g_p, g_r are dead (constant) loads applied to the slider by the suspension. All forces and torques are calculated at the center of the slider. Notice that the air pressure and air shear stress depend on the local slider-disk spacing u (hence on $\boldsymbol{u}$) as evidenced by equations (6.2) and (6.3).

It is convenient to obtain time scales for changes in lubricant thickness and changes in air bearing pressure in order to have a better understanding of both processes. For this reason we non-dimensionalize equations (6.1), (6.2) and (6.3) by replacing the dimensional variables $h, x, y, \boldsymbol{\tau}, p, \Pi, u$ by the non-dimensional ones $h_0 h, Lx, Ly, \tau_s \boldsymbol{\tau}, p_s p, \Pi_s \Pi, h_0 u$. Also, in (6.1) and (6.2) we replace time t by the non-dimensional time $t_h t$ and $t_p t$ respectively. Clearing dimensions in all equations leads to the choice $p_s = 6\eta U_x L/h_0^2$, $\tau_s = \eta U_x/h_0$, $\Pi_s = p_s$ with time scales for air pressure and lubricant thickness given by $t_p = 2L/U_x$ and $t_h = (\mu/\eta)t_p$. The non-dimensional governing equations become,

$$h_t + \nabla \cdot \{h^2\boldsymbol{\tau} - 4h^3\nabla[p - \Pi(h)]\} = 0, \tag{6.7}$$

$$(pu)_t - \nabla \cdot \left[\left(\widehat{D} + pu\right)u^2\nabla p\right] + U_x^{-1}\mathbf{U}_d \cdot \nabla(pu) = 0, \tag{6.8}$$

$$\boldsymbol{\tau} = -3u\nabla p + \frac{3pU_x^{-1}}{\left(\widehat{D} + 3pu\right)}\mathbf{U}_d, \tag{6.9}$$

where $\widehat{D} = 6D/(h_0 p_s)$. A typical value of viscosity for lubricants used in HDDs is $\mu = 1\ Pa \cdot s$ and that for air is $\eta = 1.806(10^{-5})\ Pa \cdot s$. Therefore, we find that the time scale for changes in lubricant thickness is approximately $t_h = 5.5(10^4)t_p$, i.e. $5.5(10^4)$ times larger than the time it takes for changes in air pressure to occur.

We need also to non-dimensionalize equations (6.6) by replacing $x, y, p, T_{xz}, T_{yz}, F_z, T_p, T_r$ by the non-dimensional variables $Lx, Ly, p_s p, \tau_s T_{xz}, \tau_s T_{yz}, F_z^s F_z, T_p^s T_p, T_r^s T_r$ with the choice $F_z^s = p_s L^2, T_p^s = p_s L^3, T_r^s = T_p^s$. Obtain the non-dimensional equations,

$$F_z = \int_{-\alpha/2}^{\alpha/2}\int_{-1/2}^{1/2}(p - \hat{p}_0)dxdy - \hat{g}_z, \tag{6.10a}$$

$$T_p = \int_{-\alpha/2}^{\alpha/2}\int_{-1/2}^{1/2}\left[\hat{b}T_{xz} + x(p - \hat{p}_0)\right]dxdy - \hat{g}_p, \tag{6.10b}$$

$$T_r = \int_{-\alpha/2}^{\alpha/2}\int_{-1/2}^{1/2}\left[\hat{b}T_{yz} + y(p - \hat{p}_0)\right]dxdy - \hat{g}_r, \tag{6.10c}$$

where $\alpha = W/L$, $\hat{b} = bh_0/(6L^2)$, $\hat{p}_0 = p_0/p_s$, $\hat{g}_z = g_z/(p_s L^2)$, $\hat{g}_p = g_p/(p_s L^3)$, $\hat{g}_r = g_r/(p_s L^3)$. Similarly we can replace $t, u_z, \varphi_p, \varphi_r, F_z, T_p, T_r$ in equation (6.5) by the non-dimensional variables $t_p t, h_0 u_z, \varphi_p^s \varphi_p, \varphi_r^s \varphi_r, F_z^s F_z, T_p^s T_p, T_r^s T_r$ where φ_p^s, φ_r^s are referential pitch and roll angles respectively. Obtain the non-dimensional equation,

$$\widehat{M}\ddot{\boldsymbol{u}} + \hat{C}\dot{\boldsymbol{u}} + \widehat{K}\boldsymbol{u} = \boldsymbol{F}, \tag{6.11}$$

with,

$$\boldsymbol{u} = \begin{bmatrix} u_z \\ \varphi_p \\ \varphi_r \end{bmatrix}, \widehat{M} = \begin{bmatrix} \widehat{m}_z & 0 & 0 \\ 0 & \widehat{m}_p & 0 \\ 0 & 0 & \widehat{m}_r \end{bmatrix}, \hat{C} = \begin{bmatrix} \hat{c}_z & 0 & 0 \\ 0 & \hat{c}_p & 0 \\ 0 & 0 & \hat{c}_r \end{bmatrix}, \widehat{K} = \begin{bmatrix} \hat{k}_z & 0 & 0 \\ 0 & \hat{k}_p & 0 \\ 0 & 0 & \hat{k}_r \end{bmatrix}, \boldsymbol{F} = \begin{bmatrix} F_z \\ T_p \\ T_r \end{bmatrix}, \tag{6.12}$$

where $\widehat{m}_z = m_z h_0/\left(F_z^s t_p^2\right)$, $\hat{c}_z = c_z h_0/\left(F_z^s t_p\right)$, $\hat{k}_z = k_z h_0/F_z^s$, $\widehat{m}_p = m_p \varphi_p^s/\left(T_p^s t_p^2\right)$, $\hat{c}_p = c_p \varphi_p^s/\left(T_p^s t_p\right)$, $\hat{k}_p = k_p \varphi_p^s/T_p^s$, $\widehat{m}_r = m_r \varphi_r^s/\left(T_r^s t_p^2\right)$, $\hat{c}_r = c_r \varphi_r^s/\left(T_r^s t_p\right)$, $\hat{k}_r = k_r \varphi_r^s/T_r^s$.

We use an implicit finite difference numerical scheme to solve equations (6.7), (6.8) and the Newmark-Beta method [82, 102, 103] for equation (6.11). We can proceed to solve equations (6.7-6.12), in a straightforward way, by using a single time step for the three equations. Then, at each time step t, we solve equations (6.8) and (6.11) simultaneously to obtain the air pressure p and slider attitude $\boldsymbol{u}$ at time $t + \Delta t$. From equation (6.9), we calculate the air shear stress $\boldsymbol{\tau}$ at the slider's surface which is then used, along with the air pressure p, as input for the lubricant thickness equation (6.7). The lubricant thickness h is used to calculate the slider-disk spacing u which is measured from the surface of the disk to the surface of the lubricant as shown in figure 6.2. We repeat the process for subsequent time steps until we have reached a desired final time. This solution scheme is represented by the flow chart shown in figure 6.5.

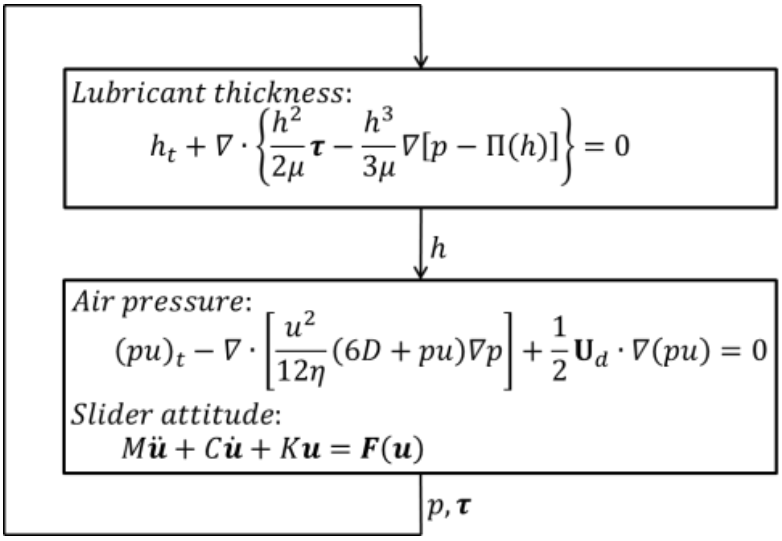

Fig. 6.5. Chart flow of the solution process for the lubricant thickness, air pressure and slider dynamics equations.

The above solution procedure is computationally demanding and time consuming. However, we can take advantage of the disparity in time scales that exist between the lubricant flow and air bearing processes, i.e. $t_h \approx 5.5(10^4)t_p$. We therefore assume that the slider attitude and air pressure remain in a steady state until sufficient time has passed for the lubricant film on the slider to undergo a significant change. Hence, we first find the steady state solution of equations (6.8) and (6.11), i.e.

$$\nabla \cdot \left[\left(\widehat{D} + pu \right) u^2 \nabla p \right] - U_x^{-1} \mathbf{U}_d \cdot \nabla(pu) = 0, \tag{6.13}$$

$$\widehat{K}\boldsymbol{u} = \boldsymbol{F}. \tag{6.14}$$

Thus, we obtain the air pressure p and flying height u which are used to calculate the air shear stress $\boldsymbol{\tau}$ at the slider surface using equation (6.9). Then, we solve equation (6.7) to obtain the lubricant thickness h using a time step $5.5(10^4)$ times larger than $t_p = 2L/U_x$. We repeat this process for subsequent time steps until we have reached a desired final time.

To solve the steady state equations (6.13) and (6.14), we need to find the equilibrium flying attitude $\boldsymbol{u} = \left(u_z, \varphi_p, \varphi_r \right)$ such that $\boldsymbol{R}(\boldsymbol{u}) \equiv \boldsymbol{F} - \widehat{K}\boldsymbol{u} = \boldsymbol{0}$. We solve iteratively for $\boldsymbol{u}$ using

Newton's method [104, 105]. We start with an initial guess $\boldsymbol{u}_{n-1}$ which we use to solve (6.13) and calculate $\boldsymbol{F}$ from (6.10). Then, we obtain a better approximation $\boldsymbol{u}_n$ in the form,

$$\boldsymbol{u}_n = \boldsymbol{u}_{n-1} - J^{-1}(\boldsymbol{u}_{n-1})\boldsymbol{R}(\boldsymbol{u}_{n-1}), \tag{6.15}$$

where $J = \nabla_{\boldsymbol{u}}\boldsymbol{R}$ is the Jacobian matrix of $\boldsymbol{R}$ evaluated at $\boldsymbol{u}_{n-1}$. We compute the elements of J numerically using the finite difference approximation,

$$J_{ij} \approx \frac{R_i(u_j + \Delta u_j) - R_i(u_j)}{\Delta u_j}. \tag{6.16}$$

We iterate Newton's method (6.15) until $\|\boldsymbol{R}\| < \delta$, where δ is a desired tolerance [106].

As discussed in Chapter 4, the governing equation for the air bearing pressure (6.13) was derived assuming a first order slip condition for the velocity at the air-solid interface. Before proceeding further, we wish to compare this approach with the molecular gas lubrication (MGL) equation implemented in the CMLAir solver [75]. The solution of the first order slip governing equation (6.13), yields a minim flying height of 12.66 nm, maximum air pressure 24.0 atm, and maximum air shear stress 0.2217 atm. On the other hand, the results using CMLAir solver with the MGL equation yield a minimum flying height of 12.28 nm, maximum air pressure 22.5 atm, and maximum air shear stress 0.2230 atm. The difference in air shear stress between CMLAir and our approach is only of 0.5 %. Since, as shown in chapter 4, the main driving force for the lubricant flow is the air shear stress, we considered the first order slip condition to be adequate for our purposes.

6.2 Simulation results

Consider first the case of a slider with a uniform layer of lubricant on its air bearing surface. The initial thickness of the lubricant film is 1 nm. We use the slider design shown in figure 5.12. The disk angular velocity is set to 10,000 rpm. The radial position and skew angle of the slider are 23 mm and 0° respectively, which correspond to the linear velocity $\mathbf{U}_d = (24.08, 0)\ m/s$. The minimum steady state flying height, $\min u$, of this particular slider design without any lubricant on its surface is 12.66 nm. We use a disjoining pressure given by purely van der Waals forces i.e. $\Pi(h) = Ah^{-3}$ with $A = 5.3(10^{-21})\ Nm$. The lubricant viscosity was set to $\mu = 1\ Pa \cdot s$. The results are presented in figures 6.5 and 6.6 below.

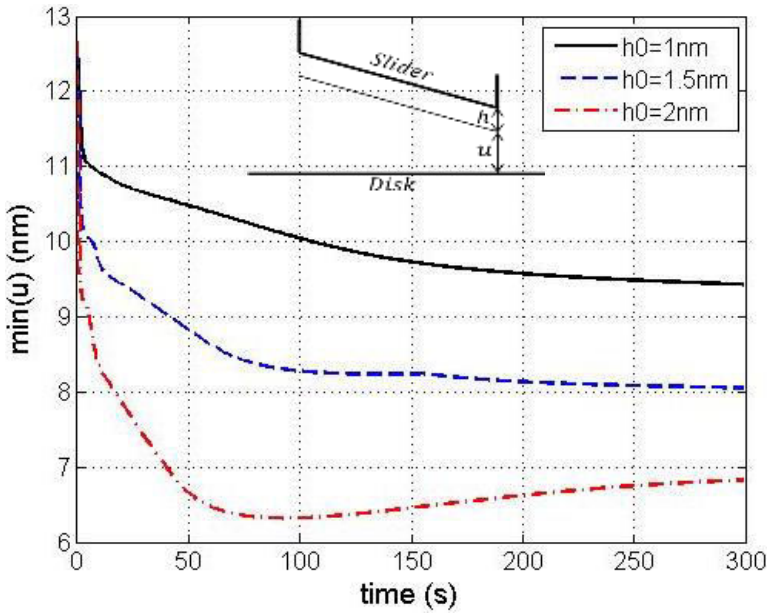

Fig. 6.5. Minimum flying height, $\min u$, as a function of time.

Figure 6.5 shows the minimum air clearance, $\min u$, measured from the surface of the disk to the surface of the lubricant on the slider. We note that the minimum air spacing, $\min u$, is always located around the center of the slider's trailing edge (center trailing pad). We observe that as the air shear stress pushes the lubricant towards the slider's trailing edge, the minimum air spacing decreases. We also observe in figure 6.5 that the distance from the disk to lubricant surface, $\min u$, decreases as the initial film thickness h_0 increases. The rate of decrease in $\min u$ is relatively large within the first five seconds, but it slows down as time progresses. The decrease in $\min u$ is faster for larger initial film thickness h_0.

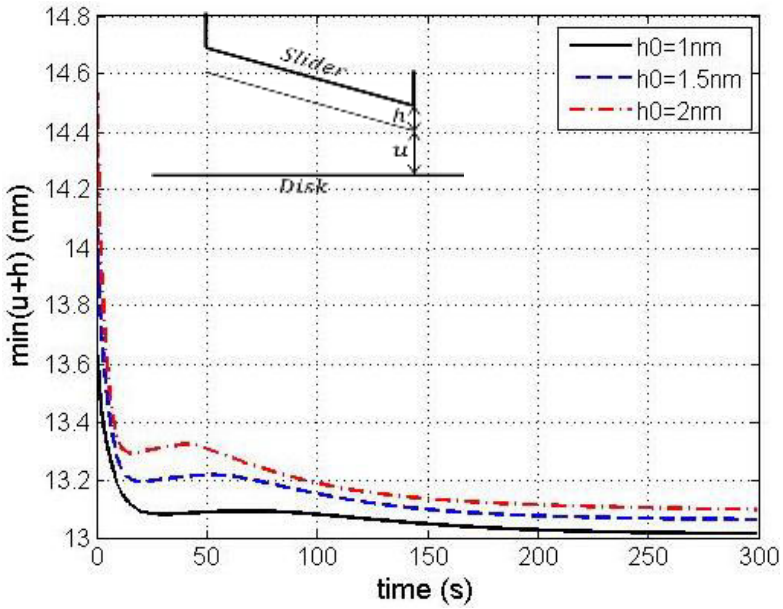

Fig. 6.6. Minimum head-disk spacing, $\min(h+u)$, as a function of time.

Figure 6.6 shows the minimum head-disk spacing, $\min(u+h)$, measured from the surface of the disk to the solid surface of the slider. During read/write operations of the hard disk drive it is important to maintain the magnetic head, i.e. the read/write elements, as close as possible to the disk surface in order to achieve higher recording densities and better magnetic signals [54]. Therefore, the distance $\min(u+h)$ is of special interest for the optimal performance of the HDD. We observe that $\min(u+h)$ increases with the initial film thickness h_0. Also, after 100 s the minimum head-disk spacing is over 13 nm for $h_0 \geq 1\, nm$, which is larger than that of a clean slider, i.e. 12.66 nm. As pointed out above, this increase in spacing can be detrimental to the quality of the magnetic signal. We note that the locations where the spacings $\min u$ and $\min(u+h)$ occur are not necessarily the same. Also both locations may change with time as the slider's attitude and lubricant thickness evolve.

Now we fix the slider at its steady state flying attitude. We consider the air shear stress and air bearing pressure to be constant in time. We use the same disk angular velocity and lubricant properties as above. Under these conditions we calculate the minimum spacing, $\min u$, and compare the results with those obtained above for a slider free to change its flying height with time. The results are presented in figure 6.7.

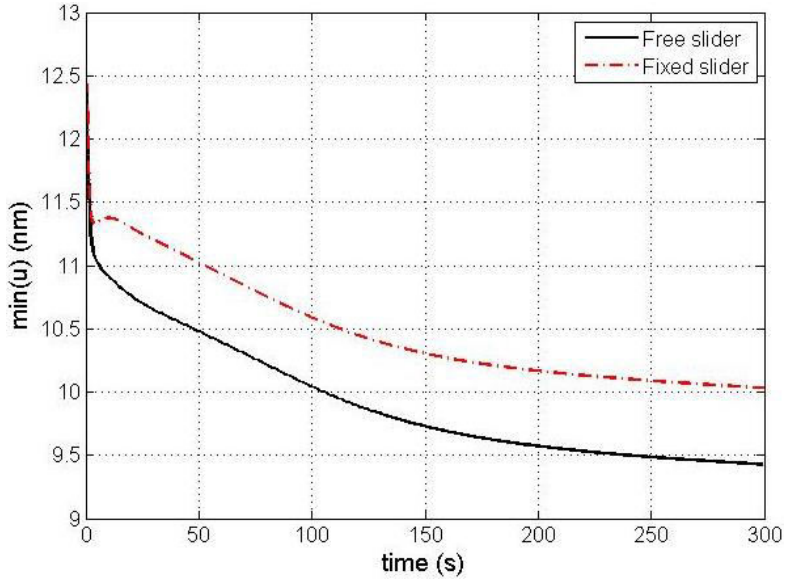

Fig. 6.7. Minimum flying height, $\min u$, as a function of time for a free and fixed slider with initial lubricant thickness $h_0 = 1\, nm$.

As observed in figure 6.7 the minimum flying height, $\min u$, for the fixed slider is larger than that of the free slider. We also note that on the fixed slider, $\min u$ decreases with time which implies that lubricant accumulates on a location near the slider's central trailing pad. For this purpose, we calculate the lubricant thickness as a function of time on three points of the center trailing pad. The coordinates of points 1, 2, 3 are $x = 0.9904L, 0.9952L, L$ respectively and $y = 0.5W$ for all points. Here L, W are the slide's length and width respectively. The results are shown in figure 6.8.

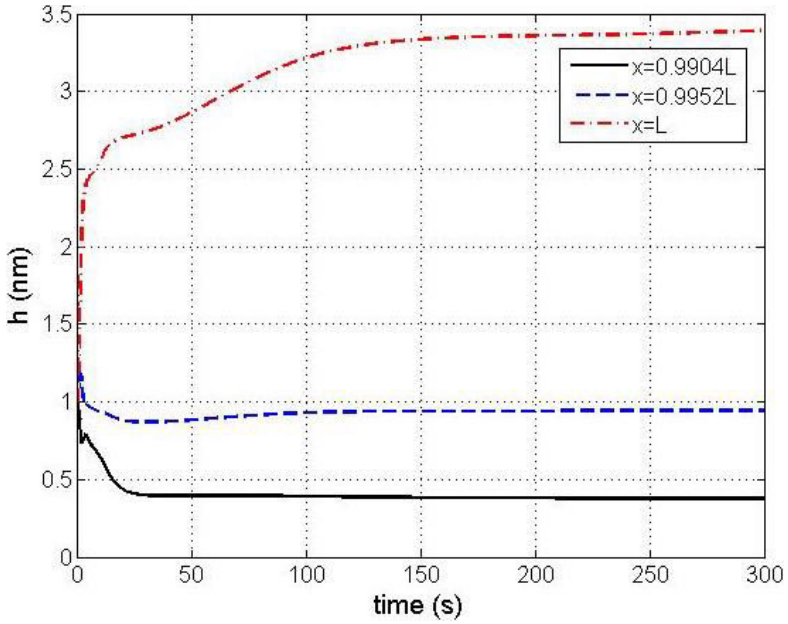

Fig. 6.8. Lubricant thickness, h, as a function of time at three locations on the slider's central trailing pad with coordinates $x = 0.9904L, 0.9952L, L$ respectively. Here $y = 0.5W$ for all points.

As observed in figure 6.8, the lubricant thickness increases with time on the edge of the slider's trailing pad at $x = L$ but it decreases on the interior points $x = 0.9904L$ and $x = 0.9952L$. Therefore, we expect the spacing, u, to decrease with time at the edge of the slider's central pad i.e. at $(x, y) = (L, 0.5W)$. On the other hand, u increases with time in the interior points of the slide's central pad.

6.3 Conclusions

In this chapter we have calculated the slider's change of attitude due to the migration of lubricant on its air bearing surface. The air shear stress and air bearing pressure were considered dependent of time; they were updated at each time step during the numerical simulations. We observed that the time scale for changes in lubricant thickness is approximately 10^4 times larger than that for changes in air pressure. Due to this disparity in time scales, we concluded that it is computationally expensive to consider a single time step for the numerical simulation of both processes. Therefore, we used a time step for the lubricant flow simulations 10^4 times larger than that of typical air bearing pressure simulation, e.g. $10^{-2}\ s$ for the lubricant and $10^{-6}\ s$ for the air. At each time step we calculated the steady state slider's attitude and air bearing pressure which was used as input for the lubricant thickness simulations.

We observed that the minimum air spacing, measured from the surface of the disk to the surface of the lubricant on the slider, decreases with time and with initial film thickness h_0. The decrease in air spacing is relatively fast in the first five seconds but slows down as time progresses. It was also observed that the minimum head-disk spacing, measured from the surface of the disk to the solid surface of the slider, decreases with time and increases with initial film thickness h_0. After 100 s, the minimum head-disk spacing is significantly larger than that of a slider with no lubricant on its surface. This increase in spacing is detrimental for the read/write performance of the hard drive.

Chapter 7

Numerical simulations of two dimensional lubricant flow on the disk surface

As the slider-disk spacing approaches sub-nanometer clearances in current HDDs, it is expected that the lubricant from the disk will be displaced due to increasing air shear stresses and van der Waals interactions from the slider [107, 110]. It is observed experimentally that continuous flying of a slider on a disk track induces the formation of lubricant features on the disk which in turn give rise to undesirable oscillations of the slider. Some of these features are called lubricant moguls [107]. These are located on the track in a random fashion which does not correspond to any of the slider's air bearing frequencies as shown in figure 7.1. There are other undulations on the lubricant which correlate with the air bearing frequencies; these are known as ripples [111]. It has been proposed that both moguls and ripples originate from air shear effects [35].

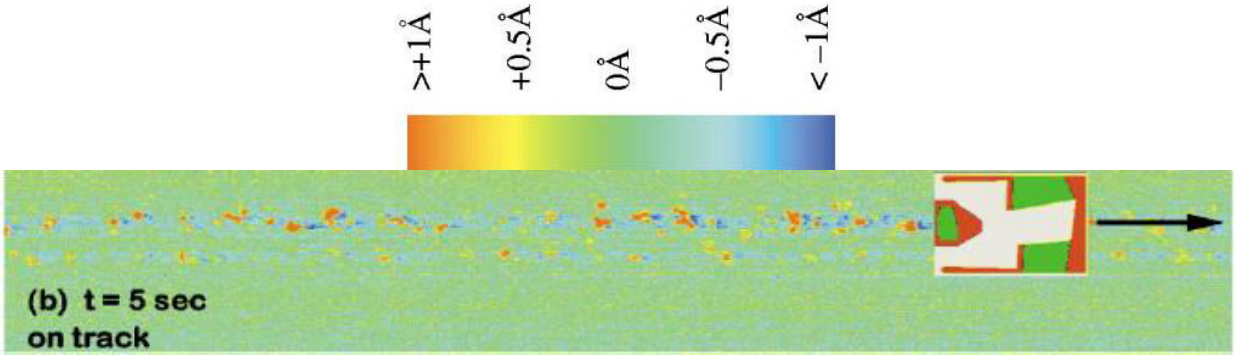

Fig. 7.1. Lubricant displacement on a disk track showing the moguls generated by a slider flying continuously over the same track for 5 s [107].

The moguls are not a result of lubricant dewetting since their formation occurs at film a thickness lower than the critical thickness. It has been proposed that the location of the lubricant moguls correlates to the location of irregularities in the substrate topography as shown in figure 7.2.

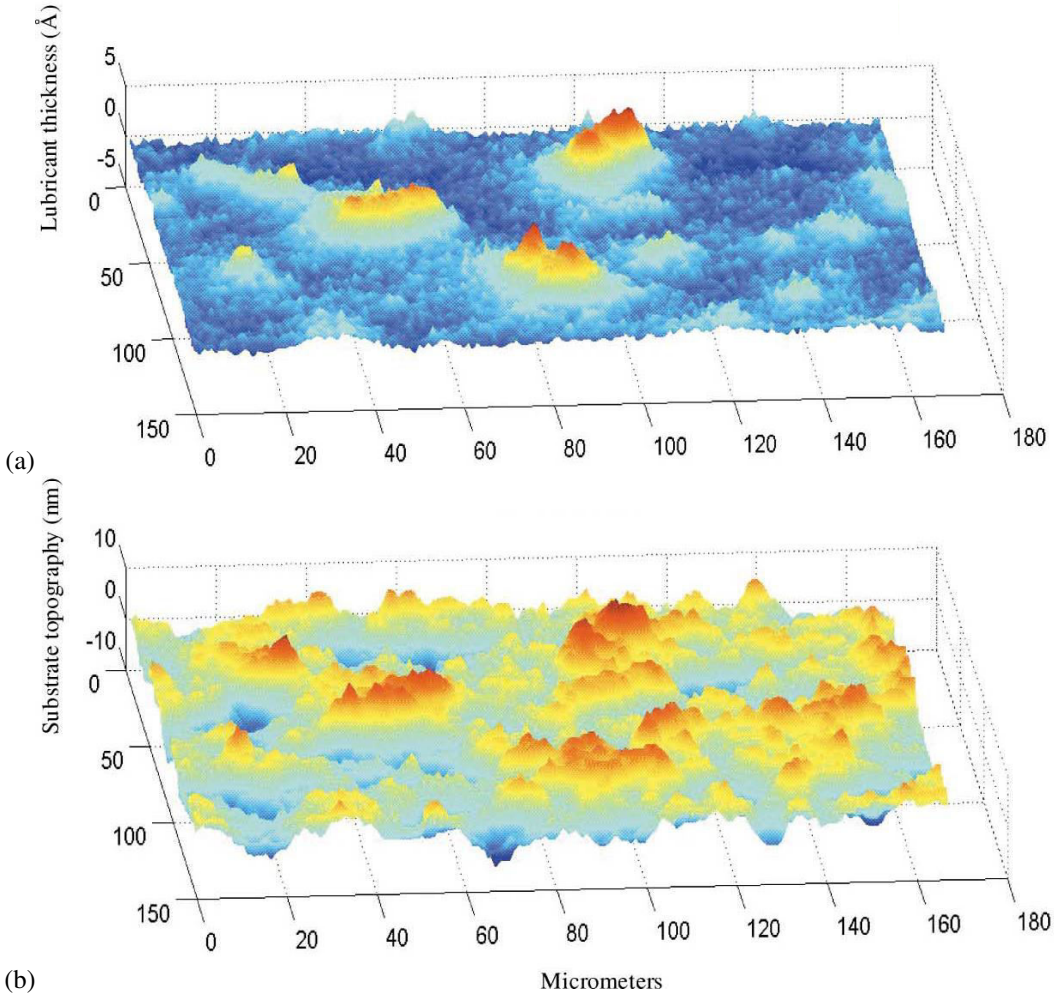

Fig. 7.2. (a) Lubricant thickness and (b) disk substrate topography [107].

In this chapter we investigate the effect of air shear stress and air pressure gradient on the formation of disk lubricant moguls. Predicting the formation of moguls on the disk surface can be of critical importance when the head-disk clearance is of the order of a few nanometers.

7.1 Governing equations

We want to study the lubricant flow on the surface of the disk when a slider is flying over a given track as depicted in figure 7.3.

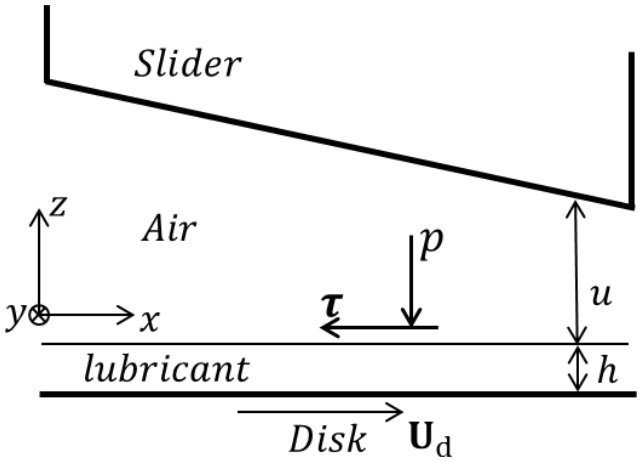

Fig. 7.3. Slider flying over a spinning disk coated with a lubricant film.

The equation governing the evolution of the film thickness on the disk is given by (2.48). Since in this chapter we are concerned with length scales of the order of $L = 1\ mm$ and $h = 1\ nm$, we can ignore surface tension effects as pointed out in chapter 4. Therefore, the equation of motion of the lubricant (2.48) becomes,

$$h_t + \nabla \cdot \left\{ \frac{h^2}{2\mu} \boldsymbol{\tau} - \frac{h^3}{3\mu} \nabla [p - \Pi(h)] \right\} + \mathbf{U}_d \cdot \nabla h = 0. \tag{7.1}$$

The air shear stress $\boldsymbol{\tau} = \left(T_{xz}, T_{yz}\right)$ in (7.1) is given by equations (2.39) calculated at the free surface of the lubricant, i.e. at $z = 0$ and $\boldsymbol{n} = \boldsymbol{e}_z$. Hence, the air shear stress is obtained from,

$$\boldsymbol{\tau} = -\frac{u}{2} \nabla p - \frac{\eta p}{(2D + pu)} \mathbf{U}_d. \tag{7.2}$$

We take into account possible van der Waals attractions exerted by the slider on the disk lubricant. This effect is included in our calculations by means of a disjoining pressure of the form,

$$\Pi(h) = Ah^{-3} + B(v - h)^{-3}, \tag{7.3}$$

where $v = u + h$. Here, A and B are Hamaker constants for the interactions between the lubricant film and the disk surface, and between the lubricant film and the slider through vacuum respectively [18, 112, 113]. Typically, the carbon overcoats on the slider and on the disk surface have different constitutive properties so that $A \neq B$. We note that the second term in equation (7.3) represents a pressure exerted on the lubricant by the slider. Consequently, the slider must experience an equal and opposite pressure that needs to be taken into account in the calculation of $\boldsymbol{F}(\boldsymbol{u})$, i.e. we replace p by $p - B(v - h)^{-3}$ in equations (6.6).

The equation of motion for the lubricant thickness must be solved simultaneously with those for air pressure and slider dynamics. The solution procedure is represented schematically in figure 7.4.

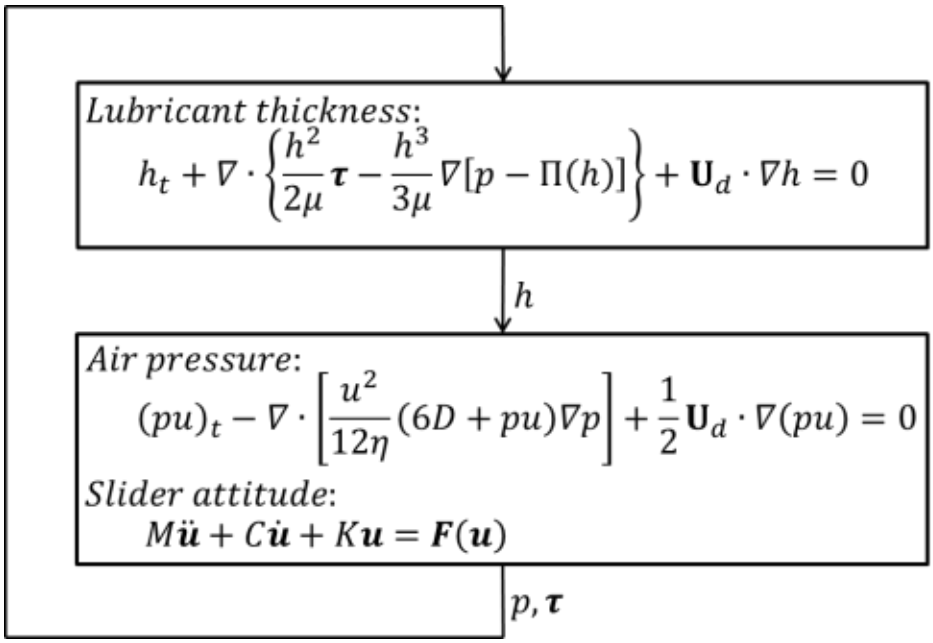

Fig. 7.4. Chart flow of the solution process for the lubricant thickness, air pressure and slider dynamics equations.

The non-dimensional version of the equations shown in figure 7.4 can be obtained using the same dimensional scaling used in chapter 7. The resulting non-dimensional equations for air pressure and slider attitude are given by (6.8) and (6.11), while the non-dimensional equation for lubricant thickness is given by,

$$h_t + \nabla \cdot \{h^2\boldsymbol{\tau} - 4h^3\nabla[p - \Pi(h)]\} + 2(\mu/\eta)U_x^{-1}\mathbf{U}_d \cdot \nabla h = 0. \qquad (7.4)$$

Equation (7.4) differs from (6.7) by the convective term $2(\mu/\eta)U_x^{-1}\mathbf{U}_d \cdot \nabla h$ which arises in this case due to the motion of the disk with velocity $\mathbf{U}_d$.

7.2 Simulation results of lubricant flow on a disk track

Since the length of a typical track on the disk is several orders of magnitude longer than the length of the slider (e.g. a disk track at a radius of 23 mm is 144 mm long while the slider is only 1 mm in length), we restrict the computational domain to only the section on the disk underneath the slider. This section has the length and width of the ABS as shown in figure 7.5. On this section, we set periodic boundary conditions on the leading and trailing edges and set $\partial h/\partial n = 0$ on the inner and outer edges. The condition $\partial h/\partial n = 0$ implies a zero volume flux boundary condition. We note that considering a disk track with the length of the slider is not a significant limitation to the model since the time response for changes in lubricant thickness is several orders of magnitude larger than the time for the disk to complete one revolution.

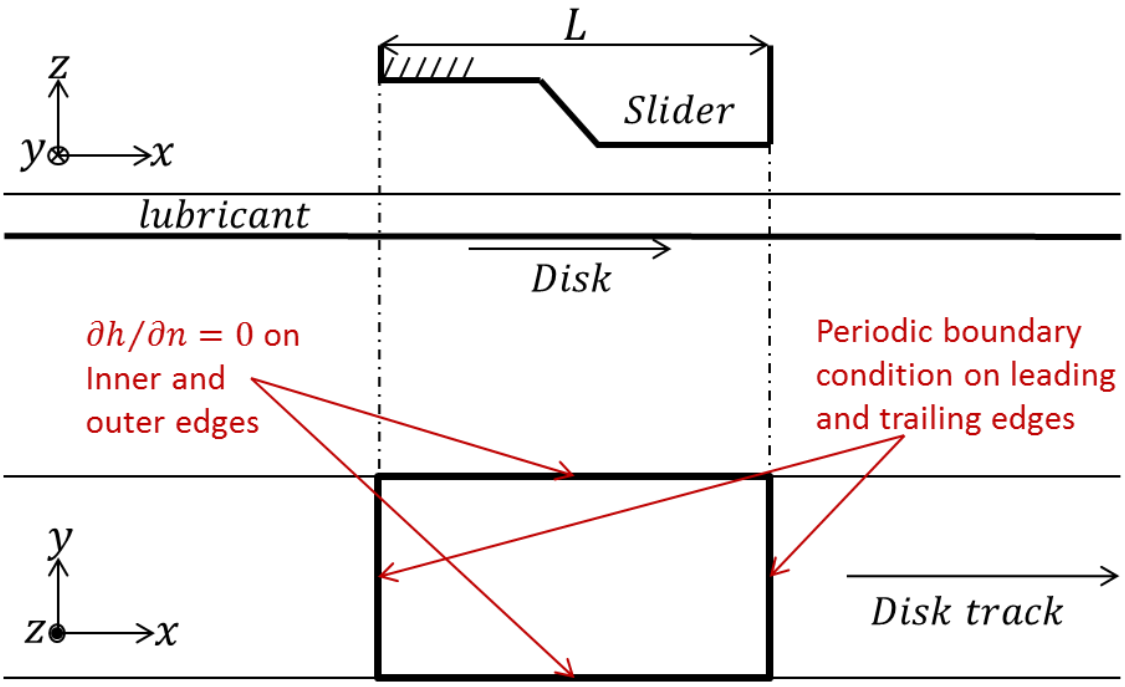

Fig. 7.5. Computational domain on the disk track with boundary conditions.

We consider the case of a smooth disk track coated with a uniform lubricant film. We first assume that a slider is flying on top of the track with a fixed steady state flying attitude so that the air pressure gradient and air shear stress are constant in time. We use the slider's ABS design presented in figure 5.12. The steady state air pressure $\hat{p}$, air pressure gradient $\nabla\hat{p} = (\hat{p}_{,x}, \hat{p}_{,y})$ and shear stress $\hat{\boldsymbol{\tau}} = (\hat{T}_{xz}, \hat{T}_{yz})$ are plotted in figures 7.6, 7.7 and 7.8 respectively. Here, the symbol $\widehat{\ }$ denotes steady state variables. For the slider design shown in figure 5.12 the steady state flying attitude corresponds to a minimum flying height = 12.25 nm, pitch = 135.77 µrad, and roll = 15.96 µrad.

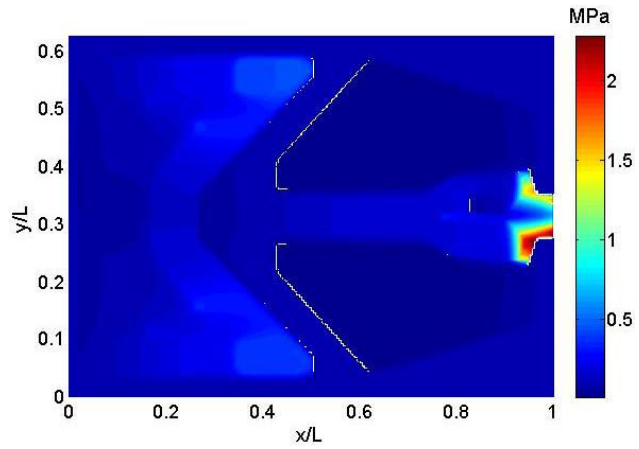

Fig. 7.6. Steady state air pressure profile $\hat{p}$ for the ABS design shown in figure 5.12.

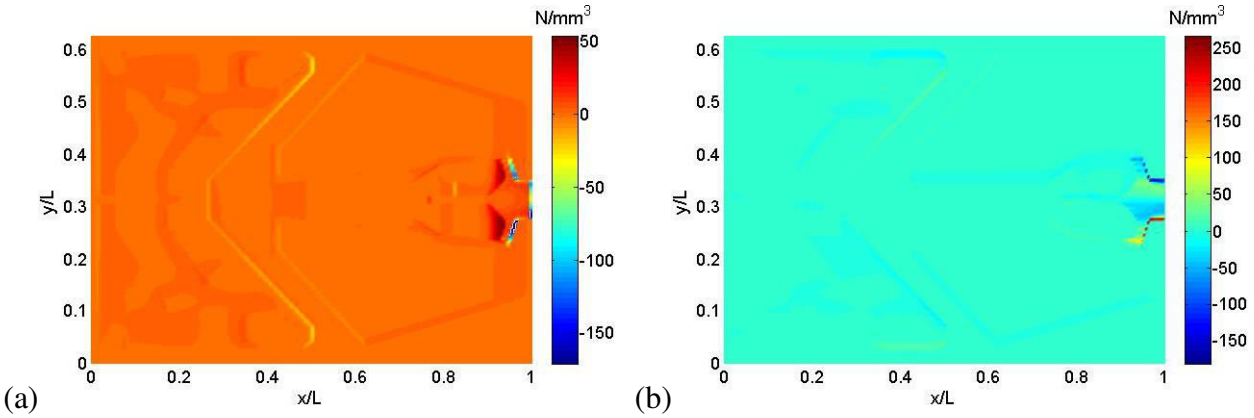

Fig. 7.7. Components of the steady state air pressure gradient: (a) $\hat{p}_{,x}$ and (b) $\hat{p}_{,y}$.

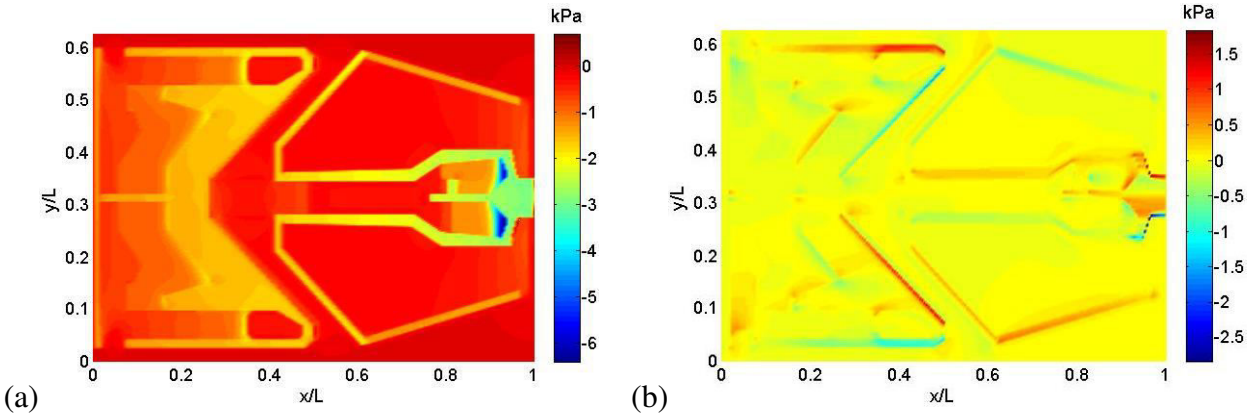

Fig. 7.8. Components of the steady state air shear stress: (a) $\hat{T}_{xz}$ and (b) $\hat{T}_{yz}$.

As initial condition the disk is covered with a uniform 1 nm lubricant film. We solve equation (7.1) for h using the numerical method described in previous chapters. The disk angular velocity is set to 10,000 rpm. The radial position and skew angle of the slider are 23 mm and 0° respectively, which correspond to the linear velocity $\mathbf{U}_d = (24.08, 0)\ m/s$. We use the disjoining pressure given by (7.3) with $A = 5.3(10^{-22})\ Nm$ and $B = 5.3(10^{-20})\ Nm$ and a lubricant viscosity of $\mu = 1\ Pa \cdot s$ [113]. The results at time $t = 1\ min$ are shown in figure 7.9.

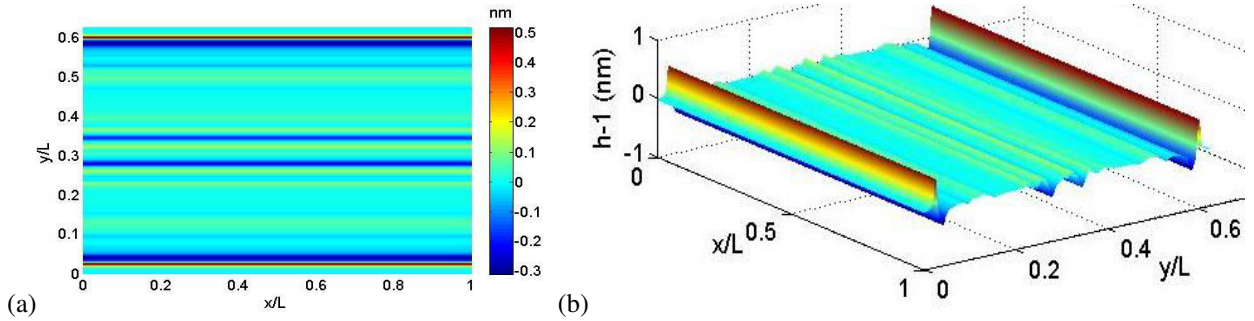

Fig. 7.9. Lubricant displacement profile, $h - 1$, induced by a slider flying at steady state for $t = 60\ s$; (a) 2D view and (b) 3D view.

Figure 7.9 shows the lubricant tracks on the disk surface left by the flying slider. The lubricant film had a maximum deformation of 0.5 nm after 60 s of slider flying on the same track which is

equivalent to 1.086 million revolutions on the "reduced" track, i.e. the track with the same size as the slider.

When a slider flies over an asperity or a disturbance in the topography of the disk, the slider will vibrate in either of the vertical, downtrack or offtrack directions or a combination of the three. The vibration of the slider results in changes in the air bearing pressure and hence in the shear stress. To obtain further insight into the process of lubricant flow on the disk surface, we solve equation (7.1) considering that the air shear stress and air pressure gradient have the following artificially imposed sinusoidal variation in time:

$$\boldsymbol{\tau}(x,y,t) = \{1 + max[\sin(2\pi t/\hat{t}),0]\}\hat{\boldsymbol{\tau}}(x,y), \tag{7.5a}$$

$$\nabla p(x,y,t) = \{1 + max[\sin(2\pi t/\hat{t}),0]\}\nabla\hat{p}(x,y), \tag{7.5b}$$

where $\hat{t} = L/U_x$. Here, $\hat{\boldsymbol{\tau}}$ and $\nabla\hat{p}$ are the steady state air pressure gradient and air shear stress shown in figure 7.7 and 7.8 respectively. This sinusoidal variation is intended to roughly approximate changes in flying height of the slider. In this case, we consider a section of a disk track with dimensions $W \times 2L$, where W is the slider's width and L is the slider's length. Then, we solve equation (7.1) numerically to obtain the results shown in figures 7.10 and 7.11.

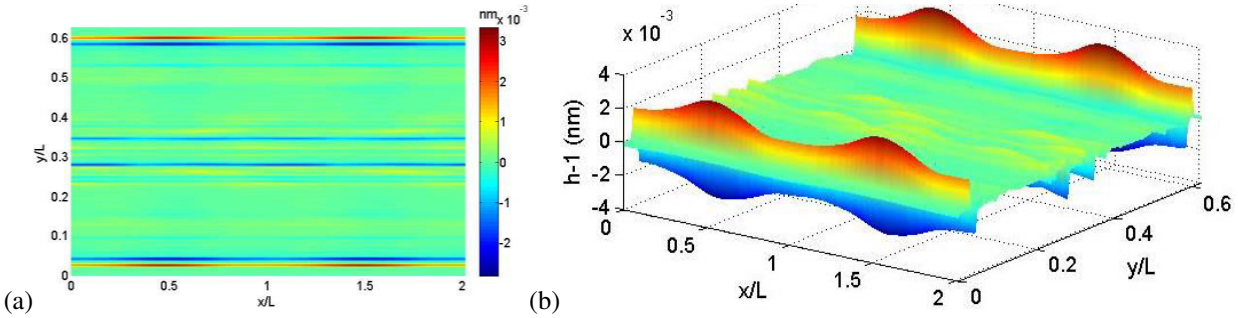

(a) (b)

Fig. 7.10. Lubricant displacement profile, $h - 1$, induced by the air shear stress and air pressure gradient (7.5) at time $t = 0.265\ s$ on a disk track with dimensions $W \times 2L$; (a) 2D view and (b) 3D view.

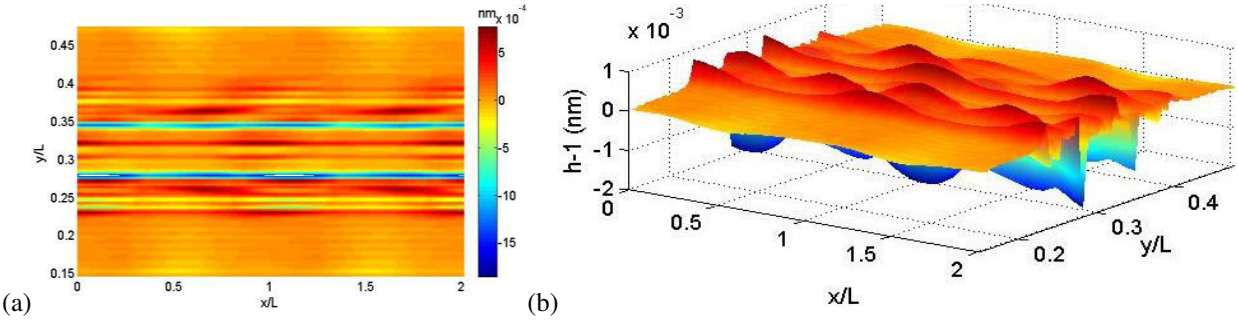

(a) (b)

Fig. 7.11. Lubricant displacement profile, $h - 1$, on a central section of the track shown in figure 7.10 of width from $y = 0.15L$ to $y = 0.46L$ and same length; (a) 2D view and (b) 3D view.

As observed in figure 7.10, the oscillations in air shear stress and pressure gradient induce periodic fluctuations on the lubricant with the same frequency as that in (7.5). After a simulation time of $t = 0.265\ s$, we observed a maximum deformation of the lubricant of $3.3(10^{-3})nm$ which is located under the side rails of the slider's ABS. Figure 7.11 shows the section of the

track ($0.31L$ in width) located underneath the slider's center pad. The maximum lubricant deformation in this section is $1.9(10^{-3})nm$.

We now investigate the effect of downtrack oscillations of the slider i.e. along the x-axis. For this purpose we assume that the location of the air shear stress $\boldsymbol{\tau}$, and air pressure gradient ∇p, moves along the track in a sinusoidal manner, i.e.

$$\boldsymbol{\tau}(x, y, t) = \hat{\boldsymbol{\tau}}(x - \hat{x}\sin(2\pi t/\hat{t}), y), \tag{7.6a}$$

$$\nabla p(x, y, t) = \nabla \hat{p}(x - \hat{x}\sin(2\pi t/\hat{t}), y), \tag{7.6b}$$

where $\hat{x} = 0.25L$. This sinusoidal variation is intended to roughly approximate the motion of the slider along the downtrack direction. Then, we solve equation (7.1) numerically to obtain the results shown in figure 7.12 and 7.13.

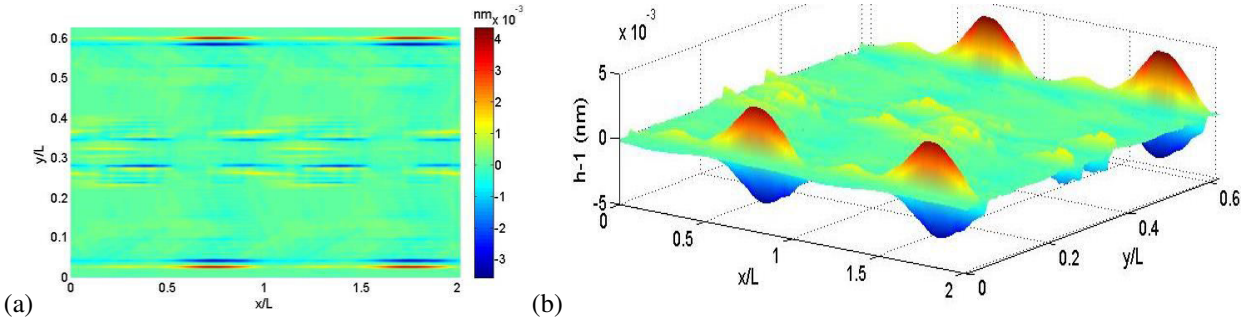

(a) (b)

Fig. 7.12. Lubricant displacement profile, $h - 1$, induced by the air shear stress and air pressure gradient (7.6) at time $t = 0.265\ s$ on a disk track with dimensions $W \times 2L$; (a) 2D view and (b) 3D view.

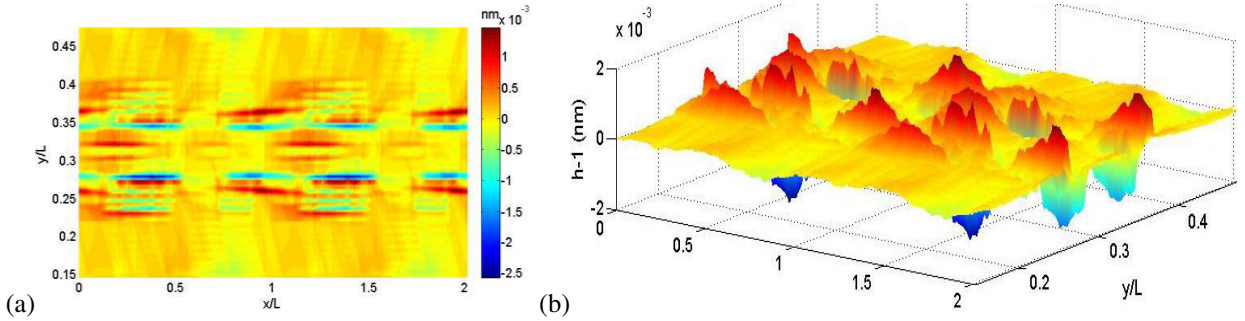

(a) (b)

Fig. 7.13. Lubricant displacement profile, $h - 1$, on a central section of the track shown in figure 7.12 of width from $y = 0.15L$ to $y = 0.46L$ and same length; (a) 2D view and (b) 3D view.

As observed in figure 7.12, the downtrack motion of the air shear stress and pressure gradient induce periodic fluctuations on the lubricant with the same frequency given in (7.6). After a simulation time of $t = 0.265\ s$, we observed a maximum deformation of $4.3(10^{-3})nm$ of the lubricant which is located under the side rails of the slider's ABS. Figure 7.13 shows the section of the track ($0.31L$ in width) located underneath the slider's center pad, i.e. under the slider's read/write elements. The maximum lubricant deformation in this section is $2.6(10^{-3})nm$.

7.3 Conclusions

In this chapter we have numerically solved the lubricant evolution equation on the disk surface. It was found that the lubricant film on a disk track has a maximum deformation of 5 Å when a slider flies continuously over the same track for a total time of 1 minute. A sinusoidal variation in the magnitude of the air shear stress and air pressure gradient induces modulations in the lubricant thickness of the same wave length as that of the shear stress. It was also observed that a downtrack oscillation of the air shear stress and air pressure gradient induce modulation of the lubricant film thickness with similar characteristics as those modulations arising from magnitude oscillations of the shear stress. The oscillations in air shear stress and air pressure gradient are intended to approximate the changes in flying height that a slider undergoes when flying over an asperity or a disturbance in the topography of the disk.

Chapter 8

Conclusions and Future work

8.1 Conclusions

We have implemented a numerical method to obtain the lubricant evolution on both the slider's air bearing surface and the disk surface. The numerical scheme solves a partial differential equation that governs the motion of thin film fluids. This governing equation, known as Reynolds equation, was deduced from classical lubrication theory which is based on continuum mechanics. Even though the air and lubricant films on the head-disk interface are composed of just a few molecules across their thickness, the continuum approach followed here was proven to be adequate.

We studied the recovery behavior of a depleted Z-tetraol film after laser heating. More lubricant depletion was observed when the exposure time to the laser heating was increased. We observed that almost 80% of the lubricant reflows back to the depleted region within 20 min at room temperature. Our simulation results showed a good agreement with experiments. The discrepancy between experiments and simulations was attributed to differences in the model chosen for the disjoining pressure. Also, the lubricant viscosity of real thin films is thickness dependent while in our simulations it was assumed to be constant. Other factors such as viscoelasticity of the lubricant may also give rise to differences in the simulations results.

It was shown that the lubricant accumulation characteristics on the slider surface are strongly dependent on the slider's flying height, skew angle and ABS design. It is concluded that a smaller flying height contributes to a faster lubricant removal from the ABS due to an induced increase in air shear stress. It is observed that when the HDD is at rest, lubricant accumulated on the deposit end flows back into the ABS driven by the action of disjoining pressure. It was found, for a particular slider design, that increasing the slider's skew angle has the effect of enhancing the lubricant flow process due to a decrease in the slider's flying height. The lubricant migration process is significantly dependent on the ABS design. It is found that slider designs that accumulate most lubricant on a broader area on the deposit end and have larger values of air shear stress remove lubricant from the ABS at higher volume rates than those designs where accumulation is concentrated near the center of the deposit end and have smaller values of average shear stress.

We investigated the de-wetting behavior of PFPE lubricant films on the slider's air bearing surface. It was observed that, if the surface tension is neglected from the governing equations, the disjoining pressure acts as the only driving force during the spreading of a lubricant droplet. When the thickness of the droplet is larger than the critical de-wetting thickness, the disjoining pressure is a destabilizing force that induces the unrestrained growth of the droplet. The disjoining pressure breaks up the initial droplet into smaller ones which narrow down in width and increase in height. When we consider a portion of the slider with size $1\,\mu m \times 1\,\mu m$, the value of the surface tension is large enough to balance the effect of disjoining pressure. In this case, an initial lubricant droplet breaks up into smaller droplets which then merge to form larger ones. The final state is that of a few stable droplets sitting on top of a uniform film. When we include the effect of air shear stress and air pressure gradient into the governing equations the

result is that of an initial droplet breaking up into smaller ones which are then sheared downstream in the direction of the air shear stress. It was not possible to simulate the de-wetting of the lubricant film on the whole slider domain, since it was found that surface tension is significant only at length scales much smaller than the size of the slider and without surface tension the solution is unstable.

We calculated the slider's change of attitude due to the migration of lubricant on its air bearing surface. The air shear stress and air bearing pressure were considered dependent of time; they were updated at each time step during the numerical simulations. We observed that the time scale for changes in lubricant thickness is approximately 10^4 times larger than that for changes in air pressure. Due to this disparity in time scales, we concluded that it is computationally expensive to consider a single time step for the numerical simulation of both processes. Therefore, we used a time step of $10^{-2}\ s$ for the lubricant flow simulation and a time step of $10^{-6}\ s$ for the air bearing pressure simulation. At each time step we calculated the steady state slider's attitude and air bearing pressure which was used as input for the lubricant thickness simulations. We observed that the minimum air spacing, measured from the surface of the disk to the surface of the lubricant on the slider, decreases with time and with initial film thickness h_0. The decrease in air spacing is relatively fast in the first five seconds but slows down as time progresses. It was also observed that the minimum head-disk spacing, measured from the surface of the disk to the solid surface of the slider, decreases with time and increases with initial film thickness h_0. After 100 s, the minimum head-disk spacing is significantly larger than that of a slider with no lubricant on its surface. This increase in spacing is detrimental for the read/write performance of the hard drive.

We simulated the lubricant evolution equation on the disk surface. It was found that the lubricant film on a disk track has a maximum deformation of 5 Å when a slider flies continuously over the same track for a total time of 1 minute. A sinusoidal variation in the magnitude of the air shear stress and air pressure gradient induces modulations in the lubricant thickness of the same wave length as that of the shear stress. It was also observed that a downtrack oscillation of the air shear stress and air pressure gradient induce modulation of the lubricant film thickness similar to the lubricant moguls observed experimentally by in many laboratories. The oscillations in air shear stress and air pressure gradient are an approximation to the changes in flying height that a slider undergoes when flying over an asperity or a disturbance in the topography of the disk.

8.2 Future work

To obtain more accurate descriptions of the lubricant flow process it is possible to make several improvements into the governing equations. For instance, in this work the lubricant viscosity was considered to be constant. However, it has been observed by several authors [37, 114] that the lubricant viscosity of thin PFPE films can be thickness dependent. Some of the models discussed in the literature can be implemented in the governing equations. Other factors such as viscoelasticity effects on the lubricant can also be taken into account to improve the accuracy of the mathematical models.

The disjoining pressure models used throughout this dissertation were only rough approximations to real PFPE lubricants on amorphous carbon overcoats. It is desirable to carry out experimental tests to obtain a model of disjoining pressure that can match, as close as

possible, the true behavior of the lubricant-substrate systems found in commercially available hard disk drives. Moreover, the new temperature conditions expected in future heat assisted magnetic recording drives are likely to change the properties of the disjoining pressure and the lubricant viscosity. In this case, it is necessary to consider temperature dependent properties for the lubricant film.

The initial condition for the lubricant film on the slider's ABS was always considered to be a uniform layer which covered the whole surface of the slider. However, it is observed in experiments that the lubricant on the slider is non-uniformly distributed on its surface [41]. It is then convenient to develop a novel model of lubricant transfer that can predict the lubricant distribution on the ABS, for a slider flying at close proximity or possibly in contact with the disk. Current models found in the literature are limited to one dimension [50, 39] or are so computationally demanding that can only consider small regions of the slider of the order of a few nanometers [115, 116].

Bibliography

[1] Arpaci-Dusseau, R. H., Arpaci-Dusseau, A. C. (2012). Operating systems: Three easy pieces.
[2] http://www.pcguide.com/ref/hdd/op/index.htm
[3] https://en.wikipedia.org/wiki/Hard_disk_drive
[4] Chen, B. M., Lee, T. H., Peng, K., Venkataramanan, V. (2006). Hard disk drive servo systems. Springer Science & Business Media.
[5] Daniel, E. D., Mee, C. D., Clark, M. H. (1999). Magnetic recording: the first 100 years. John Wiley & Sons.
[6] Marchon, B., Olson, T. (2009). Magnetic spacing trends: from LMR to PMR and beyond. Magnetics, IEEE Transactions on, 45(10), 3608-3611.
[7] Dahl, J. B. (2013). Heat Assisted Magnetic Recording Head-Disk Interface: Numerical Simulation of Air Bearing and Lubricant Mechanics (Doctoral dissertation, UNIVERSITY OF CALIFORNIA, BERKELEY).
[8] Mueller, S. (1998). Micro house PC Hardware Library, Volume I: Hard Drives. Macmillan Computer Publishing.
[9] Kaseta, R. G. Ruggedized disk drives for commercial airborne computer systems. Miltope Corporation.
[10] http://www.storagereview.com/ssd_vs_hdd
[11] Kryder, M. H., Gage, E. C., McDaniel, T. W., Challener, W., Rottmayer, R. E., Ju, G., Erden, M. F. (2008). Heat assisted magnetic recording. Proceedings of the IEEE, 96(11), 1810-1835.
[12] International Technical Roadmap: Magnetic Data Storage - the technology of magnetic hard disk drives. (2013). IDEMA Advanced Storage Technology Committee (ASTC), Tech. Rep.
[13] De Gennes, P. G., Brochard-Wyart, F., Quéré, D. (2013). Capillarity and wetting phenomena: drops, bubbles, pearls, waves. Springer Science & Business Media.
[14] Israelachvili, J. N. (2011). Intermolecular and surface forces: revised third edition. Academic press.
[15] Blossey, R. (2012). Thin liquid films: dewetting and polymer flow. Springer Science & Business Media.
[16] Mate, C. M. (2008). Tribology on the small scale. Oxford University Press, Oxford.
[17] Eres, M. H., Schwartz, L. W., Roy, R. V. (2000). Fingering phenomena for driven coating films. Physics of Fluids (1994-present), 12(6), 1278-1295.
[18] Mate, C. M. (2011). Taking a fresh look at disjoining pressure of lubricants at slider-disk interfaces. Magnetics, IEEE Transactions on, 47(1), 124-130.
[19] Reynolds, O. (1886). On the Theory of Lubrication and Its Application to Mr. Beauchamp Tower's Experiments, Including an Experimental Determination of the Viscosity of Olive Oil. Proceedings of the Royal Society of London, 40(242-245), 191-203.
[20] Oron, A., Davis, S. H., Bankoff, S. G. (1997). Long-scale evolution of thin liquid films. Reviews of modern physics, 69(3), 931.
[21] Batchelor, G. K. (2000). An introduction to fluid dynamics. Cambridge university press.
[22] Spencer, A. J. M. (2004). Continuum mechanics. Courier Corporation.
[23] Karis, T. (2009). Lubricants for the Disk Drive Industry, in Lubricant Additives: Chemistry and Applications, L. Rudnick, Ed., CRC Press, ch. 22, pp. 523-584.
[24] Gross, W. A., Matsch, L. A., Castelli, V., Eshel, A., Vohr, J. H., Wildmann, M. (1980). Fluid film lubrication (No. DOE/TIC-11301). John Wiley and Sons, Inc., New York, NY.

[25] Maxwell, J. C. (1879). On stresses in rarified gases arising from inequalities of temperature. Philosophical Transactions of the royal society of London, 231-256.
[26] Brenner, H. (2011). Beyond the no-slip boundary condition. Physical Review E, 84(4), 046309.
[27] Churaev, N. V., Derjaguin, B. V., Muller, V. M. (2013). Surface forces. Springer Science & Business Media.
[28] Marchon, B. (2011). Thin-film media lubricants: Structure, characterization, and performance. Developments in Data Storage: Materials Perspective, 144.
[29] Challener, W. A., Peng, C., Itagi, A. V., Karns, D., Peng, W., Peng, Y., Gage, E. C. (2009). Heat-assisted magnetic recording by a near-field transducer with efficient optical energy transfer. Nature photonics, 3(4), 220-224.
[30] Xiong, S., Kim, J., Wang, Y., Zhang, X., Bogy, D. (2014). A two-stage heating scheme for heat assisted magnetic recording. Journal of Applied Physics, 115(17), 17B702.
[31] Xiong, S., Bogy, D. B. (2014). Experimental study of head-disk interface in heat-assisted magnetic recording. Magnetics, IEEE Transactions on, 50(3), 148-154.
[32] Dahl, J. B., Bogy, D. B. (2013). Lubricant flow and evaporation model for heat-assisted magnetic recording including functional end-group effects and thin film viscosity. Tribology Letters, 52(1), 27-45.
[33] Meeks, S. W., Weresin, W. E., Rosen, H. J. (1995). Optical surface analysis of the head-disk-interface of thin film disks. Journal of tribology, 117(1), 112-118.
[34] Xiong, S., Wu, H., Bogy, D. (2014, September). Lubricant depletion under various laser heating conditions in Heat Assisted Magnetic Recording (HAMR). In SPIE Optical Engineering+ Applications (pp. 920109-920109). International Society for Optics and Photonics.
[35] Marchon, B., Dai, Q., Nayak, V., Pit, R. (2005). The physics of disk lubricant in the continuum picture. Magnetics, IEEE Transactions on, 41(2), 616-620.
[36] Mendez, A. R., Bogy, D. B. (2014). Lubricant flow and accumulation on the slider's air-bearing surface in a hard disk drive. Tribology Letters, 53(2), 469-476.
[37] Karis, T. E., Marchon, B., Flores, V., Scarpulla, M. (2001). Lubricant spin-off from magnetic recording disks. Tribology Letters, 11(3-4), 151-159.
[38] Marchon, B., Karis, T., Dai, Q., Pit, R. (2003). A model for lubricant flow from disk to slider. Magnetics, IEEE Transactions on, 39(5), 2447-2449.
[39] Tani, H., Iwasaki, K., Maruyama, Y., Ota, I., Tagawa, N. (2011). Lubricant pickup of ultra-thin PFPE lubricants with different backbone structures. Magnetics, IEEE Transactions on, 47(7), 1837-1841.
[40] Tani, H., Kubota, M., Tsujiguchi, Y., Tagawa, N. (2011). Visualization of lubricant pickup phenomena by lubricant thickness mapping on slider surface. Microsystem technologies, 17(5-7), 1175-1178.
[41] Wu, L. (2008). A model for liquid transfer between two approaching gas bearing surfaces through coupled evaporation-condensation and migration dynamics. Journal of Applied Physics, 104(1), 014503.
[42] Li, J., Xu, J., Aoki, Y. (2009). Air bearing design to prevent reverse flow from the trailing edge of the slider. Tribology letters, 35(2), 113-120.
[43] Kasai, P. H., Raman, V. (2012). Lubricant transfer in disk drives. Tribology Letters, 48(3), 367-374.

[44] Kim, S. H., Dai, Q., Marchon, B., Flechsig, K. (2009). Humidity effects on lubricant transfer in the head-disk interface of a hard disk drive. Journal of Applied Physics, 105(7), 07B704.
[45] Yanshneg, M., Kee, T. B., Bo, L. (2006). Lubricant transfer and slider–lubricant interaction at ultra-low flying height. Journal of Magnetism and Magnetic Materials, 303(2), e110-e114.
[46] Tan, B. K., Liu, B., Ma, Y., Zhang, M., Ling, S. F. (2007). Effect of electrostatic force on slider-lubricant interaction. Magnetics, IEEE Transactions on, 43(6), 2241-2243.
[47] Kubotera, H., Imamura, T. (2009). Monte Carlo simulations of air shielding effect on lubricant transfer at the head disk interface. Applied Physics Letters, 94(24), 243112.
[48] Smallen, M. J., Huang, H. W. (2003). Effect of disjoining pressure on disk-to-head lubricant transfer. Magnetics, IEEE Transactions on, 39(5), 2495-2497.
[49] Ma, Y., Liu, B. (2007). Lubricant transfer from disk to slider in hard disk drives. Applied physics letters, 90(14), 143516.
[50] Ma, Y., Liu, B. (2008). Dominant factors in lubricant transfer and accumulation in slider-disk interface. Tribology Letters, 29(2), 119-127.
[51] Wu, L. (2006). Modeling and simulation of the interaction between lubricant droplets on the slider surface and air flow within the head/disk interface of disk drives. Magnetics, IEEE Transactions on, 42(10), 2480-2482.
[52] Ambekar, R. P., Bogy, D. B., Bhatia, C. S. (2009). Lubricant depletion and disk-to-head lubricant transfer at the head-disk interface in hard disk drives. Journal of Tribology, 131(3), 031901.
[53] Marchon, B., Guo, X. C., Moser, A., Spool, A., Kroeker, R., Crimi, F. (2009). Lubricant dynamics on a slider:“The waterfall effect”. Journal of Applied Physics, 105(7), 074313.
[54] Mate, C. M., Marchon, B., Murthy, A. N., Kim, S. H. (2010). Lubricant-induced spacing increases at slider–disk interfaces in disk drives. Tribology letters, 37(3), 581-590.
[55] Ambekar, R. P., Bogy, D. B. (2005). Effect of slider lubricant pickup on stability at the head-disk interface. Magnetics, IEEE Transactions on, 41(10), 3028-3030.
[56] Ambekar, R., Gupta, V., Bogy, D. B. (2005). Experimental and numerical investigation of dynamic instability in the head disk interface at proximity. Journal of tribology, 127(3), 530-536.
[57] Matsuoka, H., Kan-Nen, M., Fukui, S. (2011). Theoretical model for lubricant pick-up (Breakage of liquid meniscus bridge due to elongation in bridged direction). Magnetics, IEEE Transactions on, 47(10), 3582-3585.
[58] Marchon, B. (2009). Lubricant design attributes for subnanometer head-disk clearance. Magnetics, IEEE Transactions on, 45(2), 872-876.
[59] Gui, J., Marchon, B. (1998). Fly/stiction: mechanical instability of a head-disc interface. Magnetics, IEEE Transactions on, 34(4), 1804-1806.
[60] Cong, P., Kubo, T., Nanao, H., Minami, I., Mori, S. (2005). Tribological performance and transfer behavior of lubricating oils at head-disk interface under volatile organic contamination. Tribology Letters, 19(4), 299-309.
[61] Pit, R., Zeng, Q. H., Dai, Q., Marchon, B. (2003). Experimental study of lubricant-slider interactions. Magnetics, IEEE Transactions on, 39(2), 740-742.
[62] Ma, Y., Liu, B. (2008). Lube depletion caused by thermal-desorption in heat assisted magnetic recording. Magnetics, IEEE Transactions on, 44(11), 3691-3694.
[63] Dahl, J. B., Bogy, D. B. (2013). Simulation of lubricant recovery after heat-assisted magnetic recording writing. Tribology Letters, 52(1), 163-174.

[64] Ji, R., Dao, T. K. L., Xu, B. X., Xu, J. W., Goh, B. L., Tan, E., Liew, T. (2011). Lubricant pickup under laser irradiation. Magnetics, IEEE Transactions on, 47(7), 1988-1991.
[65] Wu, L. (2007). Modelling and simulation of the lubricant depletion process induced by laser heating in heat-assisted magnetic recording system. Nanotechnology, 18(21), 215702.
[66] Zhang, J., Ji, R., Xu, J. W., Ng, J. K. P., Xu, B. X., Hu, S. B., Piramanayagam, S. N. (2006). Lubrication for heat-assisted magnetic recording media. Magnetics, IEEE Transactions on, 42(10), 2546-2548.
[67] Wu, L. (2006). A two-dimensional model for the interaction between lubricant droplet on the slider surface and air flow within the head/disk interface of disk drives. Journal of applied physics, 99(8), 08N101.
[68] Kubotera, H., Bogy, D. B. (2007). Lubricant migration simulations on the flying head slider air-bearing surface in a hard disk drive. Magnetics, IEEE Transactions on, 43(9), 3710-3715.
[69] Liu, N., Bogy, D. B. (2009). Air-bearing shear force in the head–disk interface of hard disk. Tribology letters, 35(2), 121-125.
[70] Scarpulla, M. A., Mate, C. M., Carter, M. D. (2003). Air shear driven flow of thin perfluoropolyether polymer films. The Journal of chemical physics, 118(7), 3368-3375.
[71] Mate, C. M. (2013). Spreading kinetics of lubricant droplets on magnetic recording disks. Tribology Letters, 51(3), 385-395.
[72] O'Brien, S. B. G., Schwartz, L. W. (2002). Theory and modeling of thin film flows. Encyclopedia of surface and colloid science, 5283-5297.
[73] Kubotera, H., Bogy, D. B. (2007). Numerical simulation of molecularly thin lubricant film flow due to the air bearing slider in hard disk drives. Microsystem technologies, 13(8-10), 859-865.
[74] Bowles, A. P., Hsia, Y. T. (2009). Quasi-equilibrium AFM measurement of disjoining pressure in lubricant nanofilms II: Effect of substrate materials. Langmuir, 25(4), 2101-2106.
[75] http://cml.berkeley.edu/cmlair_new.html
[76] LeVeque, R. J. (2007). Finite difference methods for ordinary and partial differential equations: steady-state and time-dependent problems (Vol. 98). Siam.
[77] Cha, E. T. (1993). Numerical analysis of head-disk assembly dynamics for shaped-rail sliders with sub-ambient pressure regions. University of California, Berkeley.
[78] Ma, X., Chen, J., Richter, H. J., Tang, H., Gui, J. (2001). Contribution of lubricant thickness to head-media spacing. Magnetics, IEEE Transactions on, 37(4), 1824-1826.
[79] Guo, X. C., Knigge, B., Marchon, B., Waltman, R. J., Carter, M., Burns, J. (2006). Multidentate functionalized lubricant for ultralow head/disk spacing in a disk drive. Journal of applied physics, 100(4), 044306.
[80] Gui, J. (2003). Tribology challenges for head-disk interface toward 1 Tb/in 2. Magnetics, IEEE Transactions on, 39(2), 716-721.
[81] Ma, X., Gui, J., Smoliar, L., Grannen, K., Marchon, B., Jhon, M. S., Bauer, C. L. (1999). Spreading of perfluoropolyalkylether films on amorphous carbon surfaces. The Journal of chemical physics, 110(6), 3129-3137.
[82] Jhon, M. S., Izumisawa, S., Guo, Q., Phillips, D. M., Hsia, Y. (2003). Simulation of nanostructured lubricant films. Magnetics, IEEE Transactions on, 39(2), 754-758.
[83] Waltman, R. J., Khurshudov, A., Tyndall, G. W. (2002). Autophobic dewetting of perfluoropolyether films on amorphous-nitrogenated carbon surfaces. Tribology Letters, 12(3), 163-169.

[84] Ma, X., Gui, J., Grannen, K. J., Smoliar, L. A., Marchon, B., Jhon, M. S., Bauer, C. L. (1999). Spreading of PFPE lubricants on carbon surfaces: effect of hydrogen and nitrogen content. Tribology Letters, 6(1), 9-14.
[85] Reiter, G. (1992). Dewetting of thin polymer films. Physical Review Letters, 68(1), 75.
[86] Xie, R., Karim, A., Douglas, J. F., Han, C. C., Weiss, R. A. (1998). Spinodal dewetting of thin polymer films. Physical Review Letters, 81(6), 1251.
[87] Seemann, R., Herminghaus, S., Jacobs, K. (2001). Dewetting patterns and molecular forces: A reconciliation. Physical Review Letters, 86(24), 5534.
[88] Redon, C., Brochard-Wyart, F., Rondelez, F. (1991). Dynamics of dewetting. Physical review letters, 66(6), 715.
[89] Becker, J., Grün, G., Seemann, R., Mantz, H., Jacobs, K., Mecke, K. R., Blossey, R. (2003). Complex dewetting scenarios captured by thin-film models. Nature Materials, 2(1), 59-63.
[90] Derjaguin, B. V., Churaev, N. V. (1974). Structural component of disjoining pressure. Journal of Colloid and Interface Science, 49(2), 249-255.
[91] Witelski, T. P., & Bowen, M. (2003). ADI schemes for higher-order nonlinear diffusion equations. Applied Numerical Mathematics, 45(2), 331-351.
[92] Kim, H. I., Mate, C. M., Hannibal, K. A., Perry, S. S. (1999). How disjoining pressure drives the dewetting of a polymer film on a silicon surface. Physical review letters, 82(17), 3496.
[93] Evans, L. C. (1998). Partial Differential Equations, Graduate Studies in Mathematics, vol. 19, American Mathematical Society, Providence.
[94] Karis, T. E., Tyndall, G. W. (1999). Calculation of spreading profiles for molecularly-thin films from surface energy gradients. Journal of non-newtonian fluid mechanics, 82(2), 287-302.
[95] Marchon, B., Dai, Q., Knigge, B., Pit, R. (2007). Lubricant dynamics in the sub-nanometer clearance regime. Magnetics, IEEE Transactions on, 43(9), 3694-3698.
[96] Lauga, E., Brenner, M., Stone, H. (2007). Microfluidics: the no-slip boundary condition. In Springer handbook of experimental fluid mechanics (pp. 1219-1240). Springer Berlin Heidelberg.
[97] De Gennes, P. G. (1985). Wetting: statics and dynamics. Reviews of modern physics, 57(3), 827.
[98] Li, N., Meng, Y., Bogy, D. B. (2011). Effects of PFPE lubricant properties on the critical clearance and rate of the lubricant transfer from disk surface to slider. Tribology Letters, 43(3), 275-286.
[99] Mate, C. M. (1998). Molecular tribology of disk drives. Tribology Letters, 4(2), 119-123.
[100] Liu, N., Bogy, D. B. (2009). Air-bearing shear force in the head–disk interface of hard disk. Tribology letters, 35(2), 121-125.
[101] Mate, C. M., Payne, R. N., Dai, Q., & Ono, K. (2006). Nanoscale origins of dynamic friction in an asymmetric contact geometry. Physical review letters, 97(21), 216104.
[102] Newmark, N. M. (1959). A method of computation for structural dynamics. Journal of the Engineering Mechanics Division, 85(3), 67-94.
[103] Chopra, A. K. (1995). Dynamics of structures: theory and applications to earthquake engineering. New Jersey: Prentice Hall.
[104] Kelley, C. T. (2003). Solving nonlinear equations with Newton's method. Siam.
[105] Deuflhard, P. (2011). Newton methods for nonlinear problems: affine invariance and adaptive algorithms (Vol. 35). Springer Science & Business Media.
[106] Cha, E. T. (1993). Numerical analysis of head-disk assembly dynamics for shaped-rail sliders with sub-ambient pressure regions. University of California, Berkeley.

[107] Pit, R., Marchon, B., Meeks, S., Velidandla, V. (2001). Formation of lubricant “moguls” at the head/disk interface. Tribology Letters, 10(3), 133-142.
[108] Ma, X., Tang, H., Stirniman, M., Gui, J. (2002). Lubricant thickness modulation induced by head-disk dynamic interactions. Magnetics, IEEE Transactions on, 38(1), 112-117.
[109] Dai, Q., Knigge, B. E., Waltman, R. J., Marchon, B. (2003). Time evolution of lubricant-slider dynamic interactions. IEEE transactions on magnetics, 39(5), 2459-2461.
[110] Watanabe, T., Bogy, D. B. (2003). A study of the lubricant displacement under a flying head slider caused by slider-disk interaction. Magnetics, IEEE Transactions on, 39(5), 2477-2479.
[111] Dai, Q., Saint-Olive, C., Pit, R., Marchon, B. (2002). Genesis and evolution of lubricant moguls. Magnetics, IEEE Transactions on, 38(5), 2111-2113.
[112] Izumisawa, S., Jhon, M. S. (2006). Stability model for a lubricant film with a slider. Magnetics, IEEE Transactions on, 42(10), 2537-2539.
[113] Matsuoka, H., Ohkubo, S., Fukui, S. (2005). Corrected expression of the van der Waals pressure for multilayered system with application to analyses of static characteristics of flying head sliders with an ultrasmall spacing. Microsystem technologies, 11(8-10), 824-829.
[114] Sarabi, M. S. G., Bogy, D. B. (2014). Simulation of the Performance of Various PFPE Lubricants Under Heat Assisted Magnetic Recording Conditions. Tribology Letters, 56(2), 293-304.
[115] Pan, D., Ovcharenko, A., Tangaraj, R., Yang, M., Talke, F. E. (2014). Investigation of lubricant transfer between slider and disk using molecular dynamics simulation. Tribology Letters, 53(1), 373-381.
[116] Seo, Y. W., Pan, D. Z., Ovcharenko, A., Yang, M., Talke, F. E. (2014). Molecular Dynamics Simulation of Lubricant Transfer at the Head-Disk Interface. Magnetics, IEEE Transactions on, 50(11), 1-4.
[117] Schaaf, S. A., Chambré, P. L. (1961). Flow of rarefied gases. Princenton University Press.
[118] Karniadakis, G., Beskok, A., Aluru, N. (2006). Microflows and nanoflows: fundamentals and simulation (Vol. 29). Springer Science & Business Media.
[119] Burgdorfer, A. (1959). The influence of the molecular mean free path on the performance of hydrodynamic gas lubricated bearings. Trans. ASME, Ser. D, 81, 94-100.
[120] Hsia, Y. T., Domoto, G. A. (1983). An experimental investigation of molecular rarefaction effects in gas lubricated bearings at ultra-low clearances. Journal of Tribology, 105(1), 120-129.
[121] Fukui, S., Kaneko, R. (1988). Analysis of ultra-thin gas film lubrication based on linearized Boltzmann equation: first report—derivation of a generalized lubrication equation including thermal creep flow. Journal of Tribology, 110(2), 253-261.
[122] S. Fukui, R. Kaneko, (1995). Molecular Gas Film Lubrication (MGL)," in Handbook of MicroNano Tribology, B. Bhushan, Ed., 1st, CRC Press Inc., ch. 13, pp. 559-604.